Missouri State University

BearWorks

MSU Graduate Theses

Spring 2017

Development of Many-Body Potential for Deformation Study in Al-Tin Nanolayered Composites

Paul Yaohan Simanjuntak

As with any intellectual project, the content and views expressed in this thesis may be considered objectionable by some readers. However, this student-scholar's work has been judged to have academic value by the student's thesis committee members trained in the discipline. The content and views expressed in this thesis are those of the student-scholar and are not endorsed by Missouri State University, its Graduate College, or its employees.

Follow this and additional works at: https://bearworks.missouristate.edu/theses

 Part of the Materials Science and Engineering Commons

Recommended Citation

Simanjuntak, Paul Yaohan, "Development of Many-Body Potential for Deformation Study in Al-Tin Nanolayered Composites" (2017). *MSU Graduate Theses*. 3159.
https://bearworks.missouristate.edu/theses/3159

This article or document was made available through BearWorks, the institutional repository of Missouri State University. The work contained in it may be protected by copyright and require permission of the copyright holder for reuse or redistribution.
For more information, please contact BearWorks@library.missouristate.edu.

DEVELOPMENT OF MANY-BODY POTENTIAL FOR DEFORMATION STUDY IN Al-TiN NANOLAYERED COMPOSITES

A Master Thesis

Presented to

The Graduate College of

Missouri State University

In Partial Fulfillment

Of the Requirements for the Degree

Master of Science, Materials Science

By

Paul Simanjuntak

May 2017

DEVELOPMENT OF MANY-BODY POTENTIAL FOR DEFORMATION STUDY IN Al-TiN NANOLAYERED COMPOSITES

Physics, Astronomy, and Materials Science

Missouri State University, May 2017

Master of Science

Paul Simanjuntak

ABSTRACT

A novel interatomic potential of ternary Al-Ti-N has been developed to study the deformation behavior of Al-TiN nanolaminates. The ternary nanolayered Al-TiN composite has attracted a lot of interest due to its combination of strength and ductility. The current analysis on the system has been primarily concentrated on continuum models which are inadequate to explain the key deformation events such as nucleation and interaction of dislocations. Progress in the preferred atomistic approach has been hampered however by the lack of available interatomic potential optimized for the ternary system. I developed a many-body potential based on embedded atomic model (EAM) by employing the force-fitting code Potfit to sample the energy and force data generated from the *ab-initio* molecular dynamics simulations of the ternary system using VASP code. The potential's analytical EAM function was subsequently optimized and utilized to simulate structures of bulk Al & TiN and Al-TiN nanolaminates. I then focused on modeling the deformation behavior of Al-TiN multilayers under compression through classical molecular dynamics simulations. I found that the total bilayer thickness as well as volume ratio between TiN and Al nanolayers play a major role in controlling the dislocation nucleation and mobility and the stress accumulation at the layer interface and thus determine the deformation behavior and failure mechanisms of the nanolayered composites.

KEYWORDS: interatomic potential, molecular dynamics, nanolayers, deformation, metal-ceramic

This abstract is approved as to form and content

_____

Ridwan Sakidja, PhD
Chairperson, Advisory Committee
Missouri State University

DEVELOPMENT OF MANY-BODY POTENTIAL FOR DEFORMATION STUDY IN Al-TiN NANOLAYERED COMPOSITES

By

Paul Simanjuntak

A Master Thesis
Submitted to the Graduate College
Of Missouri State University
In Partial Fulfillment of the Requirements
For the Degree of Master of Science, Materials Science

May 2017

Approved:

_____
Ridwan Sakidja, PhD

_____
David M. Cornelison, PhD

_____
Matthew C. Pierson, PhD

_____
Julie Masterson, PhD: Dean, Graduate College

ACKNOWLEDGEMENTS

I would like to thank you my advisor, Dr. Ridwan Sakidja, for all his help in my research and my two years in MSU. I also want to thank my brother, for without his cooperation, my thesis will not be in the shape it is today. Last, I want to thank the Physics, Astronomy, and Material Science Department in MSU for providing a friendly work environment for me to complete my study.

TABLE OF CONTENTS

LIST OF TABLES

LIST OF FIGURES

INTRODUCTION

Nano-layered Composites

Recent Development in Nanolaminates.

Thin film deposition as a method of controlling material's behaviour per se is not necessarily a novel idea in materials science. Review of recent publications on journals dedicated to this processing method can find a wide array of its applications in fields such as productions of solar cells, storage devices, and electronic control devices. Nevertheless, much of more recent interests in this field can be attributed to the increasing needs to procure a high degree of control of the wanted properties when one reduces the working dimension of these forms of materials into the nanoscale level. One of the most high-profile examples in recent years is graphene. This class of carbon-based materials shows markedly high transport and conduction properties, phenomenon unseen on the bulk material. In fact, the Nobel in Physics awarded to the original group who popularized graphene in 2010 has only increased the research interests in these thin materials.

Most of the research effort so far has been expended on fabricating single constituent materials for the purpose of creating a certain thick layer of material. For example, many of the semiconductor applications such as in solar cells or MOSFET's are based on the success in creating contacting layers of p-type and n-type semiconductors (the –well-known p-n junction). Certainly, having the capability to control precisely the quality of this p-n junction is one of the reasons, among others, as to why this type of thin film study is typically found to be interesting by many. Less studied is, however, the property of two materials deposited alternatively with the sole purpose of creating an

interchanging and dynamic nano-scale layered structure through the aid of external factors such as mechanical forces. This kind of material will be the main object of this study.

In the past, creating this type of material can be quite problematic. Not only facing the challenge of creating sufficiently thin layers, older processing techniques such as sintering might also create unwanted chemical reactions at the interface, thus limiting the fabrication of possible combinations only to chemically compatible materials [1]. More recent deposition techniques, however, have largely avoided this problem, allowing more thorough and wide-ranging investigations, even though they now consists only a small part of the body of research in thin films, in fabrication a variety of novel multilayer systems with two alternating layers. Moreover, large advances in imaging techniques such as high-resolution TEM (HRTEM) have greatly helped, and thus become indispensable tools in elucidating the intricate nature of nanoscale layered materials [2]. One reason as to why this subject attracts great interests is the need to observe the interaction between two materials in contact within such a close proximity especially at the atomistic level. As one reduces the layer thickness, the interface area to volume ratio increases, giving the interaction at the interface an increasing role to play. In particular, one is often interested in the case when the two constituent materials are of significantly different nature. Hence, one can envision that the layer thickness effect will play a major role in controlling the particular properties of the multilayers, an effect that has been seen repeatedly over various multi-layer systems. Four of these affected properties will be discussed here: the electronic system, magnetic system, optical system, and 'tough-resistant' system. Certainly, these four systems are not mutually exclusive and definitely

not exhaustive (indeed, one can reasonably argue that they lie under the metal-ceramic system, which encompasses almost all of the current interest in multilayers), but they lead to different applications and areas of interest. I will then close with a review of the mechanical behaviour of my material of interest; Al-TiN multilayers.

Electronic System.

In the computer hardware industry, one of the longstanding thrusts is to support the performance in an ever-smaller device. This is often achieved by creating an ever-denser circuit, packaging more connections in a given chip. One question is then how to create such a large number of connections without disrupting the signal transmission. As it turns out, this can be achieved by creating alternating multilayers of highly conducting metal with insulating ceramics [1]. In this scheme, which has been first studied almost fifty years ago, the metal and insulator layers, which are deposited by means of a photolithography technique, allow for short connections. These layers are extensively employed in complex circuits nowadays. This method of combining metal and ceramic layers, however, is not quite yet the version as is understood now, as it only contains several layers with different materials and more resembles the well-known metal-oxide-semiconductor scheme [3]. That said, the novelty and thus, the technological advance generated by this approach surely highlights the importance of the inter-layer chemical bonding.

Magnetic System.

A more recent manifestation of the metal-insulator system often concentrates on harnessing the novel magnetic property of the metal constituent for a great variety of applications ranging from solid state recording devices [4] to sensory devices [5]. In this

regard, it would actually be unfair to focus exclusively on the metal-isolator system, as ceramic-ceramic [6,7] and metal-metal systems [5,8,9] have also been explored quite extensively for the same reason, insofar that they may also exhibit novel magnetic behaviours that could be finely tuned when one adjusts the layer thickness to a nanoscale level. The question is always the same: how can one tune the magnetic property, such as paramagnetic property, to a wanted degree?

The exact nature of the magnetic effect on nanolaminates is not quite as straightforward as one would expect. It is well-established that nanoparticles under a certain critical size, which depends on the exact materials' properties, exist preferably as a single domain with certain magnetic moment [10], i.e. maintaining its own magnet. One can then attribute the detected magnetic properties due to two effects: the anisotropy and the interaction between particles. The anisotropy effect depends mostly on the shape of the particle, whereas the interaction effect, unsurprisingly, depends on the interparticle separations and cluster sizes. Applying these effects into the layering terms, one can possibly control the magnetic properties on the multilayers by controlling the layer thickness (the size effect) and the layer stacking as well as orientation (the separation effect), a familiar theme in a multilayer thin film deposition. Further explanation, however, would be system-dependent.

To illustrate the intricacies of this system, I would take an example here a magnetic metal-insulator system. One of the popular choices for an insulator layer is the high-temperature-resistant silicon nitride in its various form, such as Si_2N_2O [7], SiAlON [11], and, most importantly, Si_3N_4 [12] whose optical and transport properties make this phase to be particularly ubiquitous. That said, other oxides such as SnO_2 [5], MgO [13-

14], and Al_2O_3 [15] have also been investigated. The metal layer is usually chosen from some transition metals such as Mn, Fe, Ni, or Co, with a particular interest in manipulating their soft ferromagnetic property. In order to fully appreciate the layer interactions, it would presumably be ideal to create what is often termed "discontinuous metal-insulator multilayers" (DMIM). In other words, I should expect to find the usual alternating layers with clear interfacial boundaries between the two layers. This turns out to be a non-trivial problem, because the layer interaction itself might prevent the fabrication of such a thin film. One often finds, instead of forming separate layers with a clear demarcation between the two types of layers, the metal layer is actually embedded or protruded into the ceramic matrix with an interspersed ceramic layering, creating 'continuous' layers, so that the 'multilayers' would in fact act as an integral unit.

The solution to this problem is apparently closely related to the nature of layer interaction and the behaviours at the interface. In a study of Co-Si_3N_4 multilayers for example, it was found that the critical parameter is the thickness of metal layer in comparison with the insulator [12]. One observes the transition of the layer structures from DMIM for a thin layer with a thickness ratio of Co : $Si_3N_4 \approx$ 1.4 nm : 3 nm to 'continuous' multilayers for a layer with a comparable thickness but with a different thickness ratio of Co : $Si_3N_4 \approx$ 3.8 nm : 3 nm. The same phenomenon, with a different degree, has also been observed in other systems such as Fe-MgO [13-14]. The key observation here is that with a lower metal thickness, the magnetic property of the multilayers of soft ferromagnets shifts instead to show a superparamagnetic behaviour. In turn, this can be explained by the formation of a thin 'core-shell' structure of a metal-ceramic system at the interface, e.g. FeO on Fe-MgO system resulting in a weakened

ferromagnetism at the interface. This is just one example of an active role of the interface interaction in giving the multilayer system its unique magnetic property.

Optical System.

Applications of the multilayer idea can also be found on the field of photovoltaic materials. One path that has been extensively covered before is the usage of ceramic-metal (cermet) for the selective absorbing coating on the solar cell. For this application, one can consider, for example, an array of parabolic reflectors directed toward solar collector tubes, as is common in solar farms. This tube, an example of a solar absorber, would then be coated to maximize its absorbance of solar energy while minimizing the energy loss due to the blackbody radiation. Such a selective coating, then, would ideally has a perfect absorbance on the solar region and a very low emittance at the radiation region [16]. This problem can be somewhat complicated when one considers the high temperature ($> 400°C$) application, because the overlap of the two spectrums (the solar absorbance and the blackbody radiation) will grow more significant. Tuning the coatings' properties in this region is one of the focus on many solar cell studies.

Various materials have been tried for this purpose. The consideration for many of them would revolve around the idea of embedding clusters of metals surrounded by dielectric materials [17], hence the cermet material. Common ceramics such as AlN, Al_2O_3, SiO_2 have been tested for this design while the metal of choice ranges from Al [16], W [17], Mo [18], and Ni [19]. Most of them perform reasonably well and thusthere is a clear promise of growth in this direction. The construct of the typical absorber coating with cermet layers can be seen on Fig. 1.1

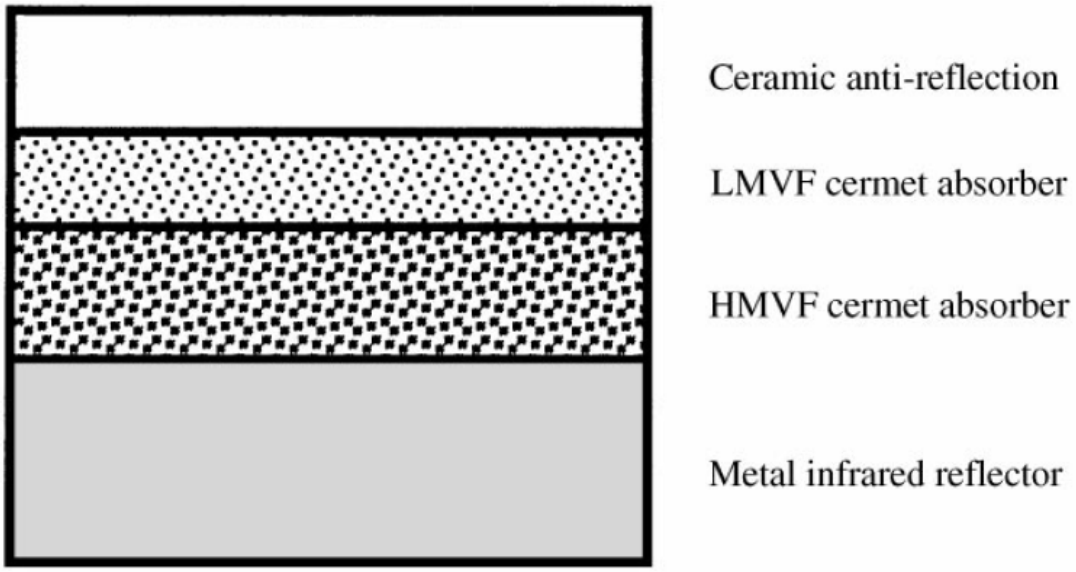

Figure 1.1: Typical construct of cermet absorber coating, using a layer each of LMVF (low metal volume fraction) and HVMF (high metal volume fraction) cermet material. Source: [16]

In order to maximize the absorbance by utilizing the optical interference, two layers with different properties are often used. I will quickly observe here two recurring themes: the essential roles of the individual layer thickness and the number of layers. The results from both the computational [16, 20] and experimental works [18] suggested that indeed the two main parameters determined to be crucial in cermet films are the metal content and the film thickness. The metal layer, which is mostly responsible for the absorbance [19], is also playing a part in increasing the reflectivity [20], making it necessary to suppress its content (hence the metal layer's thickness) as the first layer. When the thickness of the second layer, in conjunction with its metal content, is optimized, one can expect a maximum absorbance from interference to produce. Combined with a proper anti-reflective top layer and a reflective back layer, the double-layer cermet absorber coating has been shown to be a good candidate for high-temperature applications.

'Tough-resistant' System.

Last, I would discuss the application of the multilayer system in what I would call here the 'tough-resistant' system. This system has wide-ranging manifestations and, compared to previously-discussed fields, it is often utilized especially for its ability to withstand extreme mechanical pressures. The resistance, however, must also account for the stability of such a structure against a high temperature environment, including the capability to withstand melting and oxidation while maintaining other properties such as the thermal conductivity. These two characteristics are shared by some of the constituents, but not all, of the multilayer systems mentioned above. I shall review here some of the more notable examples: MAX phases and the metal-ceramic multilayers.

MAX Phases.

Even though it is only one of the many novel materials in recent years, the ternary MAX phases have recently been one that has attracted the most attention. A MAX phase is composed of interspersing layers of transition metal (M layer), carbon or nitrogen (X layer), and other metal or sometimes semimetal (A layer), creating compounds in the form $M_{n+1}AX_n$. The unit cell, as shown on Fig. 1.2, takes a hexagonal pattern with a space group $P6_3/mmc$ and has the characteristic that X layers are always situated between M layers (although the exact stacking depends on n), while blocks of MX compounds are joined together by A layer. Also characteristic is the "zig-zag" pattern from the M-X layers stacking. While certainly the MAX phase is not limited by $n = 4$ or a single phase (for example Ta_6AlC_5 and $Ti_5Si_2C_3$, where the half the unit cell of 312 and 211 phases are alternating forming a single unit cell, have been positively identified), one notices that stability of the unit cell decreases with increasing z-value of the M and A

layer. Due to the challenge in synthesis of a stable structure, even with the help of *ab-initio* calculation to suggest possible phase, only about 70 compounds (and hundreds of structures), mostly carbides, have been found to exist [21].

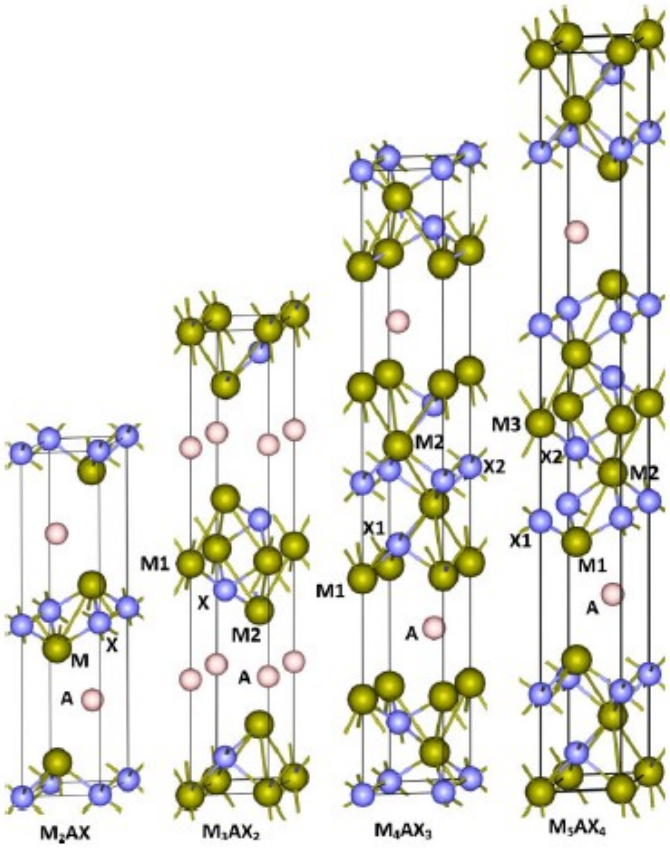

Figure 1.2: Ball-and-stick diagram of 211, 312, 413, and 514 MAX phases. Source: [22]

Indeed, the question of which MAX phases should exist, and why some of the seemingly natural phases do not exist, is quite a complex conundrum. In general, one expects that an existing phase should be intrinsically stable, i.e. the Gibbs free energy of the structure is at local minimum and should withstand small deformations such as lattice vibrations. Yet this is not necessarily true for a good number of structure [23]. For example, W-based phase such as W_2SN has no minimum energy position, while a structure of Mo_2SN was found to be unstable [24]. Even more baffling is the fact that while Ti_3SiC_2 and Ti_4SiC_3 have been known to exist for a long time, no synthesis effort so

far has successfully created Ti_2SiC. Certainly, such a stacking should be theoretically possible, as can be seen on the intergrowth phase of $Ti_5Si_2C_3$, but it is presumed that the temperature dependence of enthalpy values and the unstable nature of stacking as suggested by cohesive energy of $Ti_5Si_2C_3$, greatly complicate the growth condition [21]. Such questions are far beyond the scope of this short review, so I will simply focus on the properties of existing phases.

Our discussion so far has dwelled on the admittedly fascinating structure of MAX phase. However, the uniqueness of these phases is found mainly on their unusual, even extraordinary, combinations of chemical, physical, electrical, and mechanical properties. A comprehensive computational study on the elastic and electronic properties of existing and hypothetical phases shows generally strong structure of MAX phases [25]. A sizable number of them have a relatively well electrical conductivity and even some phases are known to be superconducting with some of them being mechanically stable at high temperatures (having a ductile-brittle transition temperature above 1000°C and thus, an excellent tribological property) [26]. Even more recent is the study of magnetic property found in MAX phases such as Cr_2AlC and Mn_2GaC [27].

An interesting point of view here is to contrast the property of the ternary phases with the corresponding MX ceramics. The combination of the metal and ceramic property is often represented in MAX phase. Indeed, this will be a running theme in this whole study and would turn out to be a particularly rich source of understanding especially when they exist but their properties do not follow the natural intuition. The conductivity of Ti-A-C is a case in point. It is known that TiC is quite a poor conductor with a relatively high resistivity and a low concentration of conduction electrons. However, if

the A layer is adopted into the MAX phase, I could expect an electrical conductivity to increase due to the weakening of the covalent Ti-C bonding and the strengthening of Ti-Ti metallic bonding. Moreover, a higher metal fraction should make this metallic property more prominent. This is indeed the case; the conductivity of Ti_2GeC is higher than Ti_3GeC_2, which in turn is greater than pure TiC [23]. Counterintuitively, however, the opposite applies for Ti-A-N phases, as the TiN segment of the MAX phases and its related property apparently dominate the ternary phase, making a more careful understanding of its band structure necessary.

In the interest of this study, it would only be proper to discuss the mechanical properties of MAX phase, one of the early triggers of interest in this field of ternary phases. For this purpose, some aspects of chemical bonding and dislocation behaviours need to be mentioned. As in their MX counterpart, any MAX phase shows a combination of covalent, metallic, and ionic bondings, in that order of importance. This should then suggest a certain degree of hardness due to the the prevalence of covalent bonding. Remarkable, however, is the strength of the M-X bonding, as shown by the higher-energy Raman modes along the c axis, in comparison with the weaker M-A bonds, corresponding to the lower-energy vibration along a axis [28]. As a consequence, MAX phases respond to stress solely on their basal planes in two ways: the arrangement at the grain boundary situated perpendicular to the basal planes or in the arrays parallel to it [29].

Using this knowledge, one can make sense many aspects of the MAX phase. Consider the phase Ti_2AlN, which has a special interest in this study. In Table 1.1, I compare some elastic properties of single-crystal Ti_2AlN, Ti_4AlN_3, and pure TiN.

Table 1.1: Comparison between single-crystal elastic properties of Ti_2AlN, Ti_4AlN_3, and pure TiN, with DFT calculations or experiment.

Elastic Constants	Ti_2AlN [24]	Ti_4AlN_3 [25]	TiN
K (GPa)	155	205	320 (Exp.) [30], 320 (DFT) [31]
C_{11} (GPa)	309	408	625 (Exp.) [32], 597 (DFT) [33]
C_{33} (GPa)	282	364	625 (Exp.) [32], 597 (DFT) [33]
C_{44} (GPa)	125	158	163 (Exp.) [32], 168 (DFT) [33]

Three things should be noted in this MAX-ceramic comparison. As has been mentioned above, I see the MAX phases as a relatively hard material, albeit with a reduced strength in a relative comparison to MX compounds due to the enhanced mechanical flow behaviour possibly generated by the Al sandwiched between the M-X layers . Also notice here the thickness effect: with an increasing number of M-X layers, the overall phase's properties resemble more closely those of the MX compound, hence suggesting a reduced importance of the weak M-A bonding and an increasing prominence of the ceramic properties. Last, quite surprisingly, in contrast to other layered materials such as graphite [34], the MAX phases are only mildly elastically anisotropic, with $C_{11} \approx C_{33}$, despite having only two identified slip systems [35]. The degree of isotropy reduces however for higher n parameter, again indicating a closer resemblance to the ceramics

Also interesting is the dislocation mechanism of Ti_2AlN, especially its unusual plastic behaviour. Consider the reversible loading cycle of during an indentation, as

shown in Fig. 1.3. This energy-dissipating mechanism is quite remarkable, especially among stiff materials, where such a strain hardening is rare.

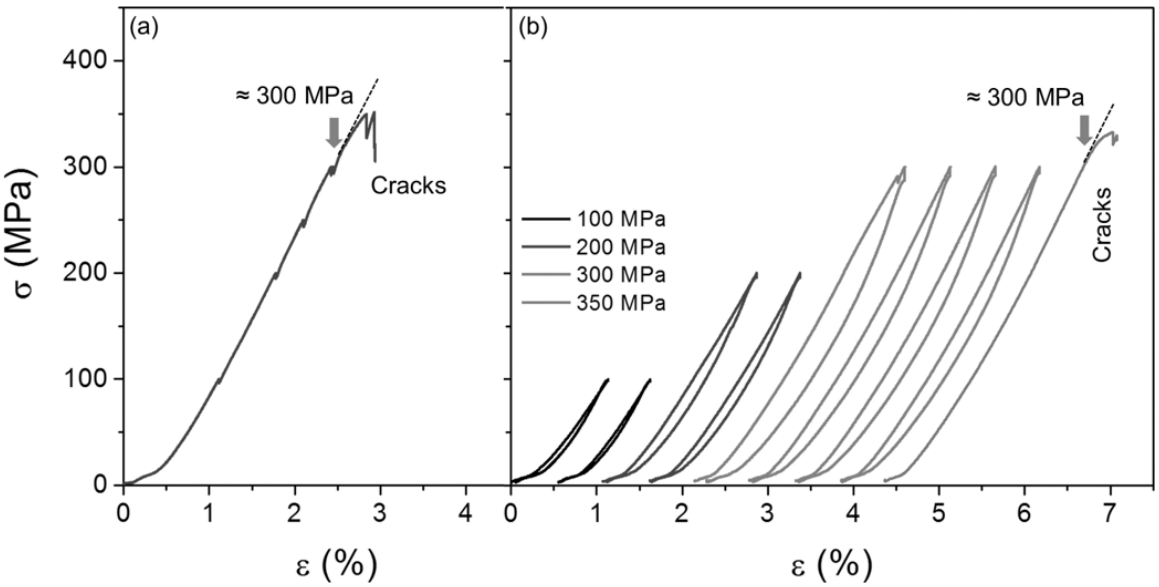

Figure 1.3: Stress-strain graphs for (a) continuous loading (b) loading-unloading cycles for Ti_2AlN (each cycle shifted for clarity). Source: [36]

Barsoum [29] proposed that the hysteretic elastic behaviour, which depends on the grain size (not shown in the graph above), can be explained by the Incipient Kink Band (IKB) mechanism. In this model, shown on Fig. 1.4, one can imagine the formation of dislocation walls at the origin of the kink band. An IKB is an ellipsoidal kink band that does not dissociate into dislocation walls. Composed of parallel dislocation loops on the basal planes, IKB will shrink when the load is removed and hence it is reversible. Mechanism of its growth is not quite clear, but this proposed mechanism allows a relatively easy material flow during indentations, causing delamination, but without the often-corresponding pile-ups [23]. So far, no such an IKB has been directly observed, despite of suggestive observations, and the existence of an open hysteresis loop on Fig. 1.4 somewhat puts doubts into its existence. An alternative mechanism based on an

analysis of a multi-axial stress-strain path has been proposed to explain the strain-hardening behaviour of MAX phases [35-37].

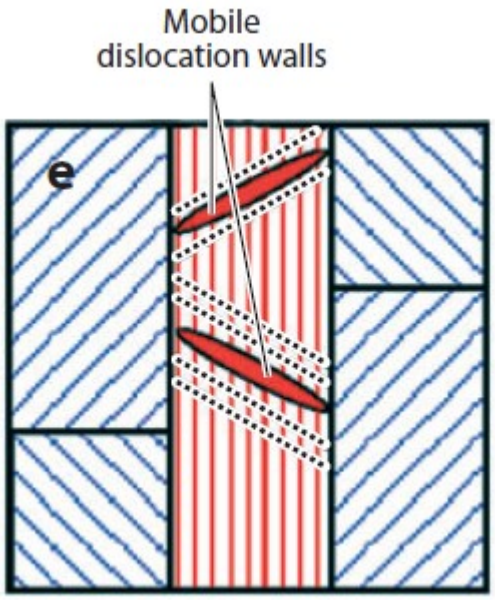

Figure 1.4: Schematic diagram of IKB formation (red eclipses) on hard grain (red) between soft grains (blue). Lines show the basal planes. Dislocation walls move on the same direction. Source: [29]

To end this section, I shall make quick comments on the application of MAX phases. It is quite hard to identify a single usage, because the unique combination of useful properties makes this class of material highly versatile, but I shall give some examples. Its combination of stiff but machinable material makes it useful in bulk for a variety of applications as heating elements, tools for die-pressing, and as impact-resistant materials [23]. The dense structure and the high-temperature stability also allow alternative applications as thin film in a irradiation-/corrosion-resistant coating such as in a nuclear protective coating [38-39].

Metal-Ceramic Multilayer.

The ’tough-resistant’ system of metal-ceramic multilayer (MCM) is not, in a sense, a very novel idea. Many ceramics, among the hardest materials ever known, have

been used as coatings for exactly the same reason. Nevertheless, it is the remarkable combination of the strength and versatility of such materials including the MAX phases, in combination with the surprising ductility that makes them an intense topic of research. Unlike MAX phases however, the physical characteristics of many of these ceramics are well-known, partly because of the many similarities of their properties and because their thermodynamic stability and existence are usually well-documented. In this section, I will discuss their structures and their relation to the general properties, in particular their deformation behaviour. I will then elaborate the properties of the main subject of my work; the Al-TiN multilayers, in the next section and draw a correlation with the observations from this section.

First, I should describe the structure of MCM. Different from the MAX phases, MCM is a simple alternating stacking of ceramic and metal: one does not limit itself to a single (or double) layer. Although many (in fact, any) ceramics, such as oxides, SiC, and carbon, are eligible, I will put a special emphasis here on the carbide and nitride phases. The metal, then, might be chosen to match the ceramic material (for example Ti-TiN), although any metal is possible, depending on its usage. At the interface, one can sometimes find a good lattice matching, although more often than not, heterophase interfaces are not always perfect, allowing coherent regions to be separated by misfit dislocations. Most likely I will see a semicoherent misfit, although sometimes incoherent interfaces might occur. Similarly, one can consider either reactive or non-reactive interfaces, especially when oxides are considered. This will then put limits on the operating pressure and temperature of the material. The choice of ceramics here will then leave only to consider the non-reactive case. Last, one can sometimes be left with

segregate phase at the interface, especially when using with polycrystalline metal [40-41]. This phase might have implications on the mechanical properties (e.g. to limit the dislocation mobility onto another phase), but I will limit my discussion here to simple, clean interfaces between the metal and ceramic layers.

The question then, just like the running theme in this writing this far, is the size of the layers. Generally speaking, one should expect MCM property to be governed by the rule of mixtures. However, the fact is a bit more complicated. In 1970, it was predicted [42] that one can create a strong multilayer provided four criterions are satisfied:

1. Lattice mismatch should be minimized over the working temperature range (but crystal structure is not necessarily the same).
2. Elastic constants should differ as much as possible, so that very large stress is needed before dislocations can move from the ’soft’ crystal to the ’hard’ one
3. Bonding between crystals should be on the same order as within the crystal
4. Thickness of both layers are about similarly small, preferably under 100 layers

When these four points were first outlined, the technology was barely available to create multilayers under a micrometre scale. However, better synthesis techniques have allowed the last principle to be thoroughly investigated and now the often called ’smaller is stronger’ principle has been implemented quite extensively [43]. A similar phenomenon has also been observed in metallic glasses [44]. In any case, I will show in the following sections that all but the second criterion is quite faithfully followed in creating the ’tough-resistant’ system.

The smaller working scale requires new experimental techniques to probe into the mechanical properties of the nanolayered MCM. For example, in the past, one can use a double cleavage compression or a relatively straightforward peel test to measure the strength of the interface [40]. A peel test, however, comes at the cost of producing a

complicated characterization of strain, as bending of the film is also involved. Many recent studies have employed more appropriately compression [46] and tensile [47] tests as well as the ubiquitous nanoindentation with a force applied normal to the interface [46, 48-50]. The nanoindentation method in particular is particularly useful, as the localized nature of its work might allow mechanical behaviour unseen in bulk and very different from other methods. It also works well with the *in-situ* TEM technique, enabling a 'live' snapshot of the experiment. I will see this technique being repeatedly employed in various situations, especially when the layerings are convenient

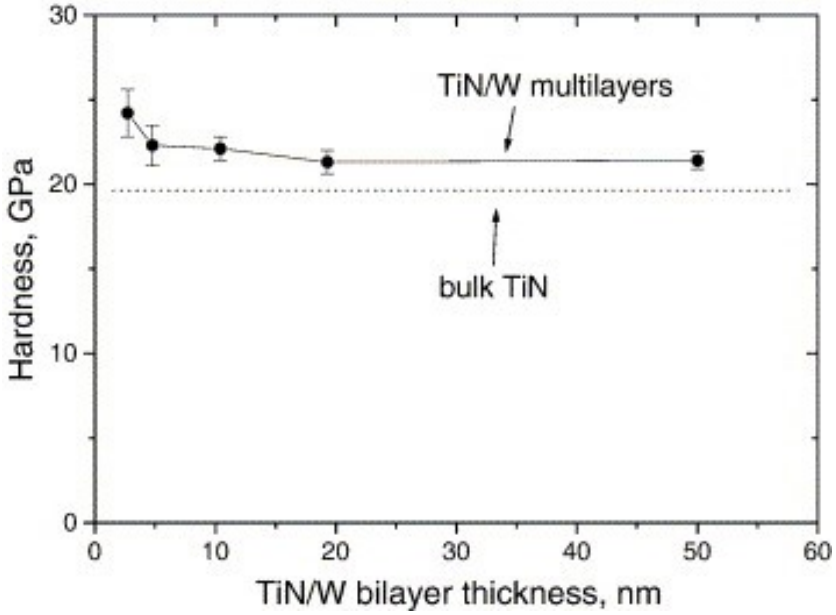

Figure 1.5: Comparing the hardness from nanoindentation of TiN-W with different bilayer periods. Source: [45]

Probably the most interesting feature of MCM lies in its combination of higher hardness and the increased level of ductility in comparison to similarly strong materials, especially when one considers the deviation from the rule of mixtures (see Fig. 1.5). Following the second principle above, one can explain this by the co-deformation behaviour of the metal and ceramic layers [51]. In general, one can expect the deformation to start to glide and to interact primarily on the softer metal layer. Failures,

then, will only happen when the dislocations could not transmit the stress into the harder ceramic layer with a consequence of an increasing level of stress at the interface [51]. One can then surmise, from various experiments, that three factors may govern the strength and ductility of MCM: (1) the material of choice, (2) the thickness of individual layer, and (3) the layer thickness ratio. I will discuss these factors in the following part.

First, I consider the material choice. In a study of TiC-metal multilayers [52], four different metals (Al, Cu, Fe, and W) with various thickness (kept invariably under 30 nm, often 10 nm), were tested for hardness. The result, as seen on Fig. 1.6, shows an improvement of the hardness value for some with, more importantly, an accompanying gain in ductility. However, notice that the result varies widely for different metals. While all samples see an improvement in toughness, the layers of a softer metal such as Al and Cu (not shown) show no improvement in hardness. Similar result has been shown by the combination of a hard NbN-W or NbN-Mo layer [53] and a soft layer of SiC-Al MCMs [47]. This seems to suggest that the MCM hardness is roughly determined by the metal layer itself. However, this is not universally true. For example, for theTiN-metal MCM's case, both the hard TiN-W [45] and the relatively softer TiN-Al [46] and TiN-Ti [54] layers endure significant changes. Even accounting for r the other two factors, one can still see the improvements above. Thus, while it is useful to consider the metal strength itself, one should be careful of the many exceptions to the rule.

The other two factors, the individual layers' thickness and their ratio, are simply a manifestation of the 'smaller is stronger' principle mentioned previously. Drawing a conclusion from Fig. 1.5 and 1.6(a), one can observe that the most gain is achieved when the individual layer thickness falls under 10 nm, a feature that is also shared by other

studies [46,53]. More interesting is the ratio effect. The most dramatic gain in Fig. 1.6 on TiC-Fe was achieved around the equal layers' size, also seen in the NbC-Nb [51] and TiN-Al [55] multi-layer systems but not shared by other combinations. Indeed, a urther study on the ratio effect for other materials is still needed to find a definite conclusion.

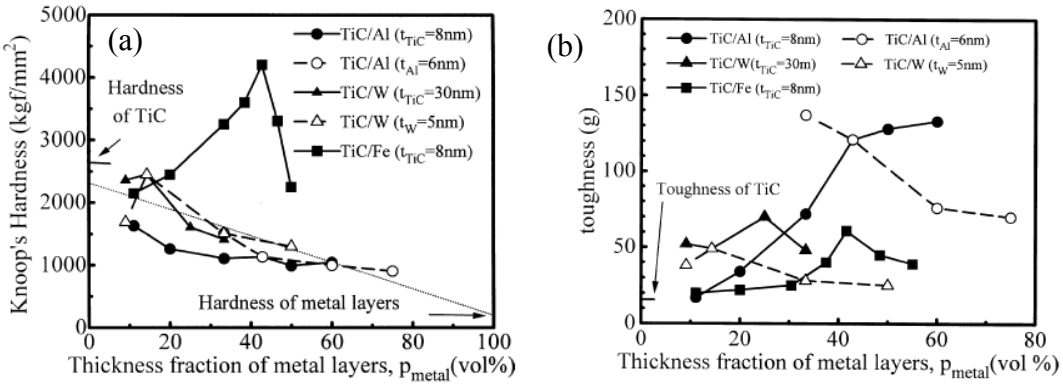

Figure 1.6: Comparison of (a) hardness and (b) toughness of TiC-Metal (Al, W, Fe) MCM with varying thickness ratio. Dotted straight line is prediction from rule of mixtures. Source: [52]

I have just described the observed phenomenon of increased hardness and ductility. I have not, however, explained the mechanism behind it. Almost naturally, one can consider the hardening would follow the dislocation pile-up analysis from the Hall-Petch relationship [56], which considers the geometry of multiple dislocation pile-ups at the interface with decreasing grain (i.e. layer) sizes to break the interface barrier. The problem is, this model assumes that the strength is constant irrespective of the layers' size, while the opposite is true [57]. At the same time, it has been calculated that two dislocations will follow indeed the Hall-Petch model. Then, one is left to consider the case of a single dislocation, where the thickness factor will be the key parameter that will prevent its nucleation. Most importantly, the large deviation from the Hall-Petch model (e.g. Fig. 1.5) suggests that the dislocation pile-ups cannot be the primary reason for strain hardening.

The most important mechanism is what is called the confined layer slip (CLS) [51,57]. In this construct, the formation of pile-up and dislocations is limited by the small scale of the metallic layer. The dislocations form glide loops in each layer, which then deposit the dislocation fronts on the interface (in some ways, this is analogous to the kink bands observed in MAX phases). Initially, these glide loops are placed sufficiently far apart and do not show any hardening. However, as one reaches further into the plastic regime with an increasing level of strain, these deposited dislocations will resist the motion of parallel loops, increasing the stress and causing the observed strain hardening. At the same time, when interacting with other types of dislocations (such as a misfit dislocation at the interface), these dislocations produce a glide motion in the direction of an adjacent layer which would correspond to slip transmissions. All of this implies that the strain hardening rate of the metal layer must be significantly higher than the overall rate, inducing a larger layer thickness reduction of the metallic layer. When the stress becomes sufficiently large, the material fails and cracks will show up on the ceramic layer.

Recall that in the MAX phases, I observe that many of its more interesting properties are provided by the relation between the A layer with the MX block, especially the interplay between weak M-A bonding and strong M-X (ceramic) bonding. The same importance to interface's role should be emphasized, especially because the interaction is the sole reason for its strength. As the CLS mechanism described above, the strength of MCM also depends on how far the interface can endure stress, for example on the matter of interface sliding in the plastic deformation [58].

There are two things I need to observe here. The first is, related to the first of four principles mentioned above, the need to minimize the lattice mismatch. This will affect either the material selection or the choice of orientation (or both) for the multi-layer design. For example, choosing interface to be the compact plane of both layers, such as $[111]_{fcc}$ or $[110]_{bcc}$, will possibly reduce both the lattice mismatch [59] and improve the energy stability [60]. That said, it is still possible to produce relatively stable multilayers with significant misfit such as Pd-ZnO, although one then expects some structure change caused by the in-plane relaxation [61]. Second, one should be aware of the nature of the bonding between the metal and the terminating layer of ceramic portion. For example, the [111]-oriented *fcc* metal and the nitrides (carbides) show that the metal Al layer shows a thermodynamic preference [62] possibly accompanied by an even slight structure modification [63], when it faces N(C)-layer instead of the metal component of the nitride/carbide layers [64-65]. A similar affinity has also been observed in Fe-N and Fe-C multi-layer systems [66]. On the other hand, both Cu and Pt metals show no such a preference, creating a relatively weak interface. Interestingly, both of these observations run counter to the findings on MAX phases. This property can be attributed to the particularly strong and the directional nature of short-range Al-N bonding (as shown in Fig. 1.7). These particularities can explain the difference between seemingly-similar materials (e.g. 2.9 to 4.5 yield stress of Cu-TiN [67] and Al-TiN [46], respectively).

I will end this section summarizing the key findings of MCMs. I will also point out some differences in comparison to those observed in MAX phases. While MAX phase generally shows an increasing stiffness with an increasing length, MCM shows an increased strength with a decreasing bilayer period. This implies the same observation

when one considers the metal-ceramic ratio. In MCM, dislocation slips are hindered by the interface, while the weak interface allows for alayer slip in MAX, greatly ameliorating the brittleness of the ceramic-like MX block. This stress-reduction mechanism is different in MCM, where the metal layer would serve as the sink for stress. Moreover, as noted before, the strong interface, with the particular preference of the directional covalent bonding to the metallic bonding in MAX, can explain a good part of the MCM's uniqueness. I will explore more in-depth of this property in the next section.

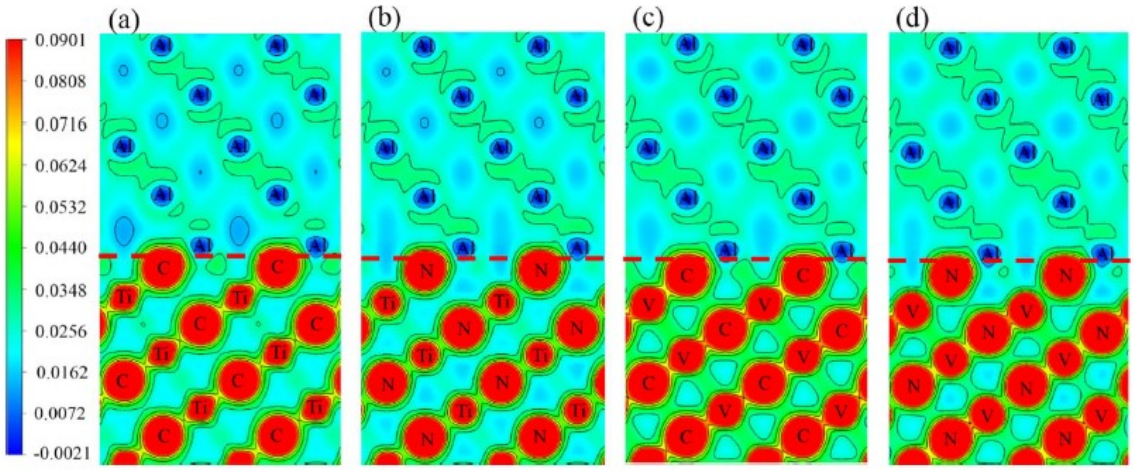

Figure 1.7: Charge density distribution of relaxed (a) Al-TiC, (b) Al-TiN, (c) Al-VC, and (d) Al-VN. Interface marked with red dotted line. Notice density difference of interface N(C) layer compared to the bulk. Source: [62]

Dislocation and Deformation on TiN-Al Multilayer.

The ceramic TiN phase is long recognized as one of the hardest material known to human, not to mention its excellent adhesion and oxidation resistance. This makes it particularly useful, for example, as a coating material for cutting tools. To improve its lifetime, the addition of micron-thick multilayers comprised of TiCN or Al_2O_3 has been tried before [68]. More recently, the multilayer of Al-TiN has been shown to exhibit a particularly attractive combination of extreme hardness and ductility, especially when the

layer size is reduced to within 10 nm thick [46,49,55,69]. This feature is particularly interesting, because, in contrast to the hard metal combination such as W-TiN [45] or Ti-TiN [54], this system uses a very 'soft' yet abundant metal, ie. Aluminum and still shows similarly interesting features. I will here review some of the experimental observations and simulation efforts to understand its deformation behaviour.

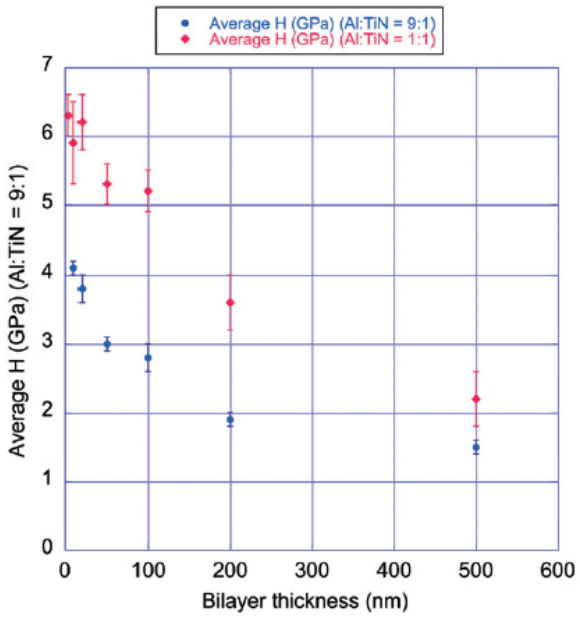

Fig. 1.8: Hardness of Al-TiN of various period and different volume ratio. Blue is Al:TiN = 9:1, red Al:TiN = 1:1. Source: [49]

Many features of the MCMs in the previous section are also observed here. To minimize the misfit, both crystals are often grown with the compact [111] plane (using B1 TiN) as interface plane. A nano-indentation study, shown on Fig. 1.8, found that when the bilayer thickness is made under 20 nm, multilayers with an equal volume ratio (Al:TiN ≈ 1:1) shows a higher hardness than that with a large difference in its volumetric ratio (Al:TiN ≈ 9:1) . Similarly, a thinner Al layer, and to lesser extent the TiN layer, show much a larger layer thickness reduction (as much as ~ 60% compared to ~ 8% in 9:1 case, roughly the overall reduction). *In-situ* TEM shows that marks of dislocations such as the shear band start on the Al layer, but the crack is always initiated in and

propagated within the TiN layer only. As expected, after a sufficiently large stress, tilted cracks will show up within the TiN layer while subgrains, but not fracture, are observed in Al layer.

More interesting is the observation regarding the nature of dislocations and cracks. On [49] and [55], dislocation pile-ups on Al are observed in the 9:1 samples, while none is observed in the 1:1 samples, although the report was not conclusive for the thinnest 9:1 case. This is consistent with the CLS mechanism, where the occurrence of pile-up is the governing mechanism. Similarly, crack is observed on all of the 9:1 samples, while [69] reported that for the 1:1 samples, only for samples with a bilayer thickness of 5.4 nm that fractures did not occur, 1;1 samples with a lesser thickness level is surprisingly devoid of any crack formation. While this can be expected from an increased hardness, cracks can also be found on both 1:1 and 9:1 samples with a larger overall thickness e.g. those with a 10 nm period, suggesting that overall thickness might be the primary driving force to initiate the crack nucleation.

As with MCMs, knowledge of interface properties assisted by DFT is key in understanding the deformation mechanism. Several studies [62-64,70,71] have found that N-terminated interface with [111] plane on both sides are the most stable for TiN-Al layers, judged from the surface adhesive energy and the energy barrier for shear. Moreover, e hcp-like stacking (see Fig. 1.9) has been found to be the most stable configuration. A similar behaviour was also shown with the shear strength, which has the implication on the deformation behaviour. A more careful analysis of pDOS found that while Al-Ti barely showed any bonding, *sp* hybridization was responsible for a stronger Al-N interface bonding. This effect is short-ranged, however, because no such an effect

was found for the subsequent layers of Al and N (see also Fig. 1.7). Interestingly, this arrangement might be prone to a chemically-induced change in a real condition, for AlN phase has been found for thicker (200 nm) layer thickness [71] but not on the thinner ones.

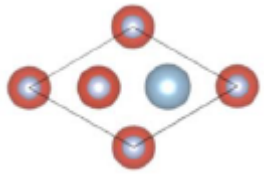

Figure 1.9: Top view of ideal interface stacking. Red is Ti, large blue Al, and small blue N. Source: [62]

Recently, a comprehensive study using a continuum model has been carried out to understand the stress nucleation and propagation on Al-TiN MCM [72]. Using CLS model, deposited dislocation is modelled as a result of a resolved shear stress on a certain slip system which exceeds the certain critical value. These deposited dislocations, which then can glide along the interface, allow for the metal and later ceramic layer at the interface to deform plastically. This co-deformation and gliding will apply shear to the interface, hindered only by the interface's shear strength, leaving a residual stress. Plastic incompatibility will then cause a strain hardening in the Al layer, reducing its resolved shear stress. Due to the high shear strength generated at the interface, the ceramic layer is prone to form cracks when a high tensile stress associated with shear is present.

When the layers are subjected to a compressive stress directed normal to the interface, a compressive stress will be applied parallel to the interface for Al layer. This will reduce the resolved shear stress for Al layer and cause hardening which consequently explain the observed high hardening rate. However, TiN layer will then respond to the

tensile stress perpendicular to interface. When the accumulated dislocations on either side of the interface interact, it will produce the transmission of the dislocation to the ceramic.

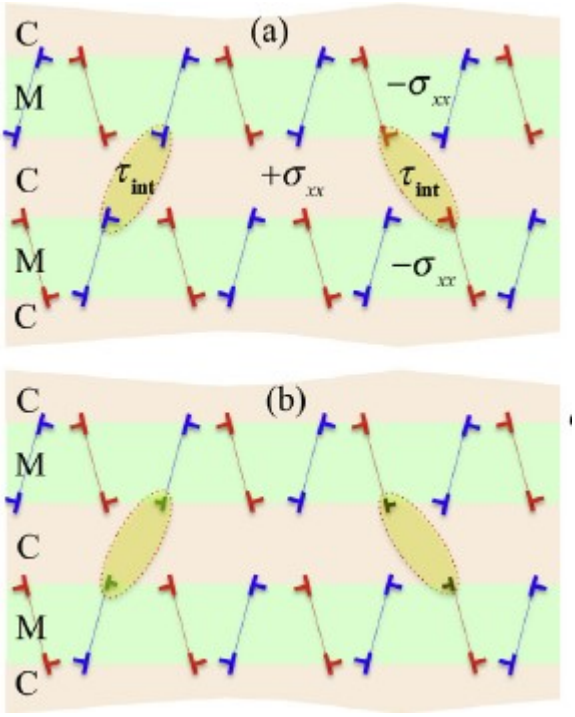

Figure 1.10: Schematic of deformation mechanism under compression perpendicular to the interface. Along the slip systems of the metal layer (M), compression will be applied parallel to the interface, shown on (a), depositing and accumulating dislocations. This will result in tensile (σ_{xx}) and force from interacting dislocations on adjacent metal layers (τ_{int}) on the ceramic layer (C). Magnitude of σ_{xx} increases with decreasing dislocation spacing, corresponding with higher plastic strains. With assistance of τ_{int}, dislocations glide in ceramic layer with resolved shear stress $m\sigma_{xx}+\tau_{int}$, shown on (b). Source: [72]

With a higher Al thickness ratio, the local shear stress will decrease for Al layer whereas the opposite is true for the ceramic counterpart. At the same time, the critical resolved shear stress (or more precisely, the Schmid factor) will increase for a lower bilayer period and TiN to Al ratio. This will effectively increase the transmission barrier, thus allowing for the transformation of TiN from brittle to ductile.

To conclude, I noticed many similarities between Al-TiN multilayers and other MCMs. Under compression normal to the interface, experiments have shown that low

period (4nm) with an equal volume ratio will give the highest strength and ductility of TiN. This can be explained by the strong local bonding between Al and N on the interface, which results in a large shear strength at the interface. This in turn allows for the dislocations to accumulate on the interface with a mobility that is hindered by also an increasing critical stress. A thinner TiN layer does not increase the overall resolved shear stress but creates a very high local stress, allowing a new path for dislocations to transmit beyond interface and hence produce the observed cracks.

Molecular Dynamics

The previous section has marked the difficulty of experimental method to properly understand the deformation mechanism of Al-TiN system and highlighting the benefits of computational approach. In this section, I will review two simulation methods, classical and *ab-initio* molecular dynamics, used in this study. I will discuss its basis and some intricacies that will need to be observed in the next chapter.

Classical Molecular Dynamics (CMD).

The main strength of physical science lies in its ability to gives reliably accurate, both in qualitative and quantitative sense, of the behaviour of a certain system given sufficient starting information. Moreover, if one can identify all relevant mechanisms of a process, one can, in principle, know the future behaviour of the system. Nowhere would this claim be truer than in field of classical mechanics. As Laplace proudly noted, if someone would give him the mass, position, and velocity of an object, he could give its trajectory into eternity. Of course, what he meant here is for one to solve the Newton equation of motion

$$\begin{cases} m_i \dfrac{\partial^2 \mathbf{r}_i}{\partial t^2} &= \mathbf{F}_i \\ \mathbf{F}_i &= -\dfrac{\partial U(\mathbf{r}_1, \cdots, \mathbf{r}_n)}{\partial \mathbf{r}_i} \end{cases} \tag{1.1}$$

where m_i and $\mathbf{r}_i$ are the mass and position of i-th object in a n-object system. The force $\mathbf{F}_i$ acting on the object is given as the derivative of the potential U given object configuration $(\mathbf{r}_1, \cdots, \mathbf{r}_n)$, giving what is termed the force field. Assuming one knows the correct potential U, this method can predict deterministically the trajectory of either heavy planets or tiny atoms. Thus, the question is then reduced to finding solution for n simultaneous differential equations. When applied to a system of atoms, I have just described the basis of classical molecular dynamics (CMD) [73].

Notice here that this model is very much simplified. In practice, one usually tries to integrate instead a set of coupled differential equations

$$\begin{cases} -m_i \dfrac{d\mathbf{v}_i}{dt} &= \displaystyle\sum_j F_2\,(\mathbf{r}_i, \mathbf{r}_j) + \sum_j \sum_k F_3\,(\mathbf{r}_i, \mathbf{r}_j, \mathbf{r}_k) + \cdots \\ \dfrac{d\mathbf{r}_i}{dt} &= \mathbf{v}_i \end{cases} \tag{1.2}$$

over a small timestep Δt and adjust the position and velocity at each step until the all of the time period τ is covered. Here, F_2 corresponds to force between 2 atoms, F_3 to 3, and so forth. Obviously, such decomposition is not always necessary, but can somewhat simplify the problem, depending the knowledge of the system's interaction. I shall insist here that this problem is far from trivial. Even though many numerical algorithms indeed exist, one needs to appreciate the challenge. The first MD simulation, simulating phase transition on hard-sphere model, involves only 32 atoms with square potential [74], which was improved later involving Ar gas with what I now recognize as timesteps [75]. I shall make a brief discussion later on solving this question of integration.

An inquisitive reader might at this point ask a question: why should this method work? Why should classical mechanics be applied to atomistic behaviour? The answer lies with statistical mechanics. MD method rests on three assumptions [76]:

1. The system, even under external forces, will settle to an equilibrium state
2. Any macroscopic event (i.e. observable events and parameters) can be described by $(\mathbf{r}_i, \mathbf{v}_i)$ for each atom
3. The system is ergodic: ensemble average is the same as time average. In other words, given enough time, the system can reach any microstate.

The last assumption here does not mean that any given state will reasonably reached or even has the same probability, regardless of the starting point. I shall show later an example of this. There are three systems, often termed ensembles, that are usually considered. The first one comes directly from Eq. 1.1. One important (unstated) assumption there is that mechanical energy does not change in time, because the system is isolated. So does momentum and angular momentum (at least in non-periodic boundary simulation). Thus, only three quantities need to be preserved: number of atoms, volume, and energy, hence the name NVE ensemble.

Of course, in reality, it is preferable to relate the simulation to easily observed quantities, for example volume, pressure, and temperature. In actual experiments, one often subjects their material at constant volume (such as in bulk modulus measurement) or pressure and temperature (as most experiment carried out at room temperature and pressure). In simulation terms, finding the first two is quite straightforward. For example, one can consider piston-like mechanism to control pressure. Controlling temperature, however, is much harder. Not only needing to consider the velocity of all particles, this can create additional constraint on volume or constraint evolution.

For this purpose, I need to introduce the idea of thermostat. This entity is analogous to using heat bath, which surrounds the material and regulates its temperature. Temperature is defined on MD by

$$\frac{k\,T_{MD}}{2} = \frac{1}{6N}\sum_{i=1}^{N}\sum_{j=1}^{3} m_i\,v_{ij}^2 \tag{1.3}$$

In other words, one can control the temperature by managing the average velocity under the correct distribution. Initially, temperature can be set by simply assigning randomly velocities so that they fit the Maxwell-Boltzmann distribution. The question is then how to move forward. The simplest scheme is of Andersen [77]: at each time step, one particle is chosen to interact with the heat bath. This particle's velocity is then randomly re-assigned following Gaussian distribution. While reaching the target temperature in the limit, the speed of convergence is sensitive to the collision frequency. One can remove this limitation with Langevin scheme: introduce additional force $F(t)$ that works as white noise. However, this method involves arbitrary choice and often shows over-correction.

A more elegant solution is the Nosé-Hoover thermostat. One can extend the Hamiltonian to include the heat bath explicitly:

$$H_{nh} = \sum_i \frac{m_i\mathbf{v}_i^2}{2s^2} + U(\mathbf{r},\mathbf{q}) + \frac{p_s^2}{2Q} + LkT\cdot\log s \tag{1.4}$$

where p_s can be understood as the momentum of heat bath variable. If $s(t) = 1$, I can recover the original Hamiltonian in the first two terms. This Hamiltonian will then translate to set of four coupled equations:

$$\begin{cases} \dot{\mathbf{r}}_i &= \dfrac{m_i \mathbf{v}_i}{s} \\ \dot{\mathbf{v}}_i &= -\dfrac{1}{m_i}\dfrac{\partial U}{\partial \mathbf{r}_i} \\ \dot{s} &= \dfrac{p_s}{Q} \\ \dot{p}_s &= \sum_i m_i \, s \, \dot{\mathbf{r}}_i^2 - LkT \end{cases} \tag{1.5}$$

The last two terms control the velocity, depending on the sign of s (and p_s), To make it more succinct, I can write the controlling equation as

$$\frac{ds}{dt} = \frac{Lk(T - T_{target})}{Q} \tag{1.6}$$

This equation provides feedback control to the instantaneous atoms in the simulation, providing ways for smooth transition. Parameter Q here determines the speed of convergence.

I return now to the question of calculating the time integral of the equation of motion. Take for example the NVE equation (Eq. 1.1). If the current position is known, for timestep Δt, I can write the next step using Taylor expansion as:

$$\mathbf{r}_i(t + \Delta t) = \mathbf{r}_i(t) + \dot{\mathbf{r}}_i\,(t)\,\Delta t + \frac{1}{2}\ddot{\mathbf{r}}_i\,(t)\Delta t^2 + O(\Delta t^3) \tag{1.7}$$

Using the expansion for negative timestep and some rewriting, I get

$$\mathbf{r}_i(t + \Delta t) \approx 2\mathbf{r}_i(t) - \mathbf{r}_i(t - \Delta t) + \frac{\mathbf{F}_i(t)}{m_i}\Delta t^2 + O(\Delta t^3) \tag{1.8}$$

where $\mathbf{r}_i(-\Delta t) = \mathbf{r}_i(0)$. This simple alghoritm is called Verlet algorithm [1], which is the most common scheme used.

[1] Yet another example of one can take credit of the simplest thing

The computational load can be reduced even further. As it turns out, the most time-consuming process is calculating these force expressions [78], so I need to create a distinction between the short-range and the long-range forces. By restricting the calculation to forces coming from groups within the cut-off range $\mathbf{r}_c$, I could reduce this consideration to $N_{neigh} = \frac{4\pi}{3}\rho r_c^3$ neighbours, where ρ is the atomic density. This restriction to short-range leaves the model then with the long-range force. Included in this class is Coulomb interaction, which may be prominent in ionic or biological system, where interaction can be found in every pair. In n-body system, the number of interaction grows as n^2, quickly turning the computation very costly for large n. There are two ways to handle this: either ignore these interactions or consider some approximation method such as particle-mesh algorithm [79]. I shall not dwell on this question, as most of the energy (and interesting interactions) are contained within reasonable choice of $\mathbf{r}_c$.

One must know when and how to apply their tool so they can be applied sensibly. CMD, as with any tool, has its limitations. There are four common issues that I must discuss here. First, one should know whether point-mass treatment of atom is justifiable. A quick calculation will show the de Broglie wavelength, which is a rough limit of quantum effect, at room temperature is about 0.2 Å for most atoms, which is still far below common atomic distance (1-3 Å). Thus, except for very light atoms or for operating at very high temperature, I can safely ignore the quantum effects.

Second, one should be aware that the limits of time and length scale involved. Even after millions of steps, which can be plenty for rich, i.e. interesting, systems, I would only last several nanoseconds. This can lead to highly misleading result. For example, one can simulate compression with perfectly harmless and reasonable strain rate

of 10^{-4}/ps. This would however translate to rate of 10^{8}/s, which is many orders of magnitude higher than any real experiments. Similarly, numbers of atoms involved are mostly limited to scale of millions. In other words, on the scale of (hundreds of) nanometres. One can use periodic images for homogeneous systems to mitigate this. Inhomogeneous systems, however, is still a challenge [76].

Third is the issue of timestep. Inherent in the Verlet algorithm (Eq. 1.8) is the dependence on size of timestep. Surely one can always choose smaller step size, although it would come with the cost of longer calculations.

Last, I shall address the issue of atomic interactions. CMD assumes instantaneous electron adjustment, which is represented by the surface of the potential energy. This rule out simulation of processes such as chemical bond breaking and forming (although there is a way around this) and electron excitation. More importantly, one then needs a potential that can approximates the wanted process. This is often done by fitting parameters such as elastic constants or volume from either into experimental data or DFT calculations into known relations. This process is time-consuming, making potential availability for many elements inconsistent, especially for systems beyond binaries. Moreover, it is sensitive to the input data, making one potential, despite having nominally the same elements, might not satisfactorily be applied to structures outside its original design (consider, for example, B1 and B2 TiN). This problem, called transferability, has always to be kept in mind for simulation. Indeed, developing one of such potential will be one of the major objectives of this study.

Nevertheless, with recent progress in computing power and parallelization algorithms, CMD has become popular simulation method due to its simplicity and ability

to simulate physical events of interests. There are many readily-used codes such as LAMMPS [79], IMD [78], MDACP [80], Camelion [81], and MDSPASS [82], with LAMMPS being the most popular choice, employing all methods mentioned above. Some, such as NAMD [83], CHARMM [84], and AMBER [85], are geared specifically for biomolecular processes. They show how successful CMD has become in fields from computational chemistry to materials modelling.

***Ab-initio* Molecular Dynamics (AIMD).**

Although the method is quite straightforward and works well for 'large' number of atoms, the lack of available, not to mention applicable, potential for many elements is a major impediment in application of CMD. Fortunately, density function theory (DFT) provides an alternative method. Recall the NVE Hamiltonian in classical case (that (1.9) results in Eq. 1.1). Instead of using a pre-determined potential, one can calculate the potential energy for the system directly from its electronic configuration at every step. I can then write the Hamiltonian as

$$H_{NVE} = \frac{1}{2}\sum_{i=1}^{N} m_i \, \mathbf{r}_i^2 + E[\phi(\mathbf{r}_1, \cdots, \mathbf{r}_N)]$$

where $\phi(\mathbf{r}_1, \cdots, \mathbf{r}_N)$ represents the Kohn-Sham one-electron wavefunctions for the electronic ground state of the system (just like assumed in CMD). Thus, the sequence is as follows: Ground state energy is calculated, which will then give information on the force. I can then advance the atoms to the next time step, just like in CMD, and repeat the same process. This DFT-based process is called *ab-initio* molecular dynamics (AIMD).

The earliest AIMD method is that of Car and Parinello [86]. This method relies on the rewriting of the Hamiltonian:

$$H_{CP} = H_{NVE} + \frac{1}{2}\sum_j \mu \int |\dot{\Psi}_j(\mathbf{r})|^2 d\mathbf{r} + L_{ortho} \tag{1.10}$$

The first term on the right-hand side is the same as Eq. 1.9. The third term introduces kinetic energy for fictitious mass μ, which represents the electronic degree of freedom. The last term then mantains the orthogonality of the one-electron wavefunction. The resulting equation of motion then takes the form

$$\begin{cases} \mu\,\ddot{\Psi}_i(\mathbf{r}) & = -H_{CP}\Psi_i(\mathbf{r}) + \sum_j \Psi_j(\mathbf{r})\Lambda_{j,i} \\ m_i\,\ddot{\mathbf{r}}_i & = \mathbf{F}_i \end{cases} \tag{1.11}$$

Done this way, I can sidestep the diagonalization of Kohn-Sham matrix in self-consistent calculation and surprisingly still almost always reach the same result. However, invention of more efficient diagonalization algorithm has seen more widespread adoption of self-consistent calculation in ready-to-use codes.

This DFT-based approach has now become a major tool in simulation, especially with highly-complex crystal or even amorphous structures. The same caveats on CMD still apply, especially concerning time and length limitation. Typical AIMD simulation involves less than 100 atoms with time scale below 100 nanoseconds. One should then be careful to choose their problem wisely. Also like in CMD, many codes are now available. For 'historical' reason, many authors see fit to make their code commercial: VASP [87], Gaussian [88], and Wien2K [89] although many open-source codes are also available: ABINIT [90], Siesta [91], and Quantum ESPRESSO [92]. To conclude, AIMD, despite of its scale limitations, is a reliable, if expensive tools to investigate the behaviour of complex structures.

Embedded Atomic Method

The previous section highlights the need for reliable model for interatomic interaction, especially for CMD. While in AIMD, one needs to be concerned only on electronic structure of a single element, the model in CMD generally relies on event-specific behaviours and mimicking observable parameters. In this section, I will review the general idea of such model and consider the highly successful model of embedded atomic method (EAM), which will be of particular interest to this study.

Basics of Potential System.

One major question in atomic modelling concerns the way atomic interaction should be represented. In the simplest model, one can imagine atoms, or to be precise the core, as simple positively-charged point particle, thus it follows simple electrostatic potential. In many ways, this simplistic view is not entirely wrong. For one, since the core constitutes the vast majority of atomic mass, both in number and in volume concentration, it would give an outsized contribution to interatomic interaction. Moreover, by adopting a positive charge, one can explain the separation between atoms as feature of the repulsive behaviour.

Of course, such a simplistic view would not suffice. For one, even though atoms would not naturally get arbitrarily close to each other (at least not without involving unrealistically high energy), they also would not, at least as observed in ordered molecules, move to any certain distance, because if this is true, atoms on the surface would simply drift away, making formation of any structure impossible. Therefore, I must also consider a form of attractive behaviour. In a sense, it is natural to make this addition, as Coulomb interaction allows both repulsion and attraction (such as expressed

in Yukawa potential), for example the relation between the core and the surrounding electrons. Moreover, this addition should allow a finite equilibrium point. That is, a resting position for the atoms, as reflected, for example, by the regular crystal spacing. In the end, I consider in this model the atoms as a certain point object with certain mass and (possibly) charge, without explicitly considering its constituent parts.

I shall not dwell on the exact nature of the interaction, as the exact mechanism of this interaction would be overly complicated and would involve unnecessary amount of time justifying the particular quantum mechanical phenomenon involved. I also would try to avoid using too fine a description of the atom, as it might restrict the generality of my model. It suffices to say that in the most basic form, interatomic potential can be expressed as the combination of repulsive and attractive behaviour of the core of the atom. I shall call this class of interaction as the pair potential.

There are some basic features of the pair potential that should be satisfied so the function can be applicable to as many systems as possible. First, I shall restrict ourselves to function where the primary variable is the distance. To see this, consider the isolated system in vacuum with two atoms. Because no external field on the system, the energy should solely come from the interaction between the two atoms. Moreover, because no other atoms exist, radial symmetry is achieved, so the system should be constant with rotation. Hence, the only relevant variable, in spatial sense, should then be the distance. Second, just like mentioned in the beginning, the pair potential should reflect repulsive behaviour so that no two atoms can get arbitrarily close. Naturally this often lead to a choice of rational function with some power, although other choices are also possible. Third, the function should allow at least one equilibrium position, such as one expected

from a regular crystal, in a many body system. Note that this does not necessarily mean such point exists in a two-body system. For example, consider a system of noble gases. However, I should also observe that the interaction energy vanishes as the separation increases. If one again imagines the aforementioned isolated system, as the separation grows, it should be expected the system to be reduced to the simple system of charges, so that only Coulombic interaction may apply. Last, to satisfy the formality of potential, the pair potential has to be smooth function in the expected region. At the very least, it should be expected that the function is continuous up to the second derivative, i.e. the force and its derivative should be continuous. This would ensure that the potential avoids inherently unphysical behaviour (since real-life force is always continuous).

Many functions satisfy the conditions outlined above. Unsurprisingly, most of them involve the rational function r^{-k}. which should easily contain the second property. One early example, which was derived from the gas equation of state, was the Lennard-Jones potential in the form

$$V_{LJ}(r) = \varepsilon\left[\left(\frac{\sigma}{r}\right)^{m} - \left(\frac{\sigma}{r}\right)^{n}\right] \tag{1.12}$$

Assuming σ is strictly positive, both the attractive and repulsive behaviours are represented. Here, the variables σ, ε, m. and n are to be determined by fitting and should vary depending on atom types. In particular, it should be pointed out that this would be this is the first mention of an empirical potential. In contrast to Coulomb potentials and its variations, the variable σ, ε, m, and n do not explicitly contain any information on the atom itself. In fact, this would be an important feature for most commonly-used modern potential. As the system grows more complicated, it would be more practical to fit the

parameters to some other independent data instead of considering every possible nuclear phenomenon.

Other functions have also been used before. One of the simpler type. Morse potential, was derived from the harmonic oscillator approximation of the well and takes the form of

$$V_{Morse}(r) = D_e[1 - \exp(-a(r - r_e))]^2 \tag{1.13}$$

The particular characteristic of this function is that the equilibrium distance r_e is specifically prescribed, which undoubtedly naturally arises from its derivation. This function does not purport to model a specific interaction (although implicitly it should only perform well whenever the harmonic oscillator model is quite justified). On the other hand, many other functions such as Lennard-Jones and its improvement, the Buckingham potential,

$$V_{Buck}(r) = A\exp(-Br) - \frac{C}{r^6} \tag{1.14}$$

are designed with classical gases, such as the noble gases, in mind. This is in fact a common occurrence, as the fully general forms have been inadequate to give accurate representation of an increasingly complex system. I shall for now mention in passing a pair potential, the ’empirical oscillating pair potentials’ (EOPP), which was specifically designed to model a not-necessarily crystalline system of metal. The function has the form

$$V_{eopp}(r) = \frac{C_1}{r^{\eta_1}} + \frac{C_2}{r^{\eta_2}}\cos(kr + \varphi) \tag{1.15}$$

Further discussion of this form and its relevance can be found in the next chapter, but it should be pointed out now that this function also contains an oscillating long-range

behaviour found in transition metals [93], hence it is potentially useful for purpose of this work. The variable φ serves here then as oscillation phase, not a physical angular dependence.

Improvements and Modifications on Pair Potential.

In the previous section, I have extensively reviewed the most basic form of potential function: the pair potential. It has been mentioned above that these functions should be a smooth function that contain both the repulsive and attractive behaviour expected from atoms. However, using only pair functions would restrict the effectiveness of any model. For example, consider a system consisting of carbon molecules. Even when the system is restricted mostly to 2-dimensional system like graphene, the carbon atoms would not take any position with the prescribed equilibrium distance. Instead, they would form a regular hexagonal (or pentagonal or any other shape) tiling. This shows a phenomenon, known as covalent bonding, shows that atomic bond, in contrast to the more traditional picture, can have a certain preferred direction, i.e. an angular dependence. This fact is however deliberately overlooked by the central pair potential. This would be used as motivation to apply some changes to the overall potential model.

I should pause here to stress the fact that any modification will not be take the shape of the pseudopotential model used in *ab-initio* calculations. In the pseudopotential model, one considers the atom as consisting of two parts: a frozen core and interacting valence electrons surrounding it. By applying some deliberate choice on where the boundary between the two lies, one can find an approximation of the wavefunction of one particular element, irrespective of other species that atom is interacting with. This might still satisfy the four criteria outlined in the previous subsection, although this is not

necessarily the case. The modifications that are concerned with here, on the other hand, needs to follow those criteria for MD simulation to perform smoothly. Moreover, their form tends to try mimicking actual behaviour of the atoms, such as the directional bonding. Due to the empirical nature of the determination of potential parameter, then, one must again be careful as not to put too much emphasis on the physical interpretation of a particular modification.

In general, one can classify most potential systems into two categories: those that use pair potential and those who does not. In the former, pair interaction is a major energy component, but additional terms are added so that the energy landscape favour a certain desired configuration or properly reflect certain behaviour, for example electronic property of metals. One example is the Embedded Atomic Method (EAM) [94], where a new term, the embedding energy, reflects the contribution from electron density of its neighbour. A further improvement, the Angular-Dependent Potential (ADP) [95], introduces further terms representing dipole and quadrupole contributions, thus penalizing deviation from a certain (in this case, cubic) structure and favouring certain angles (hence the name). The latter type, while avoiding a simple central potential in favour of a more complex description, often still keeps most of the principles of pair potential. One early example, the Tersoff potential [96], is composed of both repulsive and attractive functions. While the repulsive part is a simple Coulombic interaction, the attractive interaction considers not pair, but triplet of atom, as the effect of having a third atom in vicinity could change, in particular the angle, of formed bonds. This is meant to be by design, as the model was developed for carbon-based system. A more advanced model based on Tersoff potential is the Analytical Bond Order Potential (ABOP) [97],

which not only takes the idea of three-body potential, it also considers the bond order, that is the number of chemical bond, between two species in presence of third atom. Nevertheless, such model has not been widely applied for metals, although some results have come out to be quite favourable [97]. In the next section, it shall be discussed in detail a function of the first type, the EAM potential.

Review of EAM Potential.

As mentioned above, one cannot rely solely on the pair potential. While this is a quite simple and useful solution, it could quickly hit its limitations. One of them has been mentioned in the previous section. Another is the fact that often pair potentials are fitted using bulk properties of the said material [98], raising issues not just on its ability to handle a less-than-perfect crystal condition, such as grain boundary. Thus, a more robust approach is called for here. One approach to this problem is of course to solve the many-electron Schrödinger equation, a la DFT. Of course, this is hardly practical. On the other hand, this problem can be very much simplified if one assumes that the cohesive energy of the structure can be written as

$$E_{coh} = \frac{1}{2} \sum_{i,j;i \neq j} V\left(r_{ij}\right) \tag{1.16}$$

That is, the energy is sum of all bond pairs, which are independent of each other. One can quickly see that if this assumption is true, the scheme such as Tersoff's would be unnecessary. Moreover, for metal such as Li, its *fcc* and *bcc* phases show [99] different properties, suggesting that coordination number might plays role that would not be reflected if each bond is independent.

It would then be sensible to adopt a bonding relationship that can account for the coordination issue. This would be particularly useful for dealing with low-symmetry

problem, including cases of dislocations, grain boundaries, and even quasicrystal system. At the same time, one can add a form of pair potential to account for bulk of the binding energy, in line with the idea that the modification is a 'course correction' to the conventional pair function. Hence, the following *ansatz* of the energy in EAM was proposed [100]

$$E_{coh} = \frac{1}{2}\sum_{i,j;i\neq j} \phi_{ij}\,(r_{ij}) + \sum_{i} F_i\left(\sum_{i\neq j} \rho_j^a\,(r_{ij})\right) \tag{1.17}$$

Here, r_{ij} is the distance between the i-th and j-th atom, $\phi_{ij}(r_{ij})$ is a pair potential function, $\rho_j^a(r_{ij})$ is the spherically-averaged atomic electron density on the i-th atom due to the j-th atom, and $F_i(\sum_j \rho_j^a)$ is what shall be called here the embedding energy.

I should here elaborate more on the idea of embedding energy. The embedding energy F_i shall be defined as the interaction of the i-th atom at its nucleus with the background electron gas. One can imagine this background electron gas, which was contributed by the remaining atoms, as if one is trying to "embed" the atom at a certain location with host electron density. Certainly, this is aligned with the common idea that metals contain a 'sea' of electron. In many ways, this host-atom interaction should be more complex than simply dictating a certain type of bond. For one, this function envelopes many-body interaction, as one in principle considers the contribution from all atoms. It should be noted here that I have made some simplification, where the host density is regarded as superposition of individual contributions. In addition, my model should ideally also be able to represent the coordination, so any reasonable computation can, for example, account for the different properties on different structures. This

delicacy, all of which is packaged under the term of density, is one of the reason EAM has been a popular tool in simulation.

Notice here that this setup is not necessarily unique to EAM. Some other systems that has been proposed are either equivalent or even takes this idea further. For example, the Finnis-Sinclair N-body potential [101] would take the form of Eq. 1.17, although it allows different interpretation of the embedding energy. Another model that has been introduced above, the ADP model [95], takes the form

$$E_{coh} = E_{EAM} + \frac{1}{2}\sum_{i,\alpha}(\mu_i^{\alpha})^2 + \frac{1}{2}\sum_{i,\alpha,\beta}(\lambda_i^{\alpha\beta})^2 - \frac{1}{6}\sum_{i} v_i^2 \qquad (1.18)$$

where the last three terms are meant to force cubic symmetry upon the system through multipole expansions. A more elegant approach, the Modified EAM (MEAM), proposed by Baskes [102], does not favour certain cubic structure. While the energy still takes the form of eq. 1.17, the density function is allowed to vary by angle instead of averaged over an equidistant sphere. This consideration of angle is useful, particularly in cases where directional bonding is called for. This is the reason MEAM has been applied successfully in system where covalent bonding is prevalent such as Si [102], intermetallic alloy [103], and ceramic such as TiN, my object of interest [65].

Notice here that one must apply caution when using applying all of these models. Most of the time, these potentials are fitted with a particular reference structure in mind. For example, a Ti-N EAM potential, such as the one this work aims to produce, might not be appropriately applied for Ti_2N, because the compound has different structures and parameters than the fitted B1 TiN. In fact, this problem becomes particularly acute for MEAM, where the coordinated positions are ’hard-wired’ to the potential. Improvements from using a MEAM model might (and often) not transfer beyond the reference structure.

Note that there has been no mention so far of the actual form of the pair, embedding, and density functions. Originally [100,104], the pair potential was imagined as variation of electrostatic energy

$$\phi_{ij}(r) = \frac{Z_i(r) \cdot Z_j(r)}{r} \tag{1.19}$$

where Z_i, Z_j are the effective charge of atoms i and j. Moreover, the pair, energy, and density functions are fitted so that they and their derivative follow known relation of some basic mechanical and thermodynamical properties such as bulk modulus, elastic constants, and vacancy formation energies. Some requirements are later relaxed and modified [94], omitting, for example, the highly-simplified and restrictive electrostatic interaction, but imposing exponentially decaying convex function on the density. One then has the potential as tabular function with important parameter such as stable position as marker. This approach certainly guarantees high fidelity to the experimental result and prevents unphysical behaviour, at the cost of transferability of the potential due to its dependence on the bulk property of the reference structure.

There is of course a way to get around this reference structure issue. More recent fitting codes such as Potfit [105] and MEAMfit [81] advocate the so-called 'reference-free' method. In this approach, one defines (or more appropriately, chooses), just like in the classical models, the exact forms of the needed function, which are then fitted freely to given data. In particular, instead of considering data for bulk materials, one can simply consider now two atomic species at a time and find an appropriate fit. Needless to say, such fitted function should at least be smooth. However, the fitting process can accept more input and hence has become more flexible, as it can now be tailored to show certain

wanted phenomena, at the danger of allowing unphysical behaviours. This is a trade-off one must considers when choosing their model.

Last, I should comment on the actual choice of functions. Like mentioned just now, the ’reference-free’ method removes any constraint on the parameters. This leaves the problem of keeping reasonable behaviour to the chosen functions. For example, while not explicitly prohibited, the pair function should be expected to satisfy the four criteria of potentials. Some effort has been spent to find a more universal form, such as done in [106]. In the end of the day, one must consider properties specific to targeted structure so that it can be reasonably reproduced by the chosen function. The chosen functions for this study will be discussed in the next chapter.

Objective

In this chapter, a large part of the discussion has been devoted to observations on various properties, especially the deformation behaviours, of various metal-ceramic nanolaminates. Although there have been various experimental observations and continuum models developed to understand the dislocation mechanism, no conclusive answer has been found, especially on the questions on the nature of dislocation mobility and failure mechanism. The current continuum models are especially lacking in this respect because the difficulty of recognizing the nucleation of such phenomena. Thus, an atomistic approach is definitely warranted.

As has been mentioned before, the classical molecular dynamics simulation faces a major hurdle in the form of the absolute need for an effective interatomic potential. While models for binary systems such as Ti-N [65] and Ti-Al [107] have been previously published, no models for ternary Ti-Al-N has been known before. At the same time, the

highly accurate *ab-initio* method is simply insufficient for statistical problems such as deformation events, where scale is the key for accurate representation.

The embedded atomic method has been repeatedly shown to be effective in representing behaviours of not only metals but also ceramics. The model is versatile, in that it has been applied for wide range of materials, from alloys to ceramics. Moreover, the reference-free model, developed more recently, allows greater flexibility and adaptability of the model, which will be beneficial under the somewhat unstructured events of deformation.

It may then be concluded that the objective of this study is as follows: to develop an effective interatomic potential based on the EAM model in order to observe the deformation mechanism in Al-TiN nanoscale multilayers. Particular attention will be paid to how the effect of bilayer period and layer thickness ratio on the propagation of dislocation within the Al layer and how it relates to the eventual crack on TiN. Moreover, these will be contrasted with the behaviour of constituent materials. The detailed computational steps will be laid out in the next chapter.

COMPUTATIONAL DETAILS

Ab-initio Calculation

In order to accurately model the interactions on targeted structures to generate the interatomic potentials for the classical molecular dynamics (CMD) simulation, I need to first sample appropriate structures for forces and energy. These samplings are critical to the parameterization of the MD potentials. In this section, I will describe the procedure to create such samples.

Sampled Structures.

In order to ensure an accurate representation of the constituent parts of the bilayer structure, I also included both pure TiN and Al in my sampling. For TiN, I used rocksalt titanium nitride with a lattice parameter 4.225 Å. This lattice was obtained from Open Crystallography Database [108].

For the Al layers, I used two different structures as presented in Fig. 2.1. Naturally, I included the *fcc* phase that is thermodynamic stable phase for solid Aluminium crystal in room temperature. However, I also sampled the imaginary *hcp* phase of aluminium. I would justify this as a means to identify properly the dislocations in later MD simulations since the difference between *fcc* and *hcp* phase is only resided in the stacking order of the (111) planes, i.e. from $ABCABC$ layers in the case of *fcc* phase to $ABABAB$ layers in the case of *hcp* phase. By sampling the hypothetical *hcp* phase, I provided a more accurate description of the atomic stackings near the vicinity of (111)

dislocations where the *hcp*-like environment may have taken place within the crystalline structure.

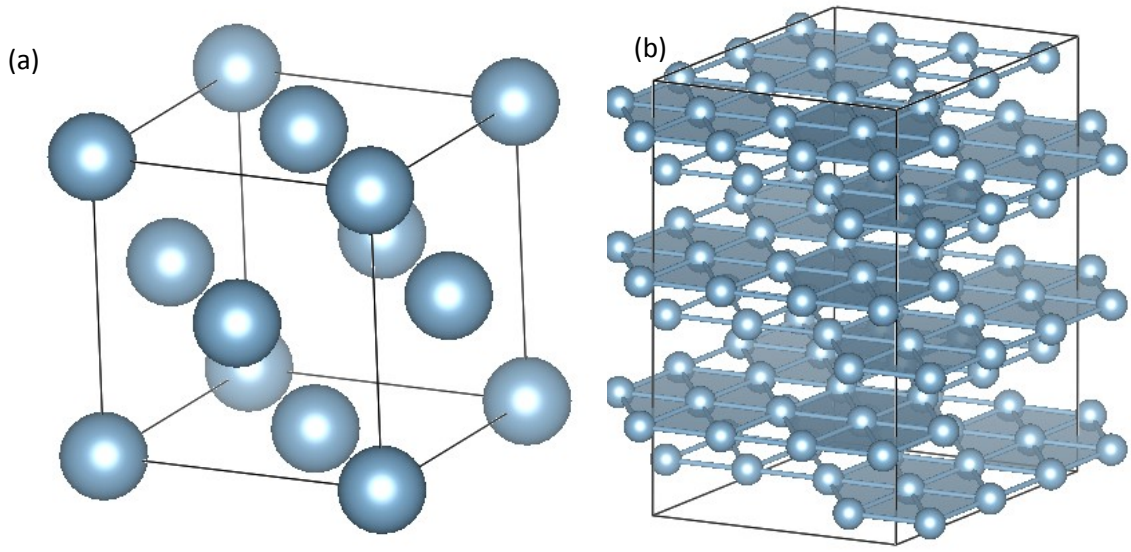

Figure 2.1: Sampled Al structures: (a) *fcc* phase (b) *hcp* phase

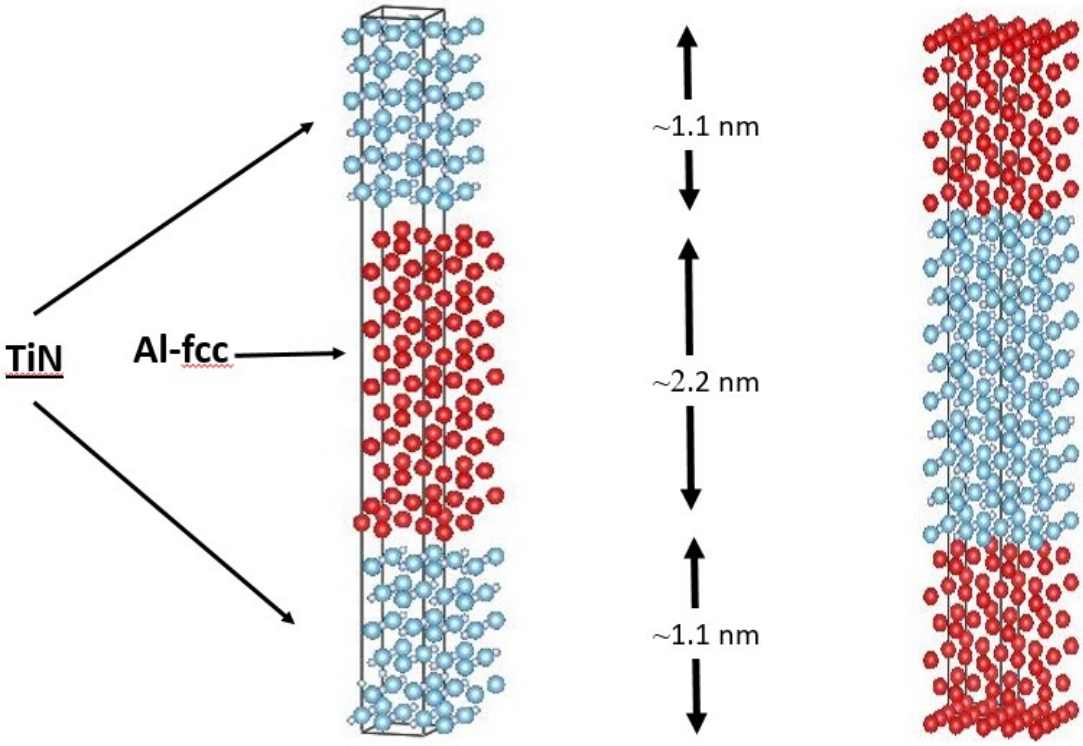

Figure 2.2: Sampled bilayer structures of Al-TiN. Blue is TiN, red Al. The thickness ratio is 1:1 with total thickness maintained at 2.2 nm

Because the aim is to model the TiN-Al bilayer structure, it is natural that I should also consider such a layered crystal as part of the in the sampling. I chose to follow previous experiment [46] and created a structure with equal thickness of *fcc*-Al and TiN (see Fig. 2.2). The model is periodic, but for completeness, I sampled both hypothetical cases when either Al or TiN is the middle layer.

Simulation Procedure.

Following examples from previous calculations reported by others [81,109], the structures are then simulated from first principles calculations in order to obtain critical information about their atomic forces and energies. The *ab-initio* molecular dynamics (AIMD) simulations was performed using Vienna Ab-initio Simulation Package (VASP) code [57].

The objective of this simulated sampling is to maximize the variation of Cartesian force data to be obtained with a relatively minimal computational resource. One way this could be achieved is by encouraging sufficient movements of atoms from their stable positions, hence allowing variations in their positions previously unseen on the initial structures. These variations will then trigger variations in forces that I subsequently used for the development of potential. I claimed to have attained this goal by running the simulations at a very high temperature, just below the melting point (or its supposed melting point), thus it is only shy of creating a melt structure. This method has been tried before and shown to be effective to explore, in particular, the quasiharmonic behaviour of high-temperature binary ceramic, which gives such ceramic its particularly unique properties [81,110]. This approach translated to using simulated temperatures of 3100 K, 2000 K, and 750 K for TiN, bilayers, and Al, respectively. For TiN, in order to induce a

faster convergence of parameterization process, small number of samples are also taken at lower temperature of 0 K, 300 K, and 2000 K.

A supercell of $2 \times 2 \times 2$ conventional cells were used for the constituent structure of the Al crystalline phase, while a single cell is used for the bilayers. The AIMD simulation for the TiN phase used both sizes, although a lower simulated-temperature TiN bulk phase was only calculated for the larger cell. For calculation efficiency, $3 \times 3 \times 3$ Monkhorst-Pack *k*-points sampling was chosen for TiN and bilayer, while $5 \times 5 \times 5$ sampling was used for Al. GGA exchange-correlation functional in form of PBE, as employed in the VASP package, was used. I chose a particularly high energy cut-off of 700 eV for both the TiN phase and the bilayer, while the lower VASP-recommended energy cut-off of 240 eV was applied for the Al simulations. The reason for utilizing this choice is to ensure that the predominant vibrational modes of TiN at very high temperatures could be properly captured by the CMD simulations [81]. Last, to create even more variations, the sampled cells were shrunk up to 20 % in cell parameters (so up to half of their initial volumes) for a total of 7 different volumes (including the initial). The exception is for TiN samples at lower temperatures, which are only taken at 5 different volumes (including initial). The simulation was then run for at least 0.5 ps before deemed to be sufficient for the next step. For visualization and analysis, the code VMD is used [111].

Force Fitting

In producing the MD potential, I used the code Potfit [105]. In this code, both force and energy information from the *ab-initio* calculation are fitted to the chosen

potential model, in this case the EAM model as has been discussed in Chapter 1. I will first describe the code Potfit before providing the details of the fitting process.

Overview of Potfit.

Potfit is a force-fitting code: it compares the force, energy, and stress of the input configuration with the current output and seeks to minimize its value functions by iteratively changing the potential functions' parameters. For this purpose, I took from the *OUTCAR* files produced by VASP that contained all of the atomic trajectories. I utilized the relevant information pertaining to the last atomic configuration, namely atomic positions, forces, stresses, and energies. Then, I chose a certain potential model that I believe will best represent my system. Once a model is chosen, then I have to pick a certain starting range for the potential function parameters that will represent the MD potential. Potfit will then compute all three information of force, energy, and stress of each atom contained in the input structure on its position using the current parameterized potential. These computed values are then to be compared with the supplied values from VASP and used to compute the targeted value functions in the form of

$$Z(\boldsymbol{\alpha}) = Z_D(\boldsymbol{\alpha}) + Z_C(\boldsymbol{\alpha}) \quad (2.1)$$

with $$Z_D(\boldsymbol{\alpha}) = w_e\, Z_{energy}(\boldsymbol{\alpha}) + w_f\, Z_{force}(\boldsymbol{\alpha}) + w_s\, Z_{stress}(\boldsymbol{\alpha}) \quad (2.2)$$

with $$Z_s(\boldsymbol{\alpha}) = \sum_{i=1}^{N_s} u_{s_i}\,(s_i(\boldsymbol{\alpha}) - s_i^0)^2 \quad (2.3)$$

with $$Z_C(\boldsymbol{\alpha}) = \sum_{r=0}^{N_C} u_r\,(A_r(\boldsymbol{\alpha}) - A_r^0)^2 \quad (2.4)$$

The targeted value function $Z(\boldsymbol{\alpha})$ on the current optimized parameter $\boldsymbol{\alpha}$ is a weighted squared sum of the current parameters' deviation from *ab-initio* result. On Eq. 2.3, the variable s can be replaced by either force, energy, or stress. The information of an individual structure (each atom for force, each structure for stress and energy) from

current parameter $s_i(\boldsymbol{\alpha})$ is then to be compared with the reference data from VASP (s_i^0) to compute the difference. The magnitude of this difference is then multiplied by a chosen weight of the particular configuration (u_{s_i}) and summed over all individual contributions. Summing for all N_s will give the total deviation (Eq. 2.2) of a property i.e. it indicates how far the value deviates from those calculated in AIMD simulations. At the same time, the function $Z_C(\boldsymbol{\alpha})$ (Eq. 2.4) computes the sum of all N_C constraint on the optimization process. This number of constraint N_C is determined by the type of potential, not by the input reference.

After the total value function is computed (Eq. 2.1), by incorporating the weight of each of the three parts (w_i), adjustments then can be made to optimize the parameter values $\boldsymbol{\alpha}$. Potfit provided two methods of minimization: simulated annealing and differential evolution. The conjugate gradient method is then run subsequent to either choice for further optimization. Differential evolution belongs to the class of genetic algorithm, where one considers the partially randomized evolution of each generation (iteration) that would minimize the value function $Z(\boldsymbol{\alpha})$ [112]. As this algorithm has been shown to work well [105] and requires fewer initial choices than simulated annealing, I chose the differential evolution as the minimization algorithm.

After the main algorithm has been completed, the parameters are supposed to be sufficiently close to the global minimum. To ensure that the true minimum is reached, conjugate gradient method is then used, which should converge relatively quickly. In order to evaluate the quality of fitting, a simple root mean square error of each quantity was computed by Potfit with [113]

$$\Delta F_e = \sqrt{\frac{Z_e}{N_e N_f}} \qquad \Delta F_s = \sqrt{\frac{6Z_s}{N_e N_f}} \qquad \Delta F_f = \sqrt{\frac{3Z_f}{N_e N_f}} \tag{2.5}$$

Last, it must be stressed here the adjustment of parameters has no particular physical meaning whatsoever. While setting bounds of search area might serve some deeper purpose, the optimisation algorithm, not physical laws, governed the movements of parameters and hence one should not dwell on particular interpretation of the numbers.

Potential Formalism.

The number of parameters may vary depending on the types of potential used. In this work, the EAM potential model is used. Recall that this model, as employed by Potfit, takes the form

$$V(r) = V_{pair_{sc}}(r) + V_{embedding_{sc}}(\rho) \tag{2.6}$$

which is used here to ensure the resulting potential and its gradient vanishes naturally at cut-off radius r_c (and hence the result is a smooth function).

The smooth cut-off equation in the form

$$V_{s_{sc}}(r) = \Psi\left(\frac{r - r_c}{h}\right) V_s(r) \qquad \text{with} \qquad \Psi(x) = \frac{x^4}{1 + x^4} \tag{2.7}$$

with s to be replaced by either 'pair' or 'embedding'. In this EAM model, there will be three functions: pair interaction, embedding energy, and density function. The pair function takes the form

$$V_{pair}(r) = \frac{C_1}{r^{\eta_1}} + \frac{C_2}{r^{\eta_2}} \cos(kr + \varphi) \tag{2.8}$$

This function is known as 'empirical oscillating pair potentials' (EOPP) [93]. While the first term represents the nearest neighbour attraction, the second term is supposed to model the nearest neighbours while taking account of the oscillations at long

range interactions. I shall make a note here that it is possibly superior to the more commonly adopted polynomial forms [114-115] in the original EAM formalism, because they might, as some of the previous trials have shown, fail to find the strong short-range repulsion. Generally designed to model complex metallic alloys and intermetallic compounds, this has also been successfully used for ternary system [109], which makes it of particular interest. Notice that although this function cannot take into account the prominent angular characteristic in the Ti-N covalent bonding, since it is designed to allow for irregular pattern in the structure (such as in quasicrystal), I hope to find good agreement over the whole structure (since the bilayers does not exactly have properties of regular crystal).

I apply the following functions to represent the embedding energy $V_{embedding}(\rho)$ and electron density $\rho(r)$:

$$V_{embedding}(\rho) = F_0(1-\gamma \log\rho)\rho^{\gamma} + F_1\,\rho \quad (2.9)$$

$$\rho(r) = \frac{1 + a_1\cos(\alpha r) + a_2\sin(\alpha r)}{r^{\beta}} \quad (2.10)$$

To adequately represent the electron density function, I concur with the argument in [115], just like in the aforementioned EOPP model, that the long-range behaviour has to contain the reflection of the Friedel oscillations normally observed in metals and hence to have both a decaying function, represented by the parameter β, and an oscillating function, here by the trigonometric functions, whose strength is determined by parameter a_1 and a_2 with oscillation regulated by α.

Last, for the embedding energy, I employed the simplified form from [106], which was modification of [116]. Note that this is quite different from the original EAM model. While the chosen function, just like in [114]. has been derived from the Rose

equation of state [94], its parameters do not have any particular attachment as far as the formats are concerned to any reference structure, because unlike [117], I have the capability to dictate an explicit form of the function, not as a tabulated function of the pair and density functions. In this sense, this method more closely resembles the 'reference-free' idea contained in [81].

Details on Fitting Procedure.

When one tries to count the number of fitted parameters, especially for EAM potentials, one should be astounded by the sheer number of fitted independent quantities that needs to be parameterized. If the smoothing parameter h is also counted (Eq. 2.7), then there are 7 independent parameters from pair function (Eq. 2.8) (C_1, C_2, η_1, η_2, k, h, and r), 4 from embedding function (Eq. 2.9), (F_0, γ, h, and F_1), and 5 from density function (Eq. 2.10) (a_1, a_2, α, h, and β). Because there are 3 species, there are 6 possible pairings and a embedding and density function for each, giving a total of 69 quantities to optimize.

In the face of such a daunting number of switches to adjust, one must be careful of not falling into the trap of working with more than what the fitting code can handle. Since Potfit requires an initial guess and is intended to search for boundaries for each parameter, one needs to make some preliminary choices of parameter values and reasonable bounds wherein the parameters might lie. However, since there are not many published MD parameters in Potfit format (in contrast to ready-use potential in format of, say, tabulated EAM potentials produced for LAMMPS), determining the starting point can be a great challenge.

To get around this difficulty, as it is often done when a more complex system is involved, I started with an estimate for the simpler binary TiN. For this purpose, I included the lower temperature calculations to improve the convergence. I optimized the weight of energy w_e to make up for the low number of data (26 energy input, compared to 168 entries of stress and almost 6000 for force) so that $w_e : w_f : w_s = 20 : 1 : 1$. The differential evolution method algorithm was used with convergence threshold 0.8. I chose the last iteration in OUTCAR file from each AIMD scenario. After the resulting Ti-N potential is deemed satisfactory, judged by the rms error (Eq. 2.5) and the reproduction of basic TiN parameters, these parameters are then used for initial guesses in the fitting for larger bilayer system. The same settings are used, but the force data are different. While still keeping only the last iteration of VASP calculation, I included the data for bilayer and both phases of Al, while excluding the lower temperature TiN to avoid unnecessary bounds on TiN, which might change in presence of Al. Fitting process was stopped after sufficiently low deviation is achieved.

Molecular Dynamics (MD) Simulation

Stable Structure Parameters.

After the fitting process was done, the resulting potential must be tested for reliability. For this purpose, I relied on the code LAMMPS [79] to perform the molecular dynamics (MD) simulation. Potfit, fortunately, produces a readily-used output readable in a format that is readable by LAMMPS.

The first, and undoubtedly important, verification procedure of the potential's capability is to reproduce basic structure parameters at room temperature. This is important, because all of the tested crystalline structures are known to exist in room

temperature, and thus any failure in reproducing these structures in this setting will place a serious doubt into the capability of the optimized potential parameters. For this purpose, I created a $20 \times 20 \times 20$ supercell of the three structures (TiN, *fcc* Al, and TiN-Al bilayer) as test inputs. Afterwards, I ran NPT simulation, where the atoms are assigned with semi-random initial velocities, following the Gaussian distribution, so that their expected initial temperature is as prescribed. At the same time, ambient pressure is set to zero and volume is relaxed, so that any change in shape and volume are due solely to the behaviour of the atoms instead of outside intervention.

If the structures are proven to be stable, I may also test for further mechanical and kinetics properties, such as shown in [118]. Whenever possible, I would test the for elastic constants, compression modulus (Eq. 2.11), Young's modulus (Eq. 2.12), cohesive energy (Eq. 2.13), and vacancy formation energy (Eq. 2.14). These values will then be compared to experimental or DFT-calculated values, whenever available.

$$K = \frac{1}{3}(C_{11} + 2C_{12}) \tag{2.11}$$

$$G = \frac{1}{5}(C_{11} - C_{12} + 3C_{44}) \tag{2.12}$$

$$E = \frac{9K\,G}{3K + G} \tag{2.13}$$

$$E_V^i = E_{defect-i} - E_{bulk} + E_{coh-i} \tag{2.14}$$

Deformation Study.

The main purpose of this study is to gain a better understanding of the nucleation and mobility of dislocations under a mechanical deformation. In particular, I am interested in matching and building upon experimental observations of the multilayer under a compressive loading normal to the interface, to match favourably with the nanoindentation experimental studies [49,55,69,119], at least qualitatively.

For this purpose, I created bilayer samples of various compositions to be used in LAMMPS using the data from COD [108] with the help of VESTA [120] and OVITO [121]. The samples are, following [69], created with $[111]_{Al}||[111]_{TiN}$ on $<110>_{Al}||<110>_{TiN}$ direction with N layer as the terminating ceramic layer. To create two interfaces, the Al layer is placed between two equal halves of TiN layer with a separation of 1.5 Å. To eliminate lattice mismatch, the Al lattice is stretched to match with TiN's. Following [46], the base thickness of each layer, called ratio 1 afterwards, is 2.7 nm and other thickness are multiple thereof. To study the effect of overall layer thickness, four samples of various of TiN:Al thickness ratio are created: 1:1 (period 5.5 nm), 2.5:2.5 (period 14.5 nm), 5:5 (period 27.5 nm), and 9:9 (period 51.6 nm). At the same time, ratio effect is observed by comparing samples with ratio 1:9, 5:5, and 9:1, all with virtually equal period. The aforementioned samples are then subjected to uniaxial compression along z-axis, normal to the interface. Supercells of size at least $20 \times 20 \times 1$ are used as it allows the trade-off between allowing space for dislocation glide and optimal computational cost. The periodic boundary condition is used on all three axes, creating an infinite array of multilayers. The sample undergoes the first energy minimization with an energy convergence of 10^{-5} and a force threshold of 10^{-7} eV/Å. Then it is NPT-equilibrated under a zero ambient pressure at room temperature (300 K) for 40 ps. Last, it is compressed while with the relaxed pressure on x- and y-boundary conditions. The following strain rates are used to study different compressive responses: 5×10^8 /s, 2.5×10^8 /s, 2×10^8 /s, 1×10^8 /s, and 5×10^7 /s. The sample is compressed until a nominal strain, the overall layer thickness reduction, reaches 20% or the simulation breaks due to lost atoms, whichever occurs earlier. As a reference, the

same procedure was also used for each constituent material in the bulk form. The OVITO and AtomEye [122] codes are used for the analysis and visualization of the simulation results. In the next chapter, I shall lay out the results in more details, but the reader is referred to this chapter or to the appendix for further information.

RESULTS

Ab-initio Molecular Dynamics

The AIMD steps are carried out for all samples with various temperature and compression levels. In Fig. 3.1, I present the radial distribution function (RDF) plots of (a) TiN at various temperatures and (b) Al-sandwich bilayer at various compression level (not all shown here). Recall that by applying AIMD at high temperatures, it is expected to find larger variation of atomic configurations in my samples. This approach seems to be successful, judging by the significant peak broadenings in the RDF plots (Fig. 3.1(a)). Similarly, one should expect to find to find larger and more accentuated forces by applying various levels of volume compression. Again, this goal is seemed to be achieved, although it results in two additional and potentially challenging consequences. One, the very high level of pressure criteria chosen inevitably slows the convergence of self-consistent steps, increasing significantly the time needed to reach the targeted equilibration time. Two, as shown on Fig. 3.1(b), there is a significant shift in the RDF peaks which lowers the length with accompanying broadening of the overall peaks. This suggests that as the free (unoccupied) space is significantly reduced, atom movements during MD simulations are significantly restricted and as a consequence, the space restriction might instead entrap them to artificially fixed positions. Hence there is a point where the benefit of extending the compression level will be outweighed by the movement restriction of the atoms, possibly leading toward artificially stagnant configurations. Nevertheless, for most of the data, they can be deemed to be quite sufficient for the purpose of force fitting procedures to generate the MD potentials.

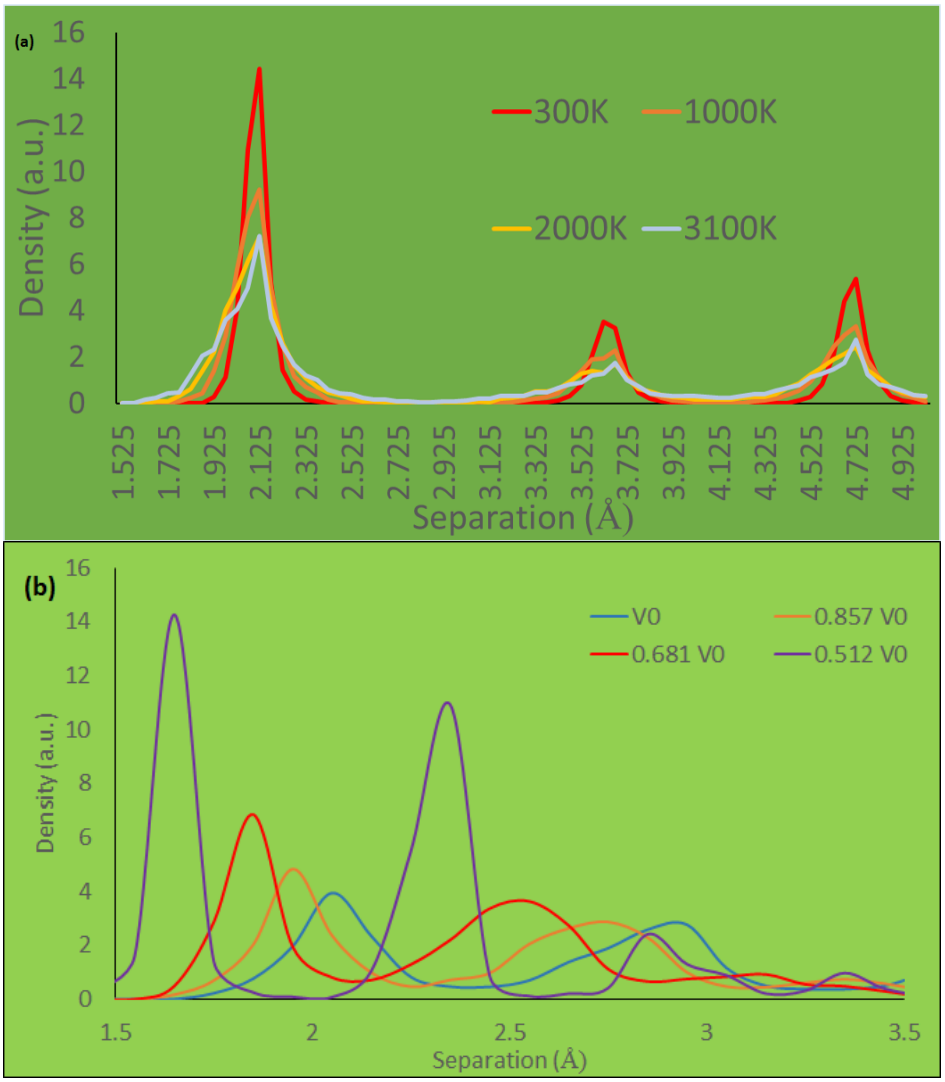

Figure 3.1: Radial distribution function (RDF) of (a) TiN with varied simulation temperature (b) Al-sandwich bilayer with varied volume. Notice the peak broadening with increasing temperature in (a) but sharpening with larger compression in (b).

Produced Potentials through Force Fitting

One way to judge the quality of the fit is to compare the energy landscape of the input configurations from *ab-initio* simulations with one resulted from MD simulations using the fitted potential. In Fig. 3.2, I compare the energy of each configuration and Cartesian forces of each atom from the same atomic trajectory positions. A well-converged potential would have reproduced the input data, thus creating such a plot

whereby the generated potential would have resulted in a perfectly 45° diagonal line, as shown in Fig. 3.2. The calculated rms deviation of the fitting procedure results in 317.2 meV/Å (25.5 %), 77.1 meV (6.6 %), and 83 kPa (48.2 %) for force, energy, and stress, respectively. Although these values are relatively higher than the published results of other works in ternary EAM fitted by Potfit (for example, the reported Al-Pd-Mn ternary gave 265.6 meV/Å, 19.4 eV, and 99.9 kPa [109]), it is necessary to point out the strong directionality of the covalent bonding present in TiN and to a lesser extent Al-N on the interface unlike that in Al-Pd-Mn system. This additional directionality is not completely captured by the EAM construct, thus adding an extra layer of challenge in terms of generating perfectly suited many-body potentials [110]. To enhance the fitting outcome, one could add an angular dependency into the EAM potential, an effort that can be done in the future, building on the EAM model that I established. A comparison with another nitride system characterized also by the presence of covalent bonding, the U-N binary system for example [123], gives a comparable level of error consistent with the result here. When the complexity of the bilayers is factored in, certainly a greater flexibility for the error range should be allowed.

The acquired data obtained from the Cartesian force divergence can give a better picture on the convergence level for individual atoms. Although Al, with its easy slip and soft structure, has a presumably less rigidity with respect to the dynamics of the structure during simulations, the percentage of Al with above rms deviation is only 19%, compared to 36% and 30.7% for Ti and N, respectively. This suggests that, for Al, the approach of fitting to bulk *fcc* and, more importantly, the alternative *hcp* structure gives a considerable adaptability to the fitting process of the potential. On the other hand, higher

Ti and N errors might instead reflect on the inherent weakness of EAM model due to the anharmonicity not fully captured by EAM. At the same time, combination of the stress and energy error shows that largest deviations are consistently produced by the configurations with a large compression, especially for Ti atoms. This might suggest that the while such a volume reduction allows for a sampling of larger forces (see Fig. 3.1), after a certain point, it may have exceeded its usefulness as there is not enough space allotted for the molecular vibration, giving false sense of rigidity to the structure. Same conclusion is reached by analysis of the RDF plot.

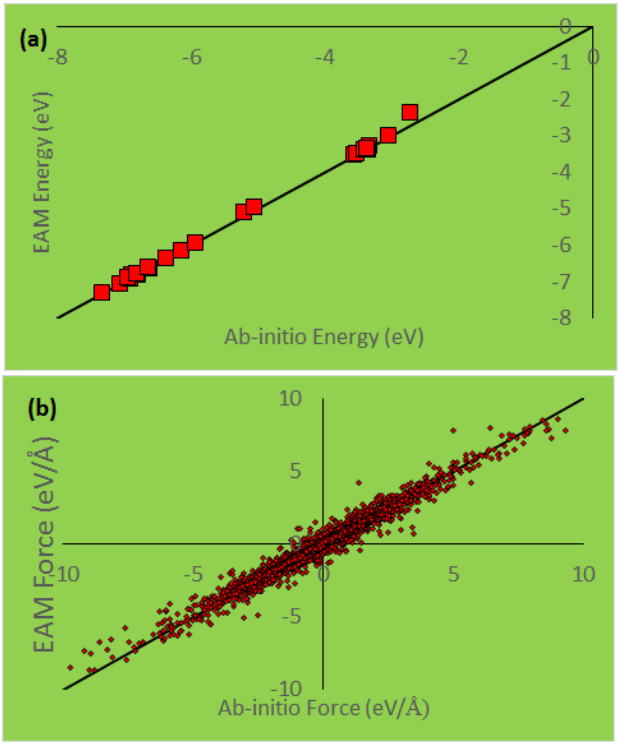

Figure 3.2: Comparison between *ab-initio* calculation and Potfit-produced EAM result for (a) force and (b) energy. Diagonal line added to guide the eyes.

I have also evaluated the fitting results from individual functions of the potential. In Fig. 3.3, 3.4, and 3.5, the pair, embedding, and density functions are plotted, respectively. It is easy to see that the embedding and density functions plots, at least qualitatively, are in agreement with the common interpretations of them. For example,

the electron density should rapidly decay as a function of distance. Similarly, one should expect the minimum of embedding energy being a proxy for a relatively stable position, a feature reported by other metallic and nitride systems [107,123,124], but curiously not in the complex metal system Al-Pd-Mn [109]. Thus, both the embedding and density functions are at par with other EAM results, although again one must not put too much emphasis on this interpretation.

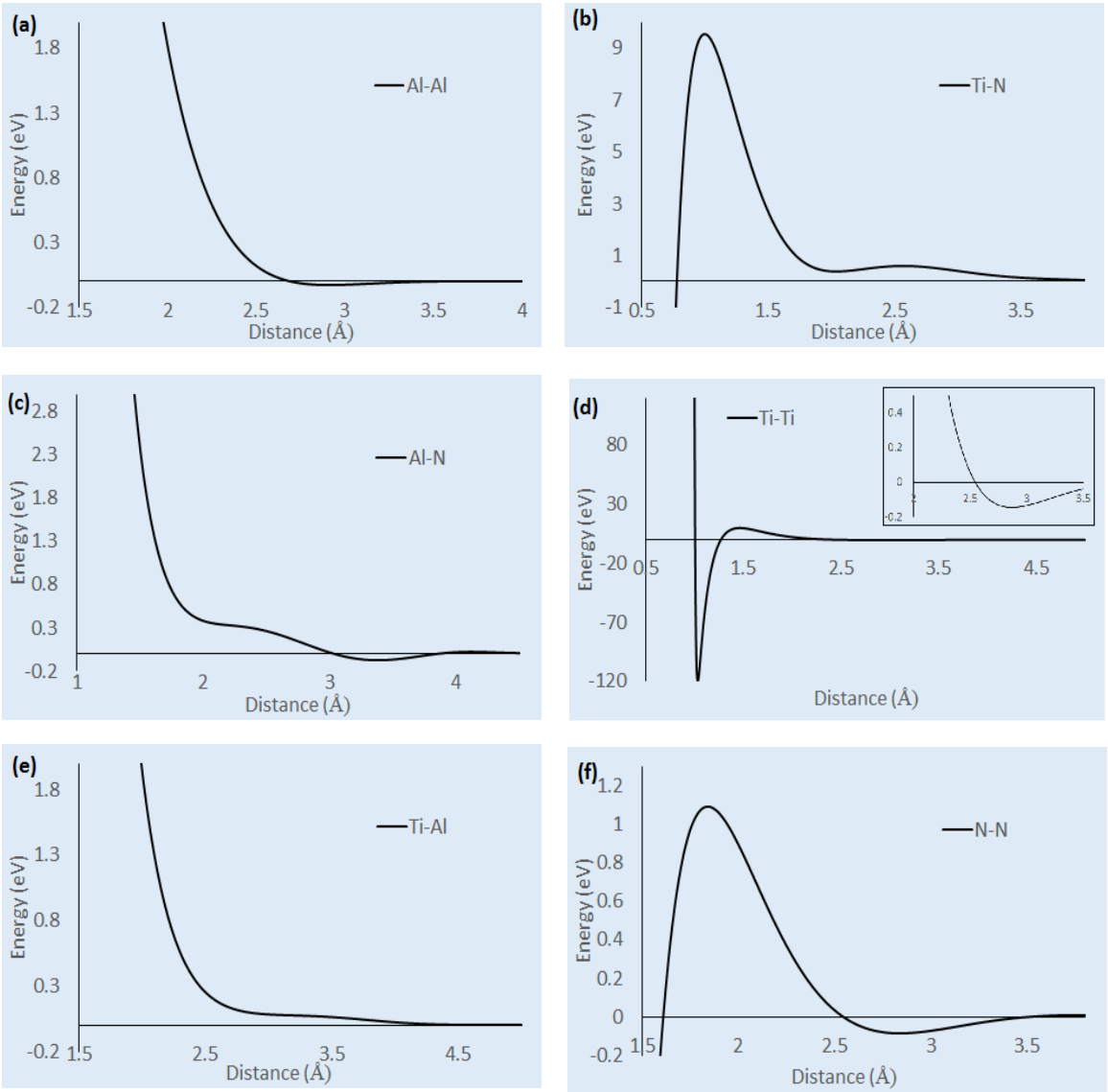

Figure 3.3: Pair interaction functions of (a) Al-Al, (b) Ti-N, (c) Al-N, (d) Ti-Ti, (e) Ti-Al (f) N-N. (a)-(c) has nearest neighbour relation, while (d)-(f) does not.

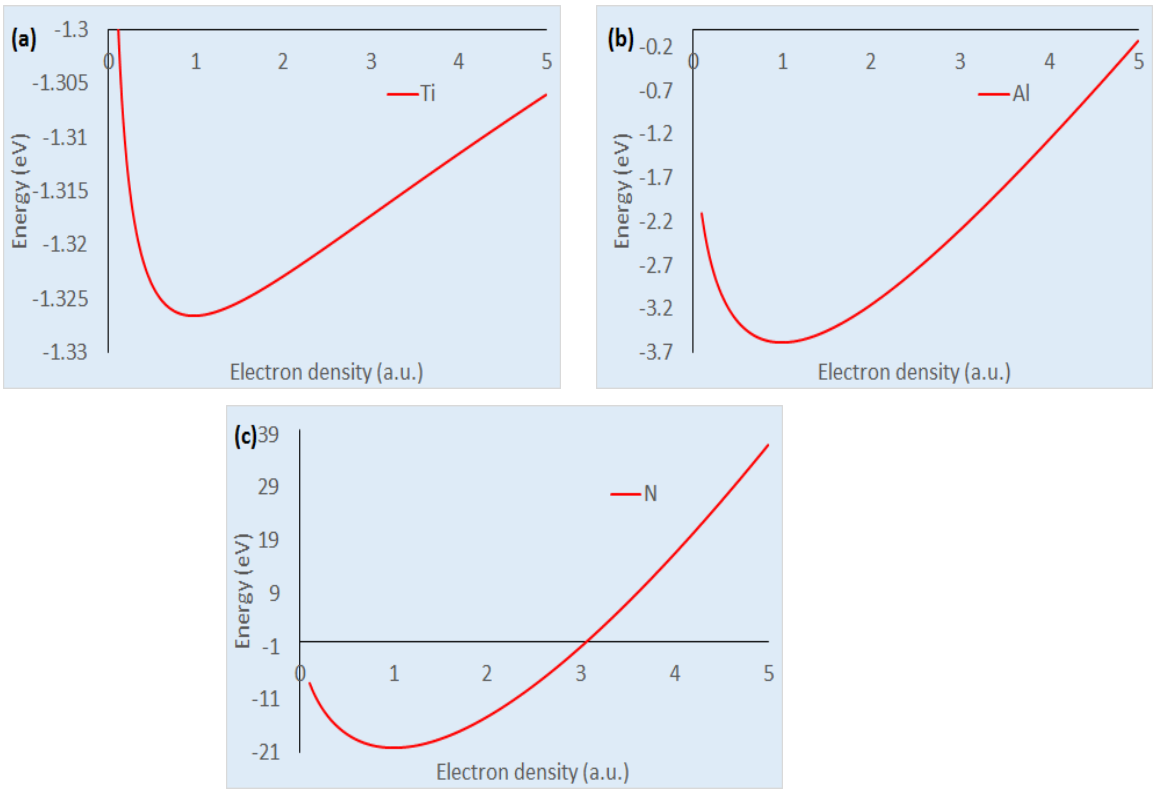

Figure 3.4: Embedding energy functions of (a) Ti, (b) Al, and (c) N

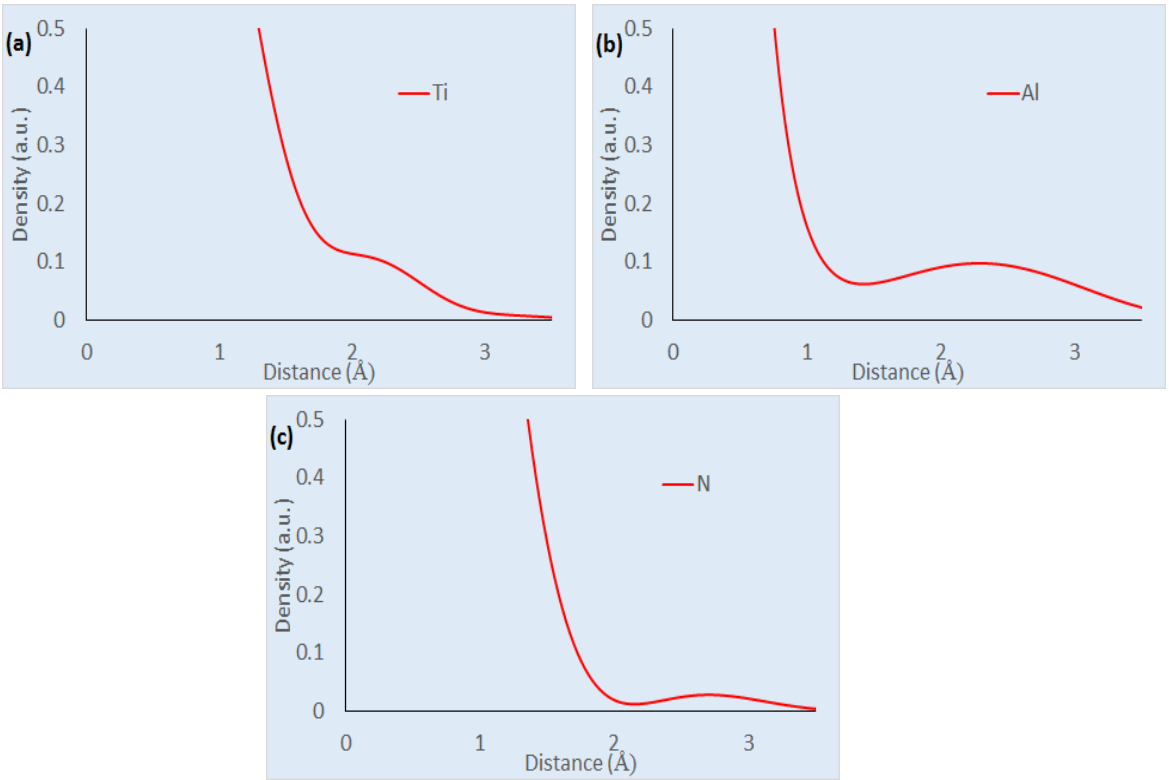

Figure 3.5: Electron density functions of (a) Ti, (b) Al, and (c) N

The interpretation of the pair potential is a not so straightforward. In Fig. 3.3, (a)-(c) are pairs that exist as nearest neighbours in any of the input configurations, where (d)-(f) are pairs that only exist as second nearest neighbour. The Al-Al interaction, for example, shows a potential well at just under 3Å, a feature often shared by well-fitted bulk Al or systems containing it [107,125]. However, the depth of the well is below 0.05 eV, less than other findings. This might be the effect of uncertainty induced by the addition of the imaginary *hcp* phase. Similarly, Ti-N interaction shows nearest stable position at around 2.1 Å, which agrees with other MEAM potentials [65,66,126] and the input TiN lattice parameters. I cannot quite explain however, the finite barrier peaking at around 1 Å, which implies that arbitrary separation is possible. This might note bide well for application in high energy environment, such as in high temperature simulation. Last, it should be noted that it is surprising to see a shallow and far-positioned well of Al-N interaction considering the strong bonding of Al-N. This might reflect on the weak $[100]_{Al}||[100]_{TiN}$ interface found in my input, as shown by DFT calculation [62].

The picture is somewhat more complicated for the second nearest neighbour pairs. For example, Ti-Ti shows an uncharacteristically deep well, indicating some 'hard-wiring' of their relative positions, which is not seen on other studies. Similarly, the well position of just 1Å can be categorized as unphysical, although the second well at around 2.8 Å (see inset) is aligned with other studies [65,107]. On the other hand, I cannot identify discernible stable position of Ti-Al pair function. This, I would claim, is consistent with the very weak shear strength of such interface from DFT study [127]. Nevertheless, the overall current MD potential provides a reasonably comparable level of error range to those found in other systems marked by dominant covalent bonds e.g. U-N.

Overall, this unique approach of combining small number of reference structures with high simulated temperature and various levels of compression has been found to work reasonably well for the complex Al-TiN bilayer system in reproducing potential interactions that agree with general expectation. The errors are found to be reasonable in comparison to another nitride system. Moreover, most of the pair functions reproduce the stable separation at bulk reference structure. Some of the errors can be attributed to the weakness of the EAM model, especially in representing the directionality of covalent bonding. At the same time, I find it challenging to, at least qualitatively, match the expected features of the interface. Further testing is needed to verify this potential, which will be done in the next section.

Classical Molecular Dynamics (CMD)

Stable Structure Parameter and Properties.

The simplest validation of the fitted potential is its ability to reproduce the parameters of bulk input structures. For this purpose, I utilized CMD simulations using the code LAMMPS. In Table 3.1 the stable unit cell parameters of TiN under NPT simulation are presented, where simulation temperature and pressure are held constant at 300K and zero ambient pressure. At the same time, I calculated the elastic constants, bulk modulus, and Young's modulus. This simple verification finds that the divergence is about 1% for lattice parameter and less than 8% for most elastic coefficients. Notice however that this model overestimated C_{12} and underestimated C_{44}. Many DFT calculations and another MEAM potential found close estimate of C_{44} but consistently

underestimated instead C_{12}. Nevertheless, the calculation results are found for TiN to be on a par with experimental and DFT studies.

Table 3.1: Elastic constants and cell parameters of TiN compared to [32], [128], and [129].

Elastic Constants	Here (GPa)	Expt. (GPa)	Cell Param.	Here	Expt.
11	638.6	625	Volume (Å^3)	73.3	76.24
12	203.7	165	Cell Param. (Å)	4.184	4.24
44	132.4	163			
K	348.7	320			
E	540	556			

Similarly, the same calculations are repeated for both the stable cell parameters and elastic constants for bulk Al at 300K on Table 3.2. Notice here that although the model obtained very good agreement on the lattice parameter, the elastic coefficients are consistently underestimated. This behaviour is not typical of EAM model, as shown by several other developed MD potentials for Al [125]. On the other hand, none of the said potentials are fitted with *hcp* phase, which is believed to distort the isotropy of cubic Al. That said, the distortion is believed to be ultimately limited, as the other calculated C_{ij} components and Poisson ratio are consistent with reported values.

Last, I will evaluate two energy parameters to probe the stable energy parameters of these two structures: cohesive energy and vacancy formation energy. It is found (Table 3.3) that the cohesive energy, just like the stable lattice parameter, is reproduced reasonably, although the vacancy formation is found lower than reported values. For TiN, on the other hand, the difference is quite significant. For example, it is well-known that nitrogen point defects are the dominant defect phenomena in crystalline TiN_x [65,138], so

one should expect that Ti vacancy energy to be higher than N to reflect the experimental observations. It should be noted, however, that even when MEAM model was applied, these calculations are still unable to produce the values found by the more reliable DFT calculation. Most probably, this is because the published data, unlike the unpublished vacancy-optimized MEAM model [131,132], was, just like the work here, not optimized for this purpose. Overall, however, these calculations find that the model produced potential can provide reasonable estimates of some structural parameters. Further refinement of the input parameter would be needed here.

Table 3.2: Elastic constants and cell parameters of *fcc* Al compared to [125] and [130].

Elastic Constants	Here (GPa)	Expt. (GPa)	Cell Param.	Here	Expt.
11	88.3	106.7	Volume (Å^3)	69.32	66.41
12	53.2	60.4	Cell Param. (Å)	4.108	4.049
44	36.4	28.3			
K	64.9	75.8			
E	48.4	70.4			

Table 3.3: Cohesive energy (E_{coh}) and vacancy formation energy (E_V) for bulk Al and TiN. Ref. [65] is my calculation from published MEAM parameter.

E_{coh}	Here (eV)	Other (eV)	E_V	Here (eV)	Other (eV)
Al	-3.72	-3.39 [133]	Al	0.32	0.66 [134], 0.7 [135]
TiN	-9.71	-6.8 [136] -7.16 [137]	Ti	-1.54	1.32 [65], 2.76 [138]
			N	2.15	-11.07 [65], 2.41 [138]

Dynamical Events: Responses Under Deformations.

In this section, I will present result of the compression test on Al layer placed between two TiN layers on various thickness. The basic strain rate, referred as R_0, is 10^9/s. All other rates will be expressed as fraction thereof. Samples with different thickness configurations are referred with their TiN:Al volume ratio, with thickness ratio 1 equal to 2.7 nm. For example, sample called 1:1 has equal volume TiN and Al layer each 2.7 nm thick (with total thickness, termed period, of 5.6 nm), but sample 5:5 has layers each 13.8 nm thick (and period 27.5 nm). See the previous chapter for more detail.

General Observations on Stress-Strain Response to Compression.

In Fig 3.6, I compare two different sample effects: layer volume effect and strain rate effect, one held constant when changing the other. To help comparison, the result of compression of bulk Al and TiN are also added. Similarly, an inset on Fig. 3.6(b) around the end of the elastic zone was attached for closer observation.

It was found that increased strain rates delay the occurrence of dislocation and the eventual failure. For example, in 1:1 samples shown on Fig. 3.6(b), eventual crack appeared at 19.4 % strain under $R_0/2$ strain rate. The failure came sooner, at 18.5 %, when the rate is reduced to $R_0/10$. Similarly, as shown in the inset, the onset of dislocation, marked by the peak of the elastic regime, is hastened by decreasing strain rate. This phenomenon is not surprising and similar trend has been reported for ceramic [139], nanocrystal metal [140], hard metal alloy [141], ceramic bilayer [142], and metal multilayer [143]. This is particularly true for nanoscale materials, which are more sensitive to rate change, although the sensitivity might vary from quite low for metal [143] to relatively high for ceramic [138,142]. Generally, one can expect increased

elasticity, ductility, flow stress, and hardness with increasing strain rate. The trend on tensile (or compressive) strength is not always consistent, although increasing trend can be expected. It is quite hard to pinpoint the exact mechanism, but explanations often involve creep of dislocation at slower rate, such as that diffusing through grain boundary, in addition to regular boundary slip on the slip planes. Moreover, higher strain rate seems to delay the dislocation nucleation and strain hardening, thus allowing more ductile response to compression. It would not be possible to observe creep diffusion as the utilized simulated strain rate is far higher than that of experiment condition, but some plane slips can still be observed in this system.

One can understand the volume phenomenon in Fig. 3.6(a) as two parts: period effect and ratio effect. In Fig. 3.7(a), various bilayer periods (total thickness) with equal ratio under strain rate of $R_0/4$ are compared. One thing to notice is that the behaviour between periods are quite similar, with possible difference in transition to plastic zone, where thicker samples see unloading up to 30% of stress but virtually none in the 1:1 sample (see inset), suggesting increased plasticity at thinnest layers [69]. Moreover, one can observe a serrated texture of the graph for 9:9 sample, suggesting lower absorbance of stress, necessitating stress diffusion to equilibrate. More careful analysis needs to look at the stress distribution in these thicker samples.

In Fig. 3.7(b), I compare different volume ratio with virtually equal bilayer thickness under rate $R_0/4$. Both the bulk TiN and Al are also added for comparison. Expectedly, the bilayer's behaviour resembles the layer with higher content, hence softer 9:1 and harder 1:9. At the same time, notice that higher ceramic content correlates with higher degree of brittleness, as shown by earlier onset of dislocation and crack on 9:1

sample compared to 5:5 sample. Even more surprising is bulk TiN's ability to maintain more or less elastic response, compared to early dislocation onset in 9:1 sample.

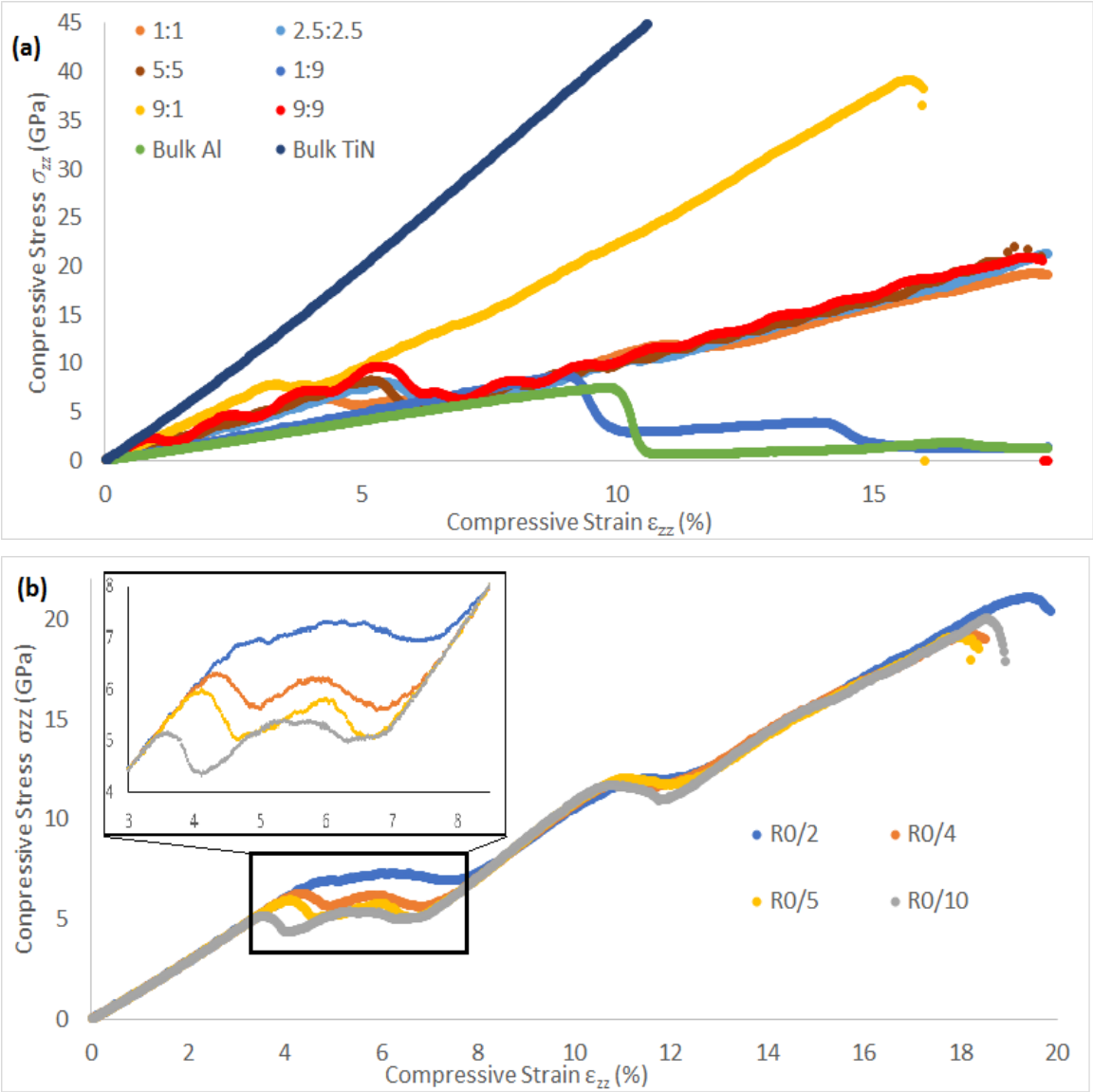

Figure 3.6: Comparison between (a) different volume ratio and thickness with rate $R_0/4$ (b) different strain rates on 1:1 sample. Inset on (b) focuses on end of elastic zone.

Last, I compare the samples' response to those expected from rule-of-mixture (ROM), shown of Fig. 3.7 (c). I calculated this as weighted average of stress in bulk TiN and Al, proportional to the sample's composition. As reported in [52], the bilayers show lower than expected elasticity. Not to mention is also the earlier onset of dislocation

observed in all of my samples (for example on Fig. 3.7(b)). Overall, however, it should be noted that toughness and stability of the multilayers increase with decreasing bilayer thickness with volume ratio held constant and strained at a faster rate. In the next three sections, I will explore the samples' behaviour under three regimes, keeping in mind observations made here. I will also try to find the explanation behind some of the phenomenon observed in stress-strain graph from the structural change during compression.

Elastic Regime.

In this section, I will evaluate the behaviour of the multilayers in the elastic zone, marked by the linear increase of stress early in the compression. I will evaluate the elasticity of each sample and the point of onset of deformation. I will also observe the reasoning behind serrated response of 9:9 sample. Last, I will make some observations on the transition to the plastic region. All observations, unless noted, will be for rate $R_0/4$, although the result is generalizable to other rates.

The easiest measure of elasticity would be the Young's modulus E. In Table 3.4, I compare E for all of the samples as measured from the slope of the stress-strain graph. Unsurprisingly, bulk TiN and Al show elasticity in the high and low extremes, respectively. Also unsurprisingly, higher elasticity correlates with increasing ceramic content, reflecting more on the property of TiN. Similarly, it can be shown that for equal volume ratio, E increases for sufficiently thick layer, an observation also made in nano-indentation experiment [55]. It has been suggested that uneven strain level between the layers, which is higher in Al, might explain this part of period effect, in addition to shear strength of the interface [47].

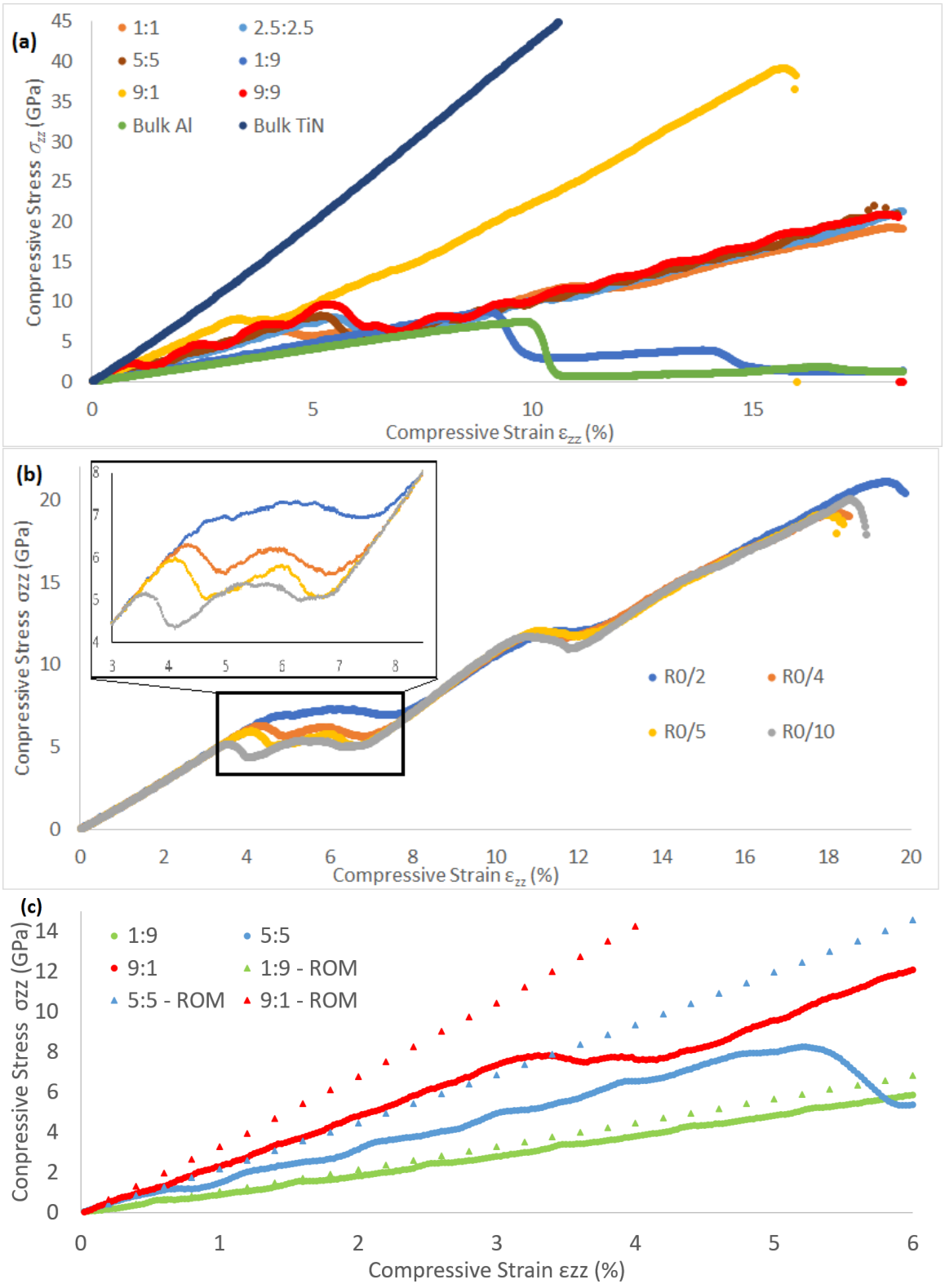

Figure 3.7: Comparison between (a) different bilayer period with rate $R_0/4$ and equal ratio (b) different ratio with roughly same bilayer period on rate $R_0/4$ (c) response of different ratio compared to that suggested by rule-of-mixture (ROM).

Table 3.4: Young's modulus (E) for each sample in rate $R_0/4$, grouped by type, in GPa. Notice that 5:5 is listed twice

E(GPa)					
Bulk Al	77	1:1	145	1:9	91
Bulk TiN	432	2.5:2.5	147	5:5	145
		5:5	145	9:1	238
		9:9	166		

I also estimated the yield strength as a marker of onset of dislocation. In Table 3.5, I calculated the yield strength of each sample. Readers should be warned that this extrapolation from the stress-strain curve involves some estimate, so these figures should not be taken as absolute. Nevertheless, two patterns can be discerned here. First, yield strength increases with increasing period for equal proportion. Considering the similar E values for all but the thickest sample, this might suggest the role of Al layer in creating absorbing stress, delaying dislocation nucleation. Second, increasing TiN portion corresponds to lower yield strength, which is aligned with earlier observation of more brittle material. This is of course surprising considering bulk TiN's ability to deform longer (as evidenced by its high yield strength) and might suggest the role of interface in regulating dislocation transmission, although evidence will need closer structure observation.

As a side, I can also measure the dependency of the yield strength to the strain rate. In general, this relation can be expressed as

$$\sigma_y = K\dot{\varepsilon}^m \tag{3.1}$$

where σ_y is the yield strength, $\dot{\varepsilon}$ the strain rate, K some constant, and m is the dependency constant. This measurement (Fig. 3.8) shows that m varies from 0.124 for 9:9 to 0.134 in 1:1 sample. This is higher than the metal multilayer (0.02) [143] but lower than those of ceramic (~ 0.5) [139,142], reflecting the nature of the multilayer structure.

Table 3.5: Yield strength of each sample in rate $R_0/4$, grouped by type, in GPa. Notice that 5:5 is listed twice

Yield Strength (GPa)					
Bulk Al	7.7	1:1	6.5	1:9	8.8
Bulk TiN	50.7	2.5:2.5	7.3	5:5	8.2
		5:5	8.2	9:1	7.8
		9:9	9.6		

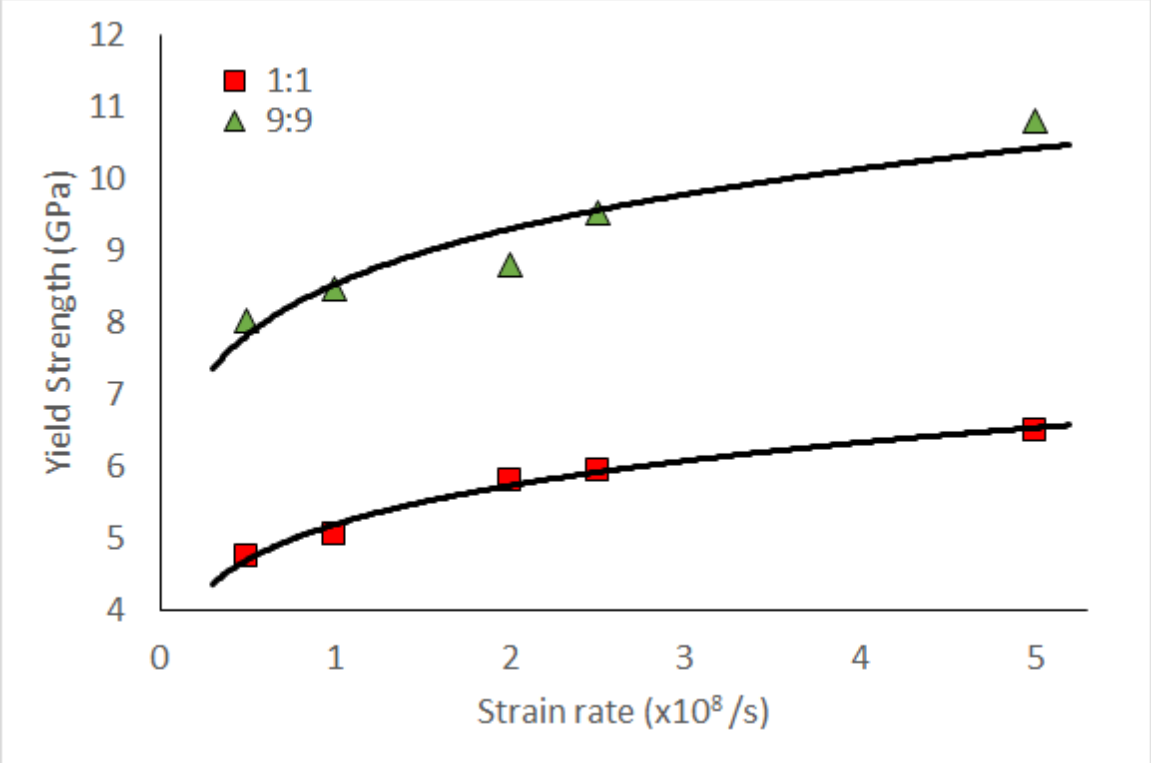

Figure 3.8: Strain rate dependence of yield strength of 1:1 and 9:9 samples

Next, I will make some observations on the serrated response of the 9:9 sample. I will start by noticing that this is not unique to this sample. For example, on Fig, 3.7(a) and 3.7(b), one can see the same phenomenon in samples 2.5:2.5, 5:5, and even, to a very faint degree, 1:9. This might suggest that an increasing Al thickness might play a role. More important, however, is the stark difference between 1:9 and 9:9 sample, which should then turn the focus to the interface and how stress is dissipated.

One might dismiss this phenomenon simply as question of relaxation time. If more time is given for the system to equilibrate, i.e. lowering the strain rate, one should see smoother response, as stress can now be readily diffused throughout the layers. As shown on Fig. 3.9, lowering strain rate actually amplify the effect, making the jaggedness more pronounced. For example, for $R_0/4$, the loading slope is 298 GPa (compare to E of 160 GPa, Table 3.4) with ~15% drop of stress at unloading. At slower $R_0/20$, the slope increased to 837 GPa with loss of ~73%. Clearly, slower rate only gives more time for the cause to 'nucleate'. On the other hand, notice that the period is virtually the same: upon doubling the strain rate, one sees exactly double the amount of oscillations during the same strain (for example compare $R_0/20$ with $R_0/10$). This might suggest a certain harmonic response in this system.

One way to get a picture on the distribution of stress is to see how well strain is distributed throughout the layer, especially on the interface. In Fig. 3.10, I compared the map of local displacement (so subtracting average cell size change due to compression) for samples 9:9, 5:5, and 1:9. Since they are coloured on the same displacement scale, it becomes clear that on 9:9 shows largely uneven strain distribution. Not only the interface sees large compression, the strain also spreads to the TiN layer. Then, one might imagine

the small load-unload cycle as mechanism where localized deformation occurs to accommodate the strain, because not enough energy has accumulated for dislocation to start. Clearly, however, this absorbing mechanism is diffusive, because no clear slip plane occurs soon after, despite the unloading of stress. However, the thickness of ceramic layer surely matters, as this behaviour is more pronounced in 9:9 rather than 5:5, even more for 1:9. If the compression is observed as it takes place, one can identify a moving wave front within the layers, signifying the harmonic behaviour observed from Fig. 3.9.

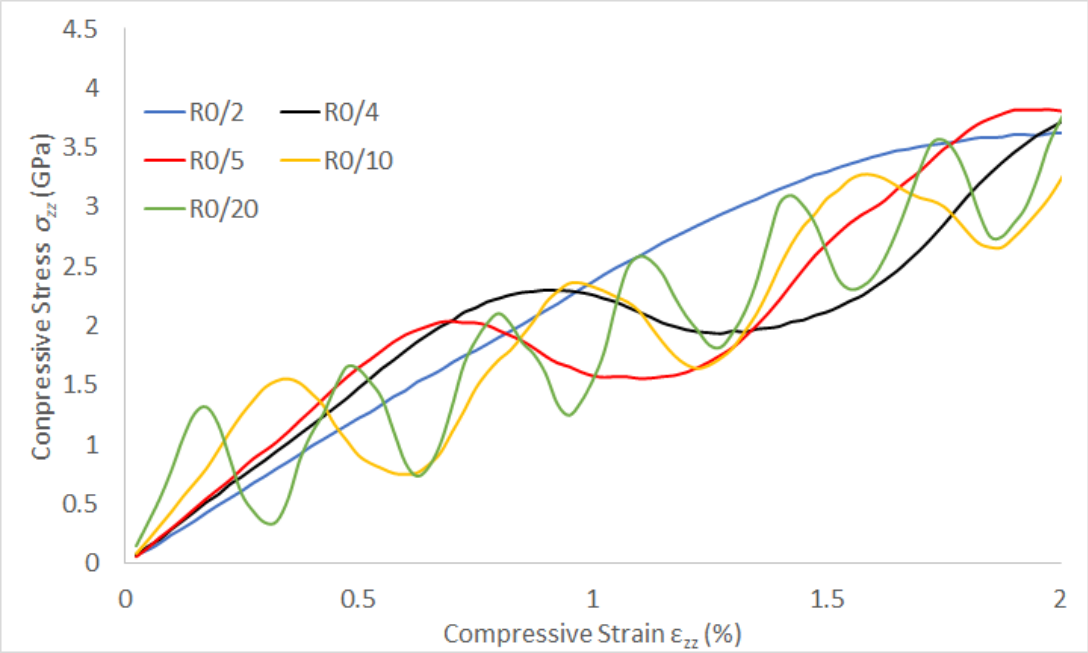

Figure 3.9: Stress-strain graph 9:9 sample at different strain rates.

Then, the magnitude drop during unloading can be understood as reflection of energy stored by the ceramic layer (with its large elasticity), which is larger than Al for the same strain and volume level. Because the strain is deeper into (and more gradually distributed) on TiN layer, thickening of TiN layer implies larger possible container for stress. Softer Al and strong interface might then accommodate this stress, allowing for release as shown on unloading drop. The drop however becomes larger for thicker TiN layer, as stress from TiN becomes more significant, both proportionally and in absolute

terms. This also explains the more extreme loading-unloading cycles seen in slower rate, because then there should be enough time for TiN to 'equilibrate' and release its stress before being compressed further. On the other hand, this whole behaviour is supressed when the ceramic layer is sufficiently thin, because compression strain on TiN is limited by the adjacent interface and hence the faithfully elastic response shown by the straight lines on the stress-strain graph. The relaxation takes place in form of compression waves, signifying the harmonic behaviour of the multilayer.

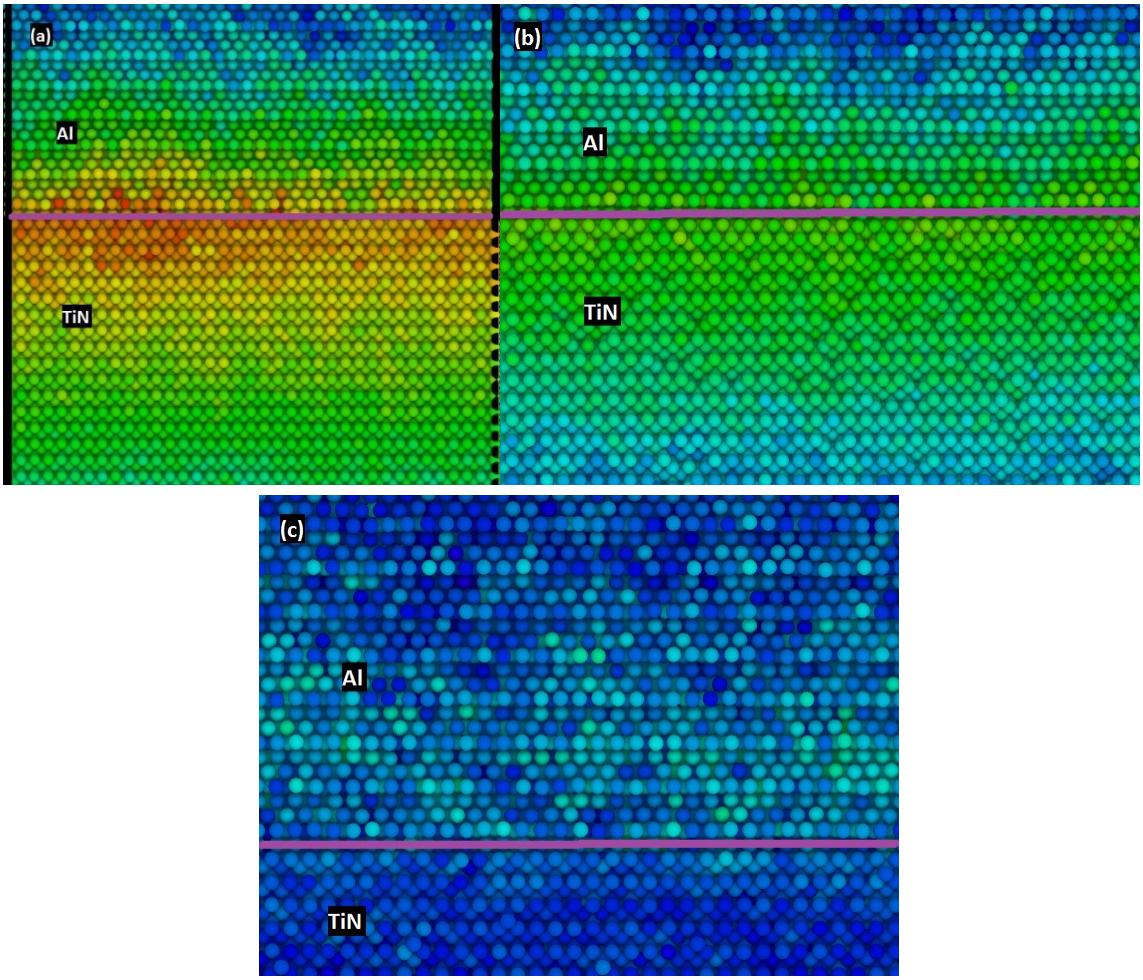

Figure 3.10: Map of local *z*-displacement magnitude at 4% strain of (a) 9:9 (b) 5:5 (c) 1:9. Interface boundary marked with purple line. Blue is the lowest, then green, yellow, and red being the highest. Coloured at the same displacement scale, but length varies.

Our first observation is that any dislocation always starts from the interface, regardless of the system and strain rate. For example, in Fig. 3.11 I show spreading process of dislocation from bottom interface to the top. Of course, this has been predicted by the CLS model [72] and observed in experiment [69]. This comes from the fact that the stress from elastic absorption is deposited on the interface. Thus, once sufficient stress accumulates, shear will be activated and slip planes will form on the metal layer. In other words, deposited stress on the interface is the driver for dislocation.

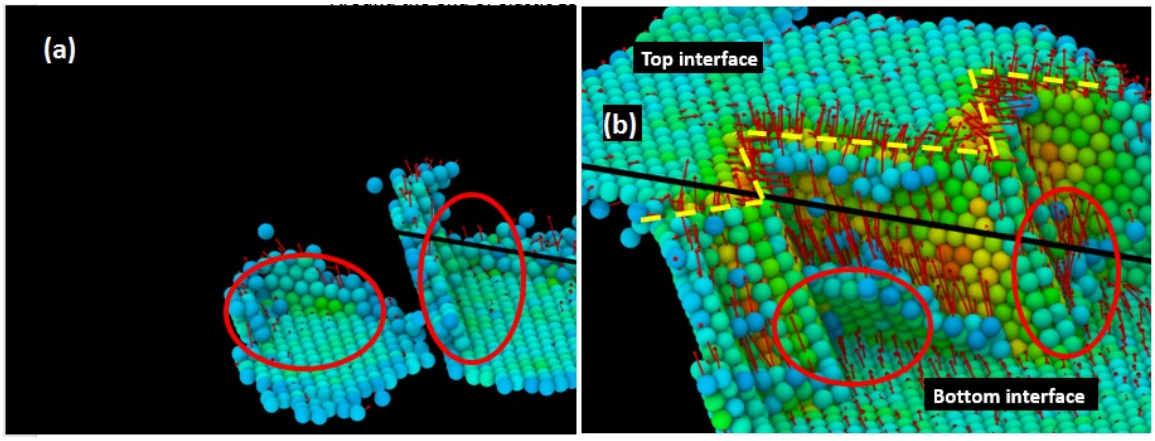

Figure 3.11: Start of dislocation at interface (a), which soon afterwards grow until hitting the top interface (b) on 1:1 sample with rate $R_0/4$. Coloured for local shear strain with other atoms removed for clarity. Blue lowest strain, red highest. Red circles added for comparison.

Once dislocation starts, however, it might not continue indefinitely. For one, two slip planes might meet, thus impending or changing direction of their growth (see Fig. 3.12). This is common in thicker Al layers, resulting in a complex interlocking pattern of dislocation planes, while multiple dislocation growth is supressed in the thinner Al layer, giving a characteristic 'zig-zagging' pattern of dislocations. At the same time, shear on the interface tends to be less pronounced, as the stress has been absorbed by the Al layer through formation of dislocations. On the other hand, when Al layer is thinner, it is more likely for single dislocation planes to connect both interfaces. As a result, shear stress

tends to be relatively high for the system and dislocation glide along the interface is often observed.

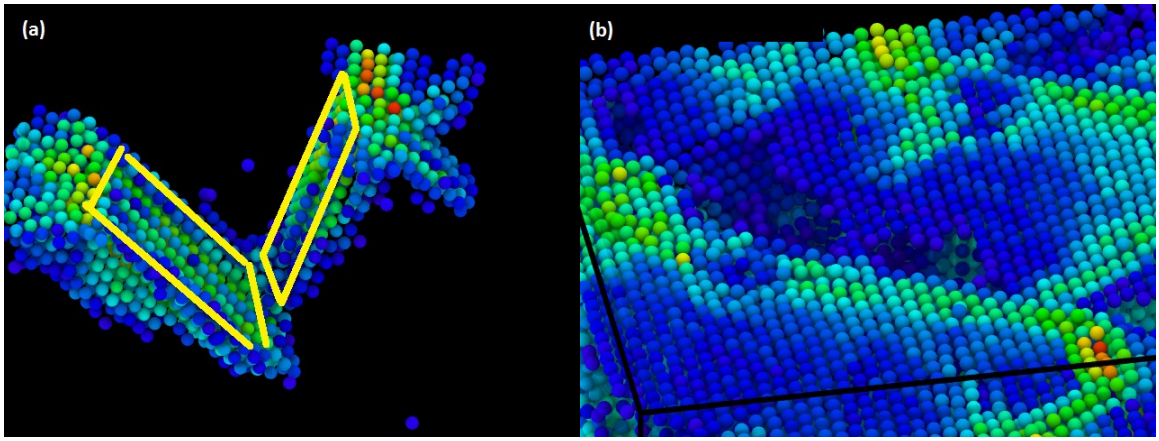

Figure 3.12: (a) Two Al dislocation planes meet, marked by yellow lines. Direction of one will be subsumed by the other. (b) Same location a moment later. Note the low shear on the interface. 1:9 sample with rate $R_0/4$ coloured by local shear strain, blue lowest to red highest.

In either case, the formation of dislocation planes acts stress relieving mechanism. However, notice that these two mechanisms are not equivalent. In the thicker Al case, the layer acts as 'stress reservoir', absorbing interfacial stress by creating slip planes. This explains the large drop of stress after yielding in both 1:9 and 9:9 samples (see Fig. 3.7), something that is not explained by any previous observations on serrated structure. For thin Al case, the reservoir is simply insufficient for this purpose, thus it is forced to form stress parallel to the interface. However, the shear strength of Al-N interface, reaches up to 26.4 GPa [127]. When combined with the uneven distribution of strain in 9:1 TiN, this might explain the early yield observed in 9:1 sample (see Fig. 3.7(b)).

Once sufficient number of dislocations accumulate, then the stress unloading will end and the 'second elastic' zone will start. The phenomenon is worth more detailed explanation, which will be given here. In the thick Al case, it is quite clear that the stress reservoir mechanism will stabilize when the dislocation planes either reach both

interfaces or they are interlocked that further slip without stress is not possible. For the other case, recall that most dislocations are singles that reach both planes. These single dislocations, such as shown in Fig. 3.13(a), would serve as pin on the interface: observe that the displacement vectors (red arrows) either are neutralized or show rotation around the dislocation (black circles), instead of uniform shear on are without dislocation (red circles). When one observes the whole interface (Fig. 3.13(b)), these deposited dislocations would form boundary of an 'island' (this island is marked by red dotted lines in Fig. 3.13(b) and (c), some atoms removed because of lower strain). Finally, when enough dislocations are formed, they pin the stable islands and thus ending the transition, as no more interface shear can be exploited. Similar mechanism also exists in the thick Al case, although more complex dislocation planes make it harder to observe in my model.

To summarize, I found that the elasticity of bilayers depends mostly on the proportion of ceramic, although the bilayer period also plays a role. Stability, however, is controlled by the thickness of the ceramic layer. For all but the thinnest layer, the increased and uneven compression in TiN layer emanates from the interface. This created a short loading-unloading cycle without formation of dislocation. How does the residual stress at the interface contribute to yielding is not quite clear. On the other hand, Al acts as 'stress reservoir' due to its ability to plastically deform. This means bilayers with thicker Al will be able to unload accumulated stress by creating dislocation planes. which will continue until sufficient density is reached. For thinner Al layers, because dislocations are mostly singular, shear on interface is preferable, although stress is not relieved. On the other hand, the deposited dislocations on interfaces will pin the interface

until no further shear is possible. In either case, further compression will then leave the transition zone into the 'elastic' plastic zone discussed in the next section.

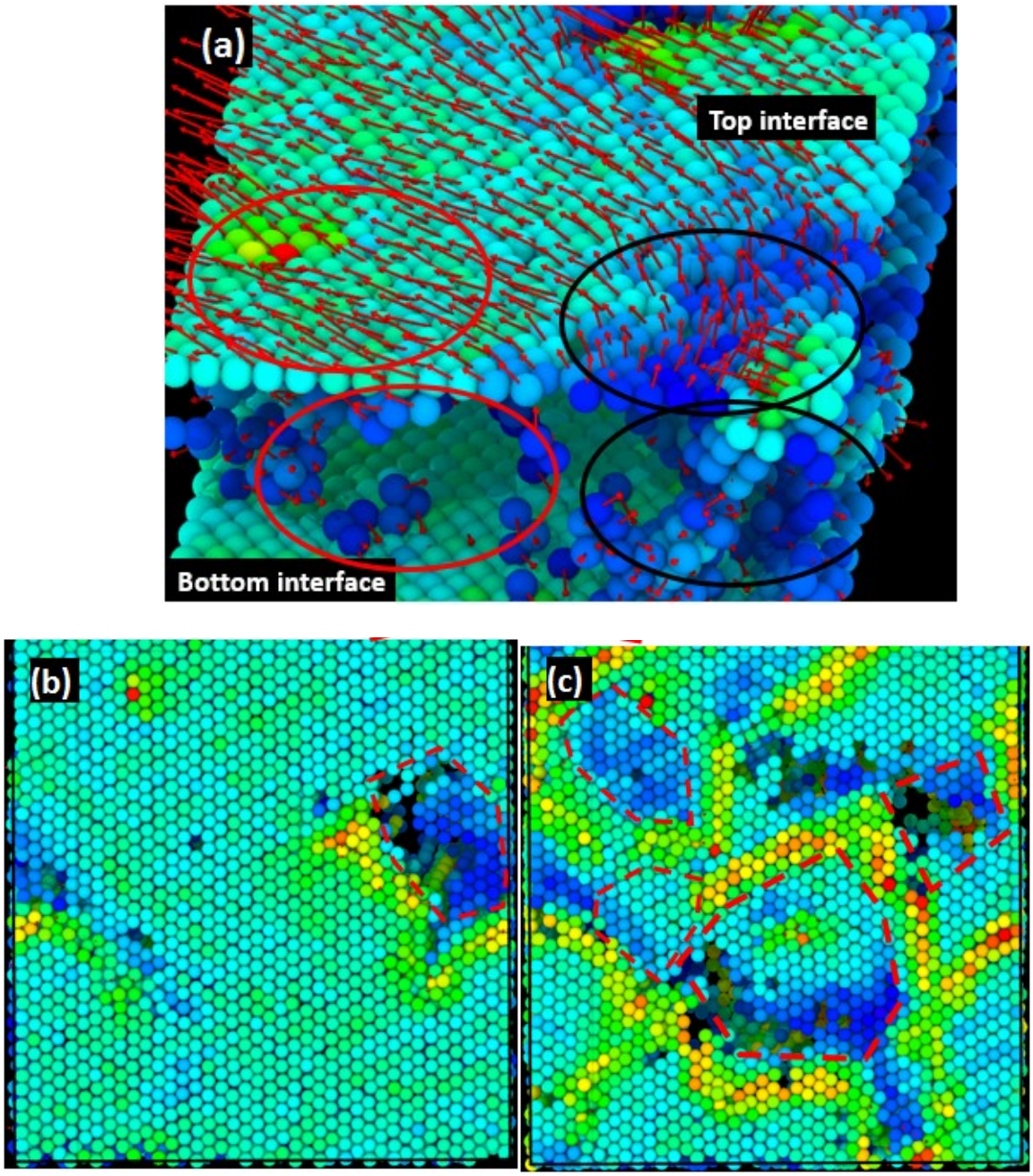

Figure 3.13: (a) Comparison between interface area of those with and without dislocation. (b) Top view of interface, island (red dotted line) marks area without dislocation marked by red circle in (a). Notice the area of high strain (yellow) by the island where dislocation meets interface. (c) At the end of transition zone, dislocations have pinned islands on the interface. Sample 9:1 at rate $R_0/4$. Coloured for local shear strain, blue lowest to red highest.

'Elastic' Plastic Regime.

In this section, I will discuss what will be called the 'second elastic' zone: where significant strain hardening necessitates almost linear increase of stress for further compression. In many ways, the present mechanisms are not dissimilar to those under elastic regime, except now significant hardening has taken place on metal layer, because the dislocations along what is identified as [111] planes in metal have taken hold. I will focus here on two phenomena: dislocation glide and confluence of dislocations as precipice for failure.

Dislocation glide can be seen as a response to plastic incompatibility of both layers: when the resolved shear stress in either layer is greater than certain critical value, glide is a mechanism to reduce this stress and allow plastic deformation [72]. The glide front can be marked with what is termed the Orowan bow in metal layer, which connects dislocations on both interfaces. Both of these two marks are observed in the sample. In Fig. 3.14, the dislocation bow can be seen by orange displacement vector (calculated as difference with the initial state, subtracting homogeneous movement. See Appendix B for detail). For an example of ceramic glide, on Fig. 3.15 the evolution of shear stress on 1:1 sample can be seen with local movement shown by orange displacement vector (calculated as difference with the initial state, subtracting homogeneous movement). Notice than how dislocation accumulation, which corresponds to the confluence of metal dislocations, at top TiN interface on Fig. 3.15 (a) (light blue) dissipates as the local dislocation moves in (c). However, the glide creates a feedback response, prompting movement of dislocation in Al (c), which in turn prompts stress applied to the interface. In fact, I have just described what in CLS construct is termed as interaction stress τ_{int}

[72]. That is, the stress due to interaction between accumulated interface dislocations will control whether glide (so slip parallel to interface) can occur.

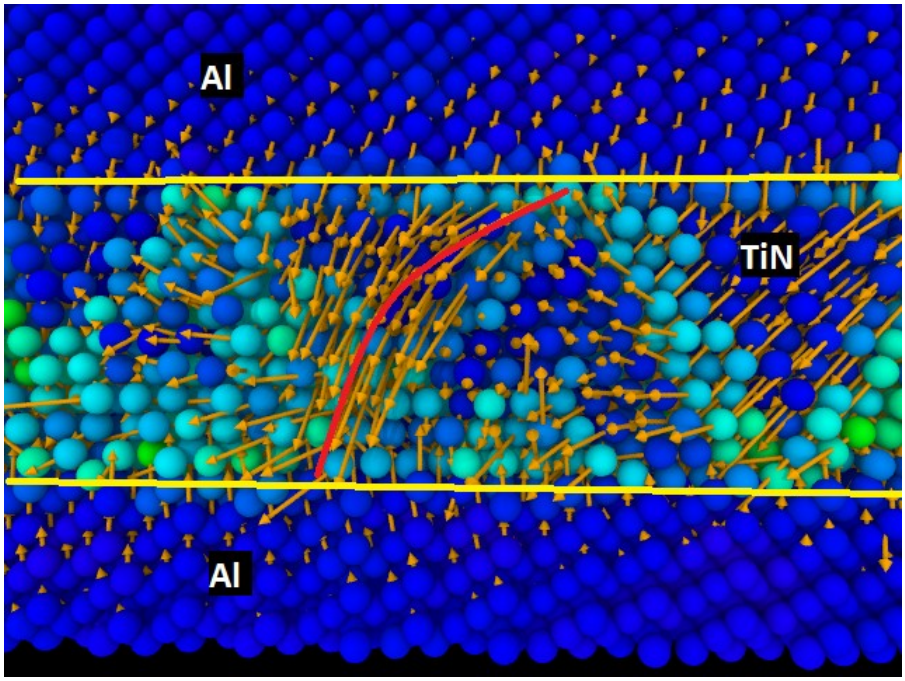

Figure 3.14: Orowan bow observed in (110) plane of 1:1 sample, marked by red line.

I should stress that this feedback between the accumulated dislocations on metal interface with glide on TiN is important in the plastic co-deformation. If there is not enough accumulated dislocation on metal interface. When such occurrence is rare, dislocations are located few and far between in the ceramic layer. In turn, this reduces the *local* shear stress in ceramic (but not average, which holds more or less constant), which then prevents glide to take place. For example, in Fig. 3.16, observe that instead of metal dislocation loop as in Fig. 3.14, the accumulation, which is composed of multiple slip planes instead of one, uniformly applies stress to the interface. Unsurprisingly, because stress is then concentrated on the ceramic layer without relief, failure will occur earlier.

Figure 3.15: From (a) to (d), gliding of dislocation, shown by local displacement vector from original position (orange arrow) on both layers of 1:1 sample coloured by local shear strain, blue lowest, green highest. Notice the deposited stress at the top of TiN interface.

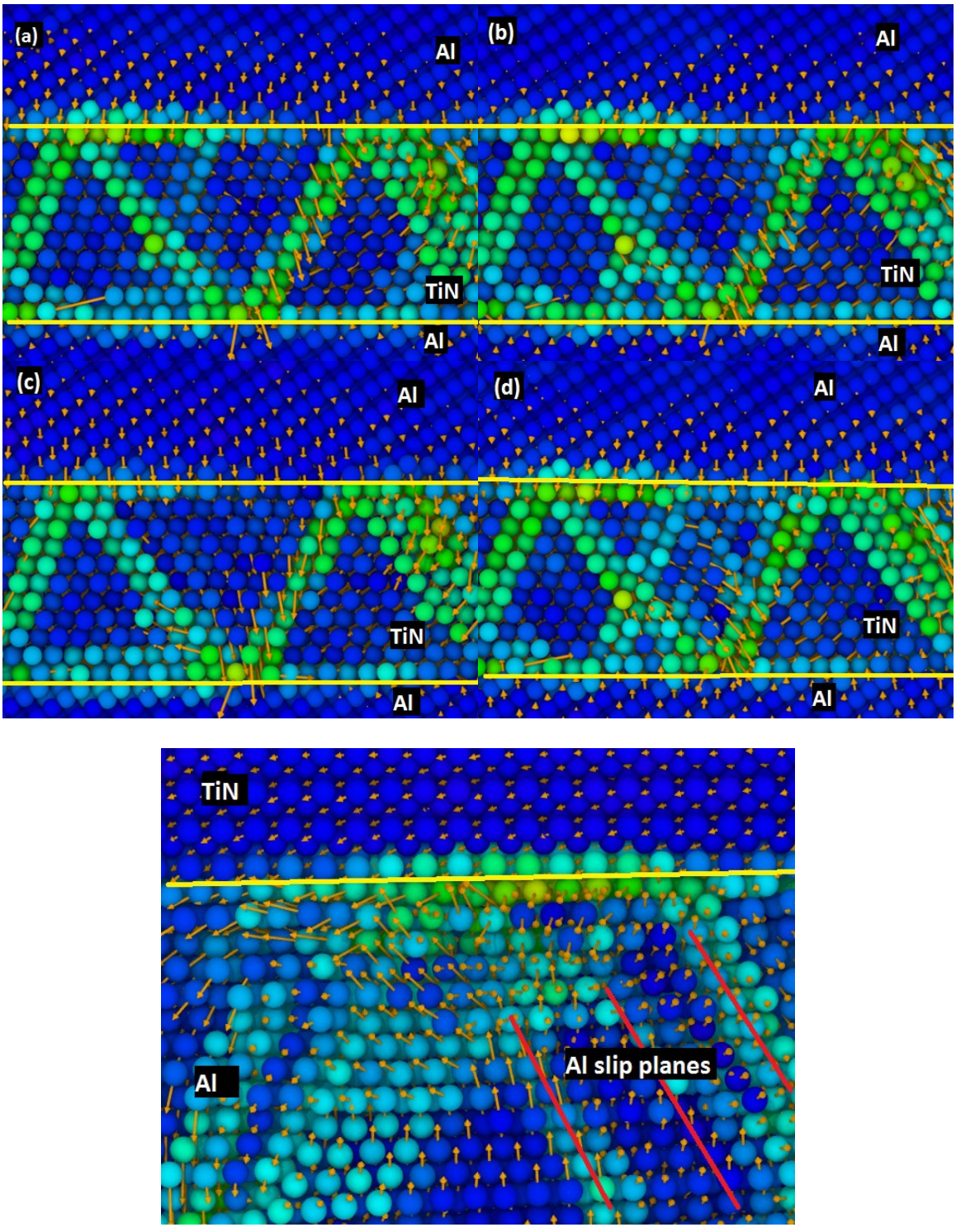

Figure 3.16: Even though the interface of 1:9 sample sees higher local shear at comparable strain, lack of 'triangular network' of metal slip planes make glide harder. Instead, whole layer shear is favoured. Sample 1:9 on rate $R_0/4$, coloured by local shear strain.

On the other end of the spectrum, as can be seen in Fig. 3.17, that instead of shear, the ceramic layer underwent tensile. The reasoning behind is ultimately very similar: higher ceramic ratio reduces local shear stress, preventing glide to start and failure to happen earlier.

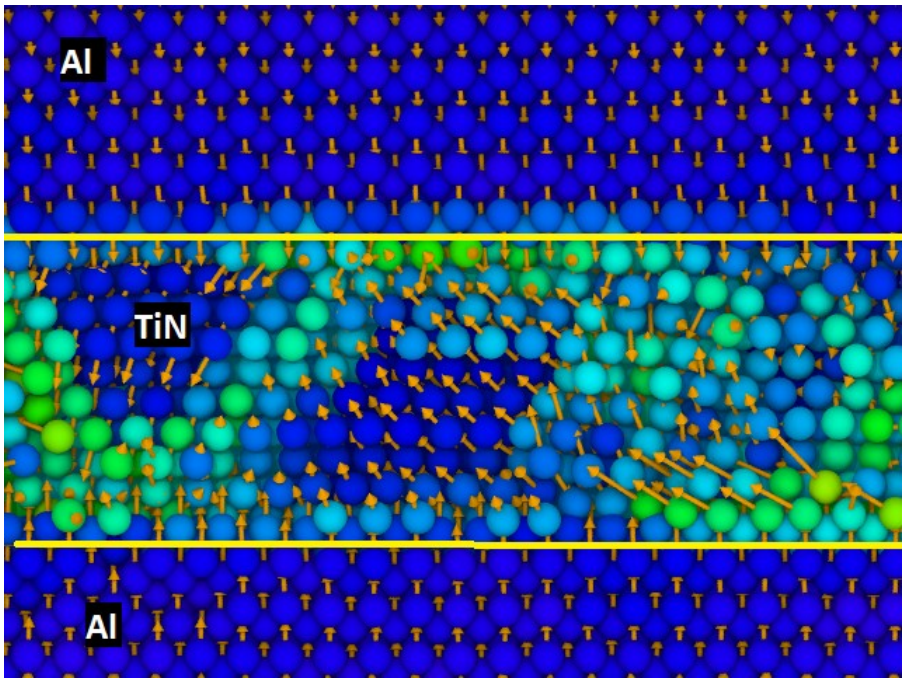

Figure 3.17: Even though the metal interface of 9:1 sees local shear, none is seen on the ceramic side. Moreover, instead of glide, tensile on ceramic layer is observed.

While discussing dislocations, it will also be appropriate to discuss anomaly on 1:1 sample. If one observes Fig. 3.6(b) more carefully, they will notice 1:1 sample shows another dip in stress during the 'elastic' plastic zone around 12 GPa stress ($\sim$ 11% strain). Afterwards, the sample seems to deform 'elastically' with linear increase in stress. Naturally, a major stress-reducing mechanism can be expected. The difference is, of course, that metal layer has mostly been saturated. Thus, there is only one possible solution without cracking: start of deformation, or slip, in TiN layer. On Fig. 3.18 I compare the ceramic interface right before imposed on the interface right after the drop.

One thing to notice is the major shift in TiN layer, not only by area (as shown) but also by number of atoms involved over a short period. This shift is larger than movements before or after it. It might then be surmised that this momentary slip is responsible for relieving stress in the ceramic layer. Later deviation from linear trend (around 18 GPa, ~ 16% strain) marked the saturation of this mechanism.

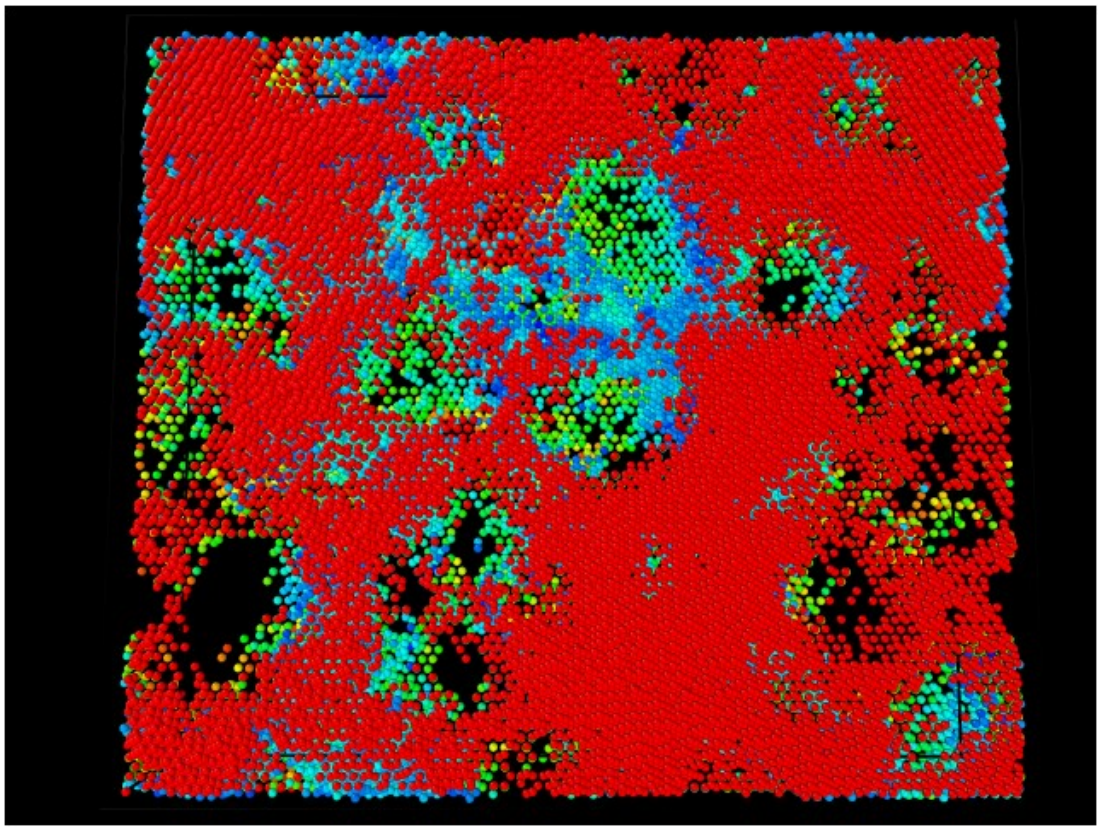

Figure 3.18: Comparison of top TiN interface before (solid red) and right after drop in stress (colourful green-blue). Strain rate $R_0/4$ and coloured by displacement magnitude.

So far, the discussion on plastic deformation has ended in occurrence of crack. However, I have not made any observation on circumstances leading to such uneventful occasion. In a very general sense two events, not always in conjunction, can be identified that leads to crack: high stress at dislocation accumulation and interface buckling or delamination. I did not observe discernible delamination in any of these samples and

none is identified in any of the experiments. Nevertheless, I will lay down the characteristics of events leading to crack here.

Interface failure is quite straightforward. The interface acts as a dislocation barrier, so that slip is contained within the metal layer. When the interfacial stress becomes sufficiently high, this barrier will fail and hence crack will occur. It then follows that all crack should stem from the interface, which I will call the breakthrough mode. Surely this is not quite so surprising, since all dislocations are considered to nucleate from the interface. In Fig. 3.19, I show a representative example of such mechanism. It starts with slip planes forming in TiN. This formation lowers the shear strength of the ceramic, allowing the deposited stress at the accumulation to break through the interface.

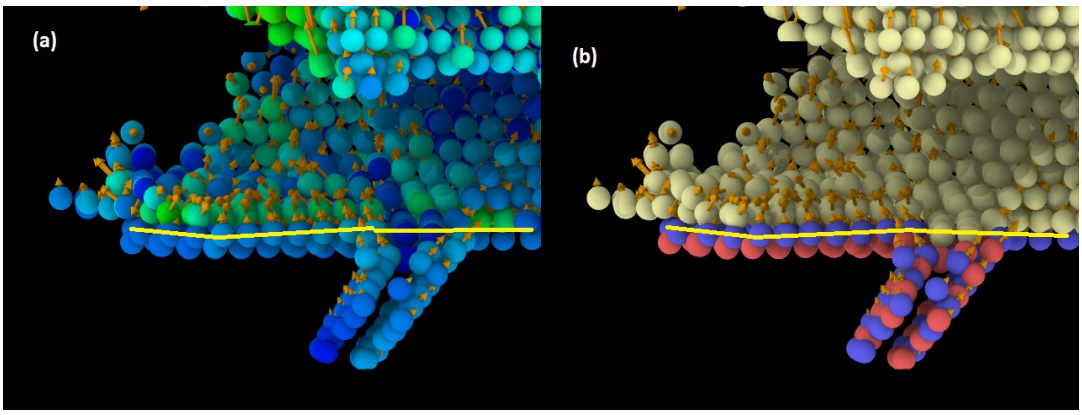

Figure 3.19: Breakthrough crack in 1:9 sample at rate $R_0/5$. (a) is coloured with shear strain to identify slip planes. (b) is coloured by atom type, displacement vectors added. Both taken at same time and angle. Original interface marked by yellow line. Red and blue are Ti and N, respectively, while white is Al.

To conclude, it is clear that many of the phenomena of the elastic zone are also observed here, such as the jagged texture of stress-strain on samples with thick ceramic layer. An important mechanism in plastic co-deformation is established [72]. It relies on the metal dislocations to accumulate at the interface, increasing the deposited stress, while allowing ceramic to continue deforming elastically, which give the almost 'linear'

shape of stress-strain. Interface's shear strength will prevent dislocation transmission at the cost increasing interaction stress τ_{int} in ceramic layer. If the metal dislocations are sufficiently dense and the ceramic layer sufficiently thin, higher localized resolved shear stress will allow glide of dislocation along the interface in ceramic, allowing plastic co-deformation of ceramic and metal. Failing either, as shown in 1:9 and 9:1 samples, the ceramic will deform elastically, which explains the almost linear response of most samples in this zone, until, due to ceramic's brittleness, crack appears. Because the stress-relieving mechanism of the glide does not take place, crack failure will occur earlier. I also observe the events leading to occurrence of crack. It starts as slip begins to occur in ceramic layer, which weaken the interface. The accumulated stress on metal interface then can overcome the barrier and hence creating crack. I should insist, however, that this process is statistical and the mere presence of accumulation does not necessarily lead to crack (see Fig. 3.20).

Eventual Failure.

Recall the claim made in the previous section that the formation of dislocation on the ceramic layers is soon followed by breakthrough crack by the metal layer, practically extending the dislocation planes. Of course, I have ignored here the 1:1 case which satisfies both the criterion of plastic co-deformation [72]. However, what is then the crack mechanism in 1:1 sample and how can it be reconciled with the continued plastic deformation observed in experiment [55,69]. It is natural to suspect that circumstances of crack growth differ on each sample. In general, what is the effect of period and ratio in determining the failure mechanism? I will try to make observations to answer these questions here.

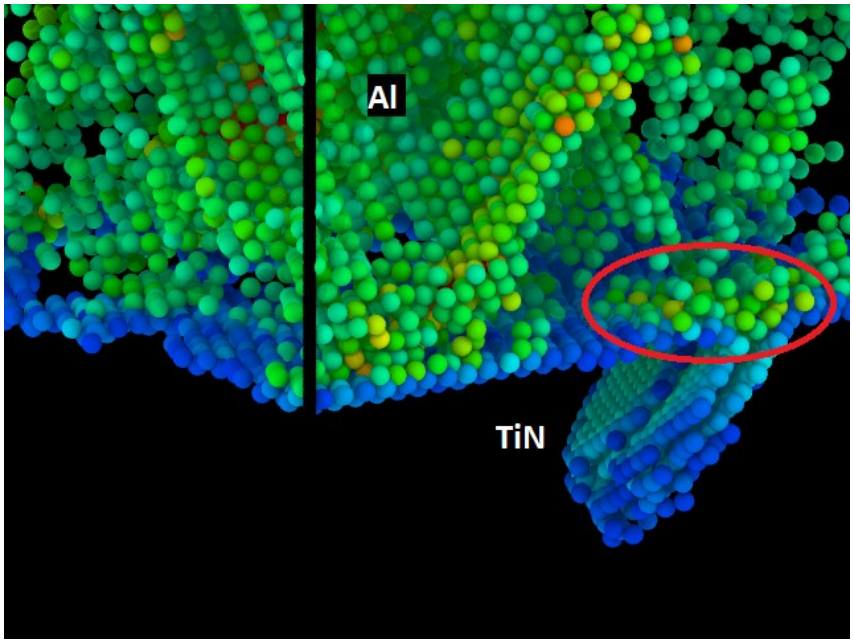

Figure 3.20: Confluence of dislocations might not necessarily lead to crack, which happen instead at relatively weak stress (red circle). Sample 9:9 at rate $R_0/4$ coloured with shear strain.

I will identify three cases of crack: Al-9 type, 9:1 type, and 1:1 type. Their difference mainly lies in how the ceramic deforms and forms slip planes. In Al-9 samples, seen not only on 1:9 (Fig. 3.19) and 9:9 sample (Fig. 3.20), but also those with significant Al thickness such as 5:5, relatively small level of stress is needed to break through the interface, while the slip plane forming in Al is already too great, giving the crack an impression as continuation of those planes. In turn, the ceramic slip planes tend to be few and localized and the crack has the shape of metal protrusion to the ceramic layer.

The other two cases are signified by the small Al volume. Recall that Al acts as the absorber of stress through its dislocation planes. Then, the thinner Al layers will promote higher stress in TiN layer, making the crack, once it happened, a non-localized phenomenon. For example, in 9:1 sample (Fig. 3.21(a)), I can identify multiple parallel slip planes on TiN layer. In fact, compared to the Al-9 samples, TiN layer on the 9:1

sample seems to slip in unison. In some ways, this is not so surprising, considering the large compression identified to emanate from the interface deep into TiN layer (Fig, 3.10). The higher local compression on interface then makes the whole layer susceptible to crack, as one slip will be followed by another. This might justify the earlier crack in this sample. A different idea apparently applies uniquely to 1:1 sample. Instead of uniform slips forming in the ceramic layer, one can see that the piling to the deformation planes. I find the impression that instead of naturally occurring slip where Al would flow in, the crack is initiated by Al 'piercing' through the interface and hence the piles occur as the atoms are forced to protrude to 'the sides'. While such interpretation is indeed interesting, I find no further evidence for it. The thick piling seems to be more a reflection of a high stress of the ceramic layer interfacing with a significant plastic deformation of the adjacent Al layer, where simple slip movements, such as those that initiated easier slip in Al-9 cases, are not possible in the ceramic layer. Because of the high interfacial accumulated stress, even after atoms with lower stress are removed, I am left with such impression.

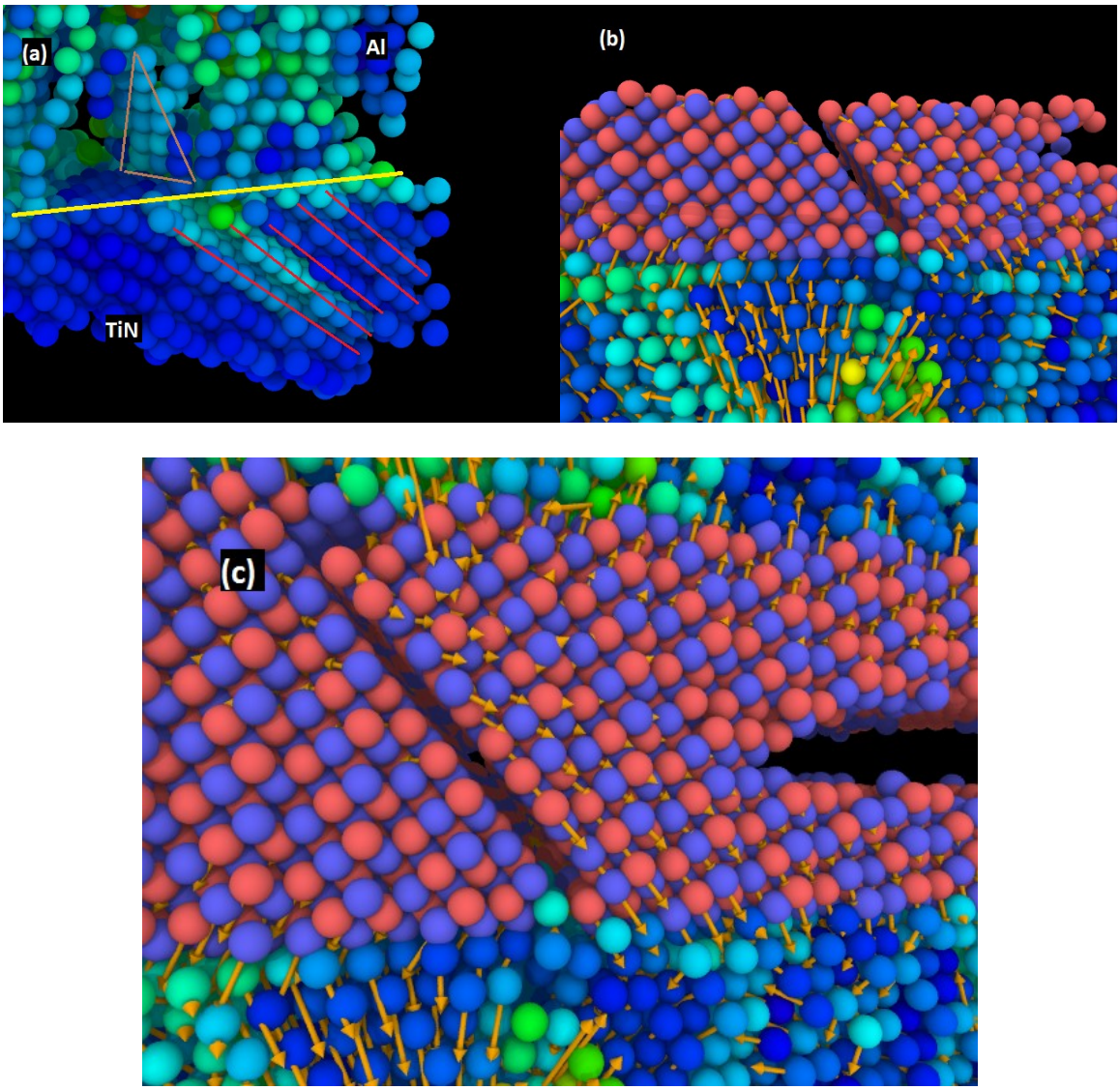

Figure 3.21: (a) Crack in 9:1 sample, coloured by local shear strain. TiN slip planes marked red, Al slip plane marked with brown. (b) and (c): Crack in 1:1 sample. Red and blue are Ti and N, respectively. On the bottom is Al, coloured by local shear strain. Not on the same scale with (a). Atoms removed for clarity.

DISCUSSION AND CONCLUSION

In this chapter, I will summarize the main findings of this study. I will review the effectiveness of my chosen computation method in creating an effective MD potential. I have also compared findings in this study with both theoretical model, experiment, and CMD simulations on comparable systems. Last, I will gleam into possible ways to create a stronger multilayer.

Effectiveness of Potential Development Method

I started this study as a project on developing an effective MD potential. The general method that I used, from the AIMD sampling of atomic forces and energies to the force-fitting process using the Potfit code, is well-established and has been successfully applied to various systems [105]. The model that is chosen, from the EAM-based potential [94], and the chosen particular functions [109] have also been applied successfully to systems containing various metals, ceramics, and those with low symmetry systems [93]. In short, it is reasonable to expect this chosen method to perform reasonably well. One difference is, of course, the presence of the nitride phase in my system, which behaves very differently than those of metal, especially with regards to the directionality of its covalent bonding, thus the inclusion of such materials has presented quite a challenge to my methodology.

My evaluation of the potential functions' forms found some significant differences from the expected results. For one, at least two (Ti-Ti and N-N) pair potentials show finite barriers to an arbitrary separation. Moreover, Ti-N function shows the first equilibrium position to be unphysically small. Nevertheless, all those pairs

involving metals either show at least one correct position (such as shown on the inset of 3.3(c)) or follow the expected behaviour (no stable position for Ti-Al) with a reasonable degree of comparison to the experimental observations.

The applications of resulting optimized potential to calculate some of the structural parameters of Al and TiN yielded mixed somewhat of a mixed result. In one hand, the potential is quite successful in reproducing the unit cell dimensions of Al and TiN with a discrepancy of less than 1.5%. On the other hand, I had only a moderate success in computing the elastic characteristics of the chosen samples. While the result for TiN is in line with other calculations [65,126], the discrepancy is more significant for Al (Table 3.2). Even more challenging is the results of the computation of cohesive and vacancy formation energies, which show a very large discrepancy with other studies (Table 3.3). In fairness, I had not exclusively included the AIMD samplings that would include the vacancy additions as part of the configurations. Nevertheless, the application of the potential to simulate the deformation behaviour has been quite successful. I have reproduced the findings of various DFT calculations [62,63,70] that the strongest bond is formed by [111] plane on both sides of the interface with N as the terminating layer for the ceramic surface. Moreover, I can observe the effect of the addition of *hcp* Al as it improves the sensitivity of the optimized potential to change of Al structure during deformation to nucleate dislocation and slip planes.

Al-TiN Deformation: Perspective from Previous Studies

In this study, I have looked at three different factors affecting deformation behaviour: strain rate, bilayer period, and layers' volume ratio. To summarize, I find that the strain rate smoothens the dislocations: a higher strain rate delays the nucleation and

propagation of dislocations, as the relaxation time of each is longer than the time needed to exert a higher strain to the sample. In turn, this delays the occurrence of dislocations and eventual crack. The bilayer period, however, does not significantly affect the stress-strain graph, although a longer period seems to delay the yield point due to its larger stress reservoir in Al. At the same time, thicker samples show the short-term loading-unloading pattern as shown by the serrated texture of the stress-stain graph (Fig. 3.7(a)), which is amplified at the lower rate (Fig. 3.9). Instead of a question of relaxation time, which is independent of strain rates, I find that thicker TiN layer corresponds to a larger-than-average compression on ceramic closer to the interface. Thus, the drop in unloading phase corresponds to the amount of energy that can be stored in TiN layer, which corresponds to its thickness. This compressive cycle is then represented by the moving wavefront of the compression, signifying the underlying harmonicity of the sample. Last of the three, I observe that the volume ratio affects the brittleness of the material, with the sample tending towards properties of the dominant component.

I have affirmed the importance of the interface in the multilayers. First, I have shown that interface is the source of both dislocation and crack nucleation. As shown in Fig. 3.11, as the stress reaches certain level (at least comparable to yield of bulk Al), the shear is activated on the interface allowing the dislocations to occur in the metal layer. Similarly, cracks are initiated when the resolved shear stress on the ceramic layer reaches a critical point so that a slip is made possible. The interface barrier then will be lowered, allowing deposited metal dislocations on the interface to break through and create crack. Notice, however, that no crack has been found in the Al layer, although subgrain has been found to form during compression. Second, interface has been found to act as a barrier to

dislocation: extension of slip planes is limited by the shear strength of the interface (estimated to be 26 GPa [70]), confining them to the metal layer. When multiple dislocations can form, as in the thicker Al layer, one observes the interlocking network of dislocations, acting effectively as the sink for the generated stress. Hence the low level of stress observed in 1:9 layer. If the Al layer becomes sufficiently thin, however, only one dislocation can form. In the end, presence of interface barrier forces even the 1:9 case into this regime, albeit with lower stress. Last, I also find that interface acts as sink of stress: as soon as slip is about to begin in ceramic layer, the high critical resolved shear stress only prevents the plane shearing, absorbing instead the stress. High level of accumulation will then accumulate, allowing slip that allows crack to form.

In a large part, my result agrees with the confined layer slip (CLS) mechanism [72,144,145]. Most importantly, I have been able to identify the Orowan bowing and the ceramic glide as the stress-relieving mechanisms during the plastic deformation. However, some issues should be noted. For one, the findings are not consistent with the prediction of a lower yield strength at a higher period [146]. I would propose to explain this by a higher stress absorption in TiN, which can undergo a further compression than that observed in the thinner samples.

Second, the bilayer's interface, by design, eliminates a significant lattice mismatch, even after the thermal equilibration. Moreover, the pattern of continued slip planes across interface makes the observed system to be for the most part coherent. It would be fair to ponder the consequence of an opposite case. In [144], it was found that coherency stress is the major component of interface's strength. Moreover, according to their calculation, this phenomenon should persist until the misfit strain becomes

significant at ~ 7%. Surely this is lower than the Al/TiN misfit of ~ 4.5 %. On the other hand, it may have an impact on the dislocation nucleation. It was investigated in [147] that even for slip planes with an equal Schmid factor, the slip planes that are incoherent with the neighbouring planes' array is preferred. Moreover, they found that the nucleation preference lies, more importantly, at the interface which has a lower local surface energy. While the observed system contains mostly isotropic interface, a significant misfit might then favour an earlier onset of dislocations and cracks.

Most important is my last contention. It was claimed that the dislocation deposition on the ceramic interface is a response to the plastic-elastic incompatibility, with the metal layer already underwent a significant hardening while the ceramic layer was still in the elastic mode. The residual stress from the dislocations, it was thought, then applies parallel to the interface, causing the effective tensile stress to the ceramic and the compression to the metal layers with an average of zero. In this way, the strain hardening occurs in Al layer while the increased tensile raises both the resolved shear stress on the interface and the opportunity of crack or slip formations for the ceramic layer [72]. In this study however, I have not found this explanation to be sufficient enough to explain the second stress drop in the stress-strain curve (e.g. Fig. 3.6(b)) in 1:1 sample). For instance, if it is sufficient to fault the plastic deformation, why is it still possible to deform as if there is no change in the strain hardening rate afterwards? Indeed I observe a significant increase of the deposited dislocation, but the ceramic seems to still deform as if it was in the elastic mode. Although I have investigated for plausible triggering mechanisms, none has been fully identified. One explanation, such as that proposed in [144], involves a 'slip trap' contained by a relatively coherent interface such

as ours: after a certain small slip, there is point where the shear stress drops, inhibiting further sliding. I have yet to find an evidence for this mechanism.

Creating a Stronger Nanolayered Composites

If there is one thing to be taken from this study, it is to help find an ideal multilayer: one that combines hardness of ceramic with significant ductility of metal. In [72], it was predicted that an ideal ductile multilayer would maximize the interaction stress τ_{int} between adjacent multilayers. This would involve minimizing two factors: 1) the separation between dislocation accumulations on the metal side and 2) the thickness of ceramic layer. I will make comparison between different samples, finding one that would satisfy both criterions.

Clearly, this automatically eliminates those with thick ceramic layers, such as 9:1. Not only it fails the thickness criterion, the high compression of ceramic near the interface also might allow a structural instability, which is unresolved only because of the lack of stress reservoir in metal layer. For the same reason, however, I must also eliminate the 9:9 and 5:5 samples. The loading-unloading cycles create an inherent instability, which might be significant for less-than-ideal operating conditions such as those in high temperatures and those that undergo cyclic thermal expansions. I am then left with either 1:1, 2.5:2.5, or 1:9 samples. Among these, clearly 1:9 sample would fail the accumulation density criterion: a thicker Al layer allows multiple dislocations to create the dislocation pile-ups and a complex network of slip planes within the layer. However, this means that accumulations would be less likely to occur, because each accumulation is already the confluence of multiple slips. With two choices left, I can then

simply apply the minimizing principle to choose 1:1 sample as the ideal multilayer. This agrees with prediction in [72].

REFERENCES

[1]. D. Chance and D. Wilcox 1971 *Proc. IEEE* **59**, 1455

[2]. S. J. Lloyd and J. M. Molina-Aldareguia 2003 *Phil. Trans. Royal Soc. A: Math., Phys., Eng.* **361**, 2931

[3]. R. Hampy 1975 *IEEE Trans. on Parts, Hybrids, and Packaging* **11**, 263

[4]. M. Gauvin, E. E. Fullerton, and F. E. Talke 2010 *J. Appl. Phys.* **108**, 063925

[5]. A. Espinosa, M. Garcia-Hernandez, N. Menendez, C. Prieto, and A. de Andres 2010 *Phys. Rev. B* **81**, 6

[6]. K. Kubota and M. Naoe 1991 *J. Appl. Phys.* **70**, 6430

[7]. S. Lin, F. Ye, J. Ma, J. Ding, C. Yang, and S. Dong 2016 *Materials & Design* **97**, 51

[8]. Y. Liu, J. Zhang, S. Jiang, Q. Liu, X. Li, and G. Yu 2016 *J. Magn. Magn. Mater.* **420**, 70

[9]. Y. Lisovskii, E. Knizhnik, V. Stolyarov, and L. Fionova 1996 *Mater. Chem. and Phys.* **44**, 239

[10]. R. Malik, S. Lamba, R. K. Kotnala, and S. Annapoorni 2010 *Eur. Phys. J. B* **74**, 75

[11]. P. Jiang, X. Wu, W. Xue, J. Chen, W. Wang, and Y. Li 2017 *Ceram. Intl.* **43**, 1335

[12]. F. Jimenez-Villacorta, A. Espinosa, E. Cespedes, and C. Prieto 2011 *J. Appl. Phys.* **110**, 113909

[13]. A. Garcia-Garcia, A. Vovk, J. A. Pardo, P. Strihovanec, C. Magen, E. Snoeck, P. A. Algarabel, J. M. D. Teresa, L. Morello, and M. R. Ibarr 2009 *J. Appl. Phys.* **105**, 063909

[14]. A. Koziol-Rachwal, T. Slkezak, K. Matlak, P. Kuswik, M. Urbaniak, F. Stobiecki, L. D. Yao, S. van Dijken, and J. Korecki 2014 *Phys. Rev. B* **90**, 045428

[15]. S. Bedanta, N. Chowdhury, and W. Kleemann 2013 *Sens. Lett.* **11**, 2030

[16]. Y. Ning, W. Wang, Y. Sun, Y. Wu, H. Man, C. Wang, S. Zhao, E. Tomasella, A. Bousquet, and Y. Zhang 2017 *Infrar. Phys. & Tech.* **80**, 65

[17]. Q.-C. Zhang 2001 *J. Phys. D: Appl. Phys.* **34**, 3113

[18]. Q.-C. Zhang 2000 *Sol. Energy Mater. Sol. Cells* **62**, 63

[19]. S. Zhao and E. Wackelgaard 2006 *Sol. Energy Mater. Sol. Cells* **90**, 243

[20]. A. Sakurai, H. Tanikawa, and M. Yamada 2014 *J. Quant. Spectrosc. Radiat. Transfer* **132**, 80

[21]. C. Hu, H. Zhang, F. Li, Q. Huang, and Y. Bao 2013 *Int. J. Refract. Met. Hard Mater.* **36**, 300

[22]. S. Aryal, R. Sakidja, L. Ouyang, and W.-Y. Ching 2015 *J. Eur. Ceram. Soc.* **35**, 3219

[23]. P. Eklund, M. Beckers, U. Jansson, H. Hoegberg, and L. Hultman 2010 *Thin Solid Films* **518**, 1851

[24]. M. F. Cover, O. Warschkow, M. M. M. Bilek, and D. R. McKenzie 2009 *J. Phys.: Condens. Matter* **21**, 305403

[25]. S. Aryal, R. Sakidja, M. W. Barsoum, and W.-Y. Ching 2014 *physica status solidi (b)* **251**, 1480

[26]. S. Gupta and M. Barsoum 2011 *Wear* **271**, 1878

[27]. A. S. Ingason, M. Dahlqvist, and J. Rosen 2016 *J. Phys.: Condens. Matter* **28**, 433003

[28]. J. Wang, Y. Zhou, Z. Lin, F. Meng, and F. Li 2005 *Appl. Phys. Lett.* **86**, 101902

[29]. M. W. Barsoum and M. Radovic 2011 *Annu. Rev. Mater. Res.* **41**, 195

[30]. Q. Wang, D. He, F. Peng, L. Xiong, J. Wang, P. Wang, C. Xu, and J. Liu 2014 *Solid State Comm.* **182**, 26

[31]. K. Liu, X.-L. Zhou, H.-H. Chen, and L.-Y. Lu 2012 *Physica B* **407**, 3617

[32]. J. O. Kim, J. D. Achenbach, P. B. Mirkarimi, M. Shinn, and S. A. Barnett 1992 *J. Appl. Phys.* **72**, 1805

[33]. B. Zhu, Y.-H. Li, J. Zhu, Y.-J. Hao, G. Xiang, B.-R. Yu, and W. Li 2014 *Comp. Mat. Sci.* **86**, 200

[34]. K. H. Michel and B. Verberck 2008 *physica status solidi (b)* **245**, 2177

[35]. K. Gourriet, P. Carrez, P. Cordier, A. Guitton, A. Joulain, L. Thilly, and C. Tromas 2015 *Philos. Mag.* **95**, 2539

[36]. A. Guitton, S. V. Petegem, C. Tromas, A. Joulain, H. V. Swygenhoven, and L. Thillys 2014 *Appl. Phys. Lett.* **104**, 241910

[37]. A. Guitton, A. Joulain, L. Thilly, and C. Tromas 2012 *Philos. Mag.* **92**, 4536

[38]. Z. Wang, J. Liu, L. Wang, X. Li, P. Ke, and A. Wang 2017 *Appl. Surf. Sci.* **396**, 1435

[39]. J. Xiao, T. Yang, C. Wang, J. Xue, and Y. Wang 2013 *J. Amer. Ceram. Soc.* **98**, 1323

[40]. A. Evans, J. Hutchinson, and Y. Wei 1999 *Acta Mater.* **47**, 4093

[41]. L. Jian, T. Hu, H. Yang, D. Zhang, T. Topping, E. J. Lavernia, and J. M. Schoenung 2016 *Nanoscale* **8**, 10541

[42]. J. S. Koehler 1970 *Phys. Rev. B* **2**, 547

[43]. M. D. Uchic 2004 *Science* **305**, 986

[44]. D. Jang and J. R. Greer 2010 *Nat. Mater.* **2**, 2622

[45]. G. Abadias, S. Dub, and R. Shmegera 2006 *Sur. Coat. Tech.* **200**, 6538

[46]. D. Bhattacharyya, N. Mara, P. Dickerson, R. Hoagland, and A. Misra 2011 *Acta Mater.* **59**, 3804

[47]. X. Deng, N. Chawla, K. Chawla, M. Koopman, and J. Chu 2005 *Adv. Eng. Mat.* **7**, 1099

[48]. S. Lloyd, A. Castellero, F. Giuliani, Y. Long, K. McLaughlin, J. Molina-Aldareguia, N. Stelmashenko, L. Vandeperre, and W. Clegg 2005 *Proc. Royal Soc. A: Math., Phys. And Eng. Sci.* **461**, 2521

[49]. D. Bhattacharyya, N. Mara, R. Hoagland, and A. Misra 2008 *Scr. Mater.* **58**, 981

[50]. D. Buord, Y. Liu, J. Wang, H. Wang, and X. Zhang 2014 *Nat. Comm.* **5**, 4864

[51]. I. Salehinia, S. Shao, J. Wang, and H. M. Zbib 2014 *JOM* **66**, 2078

[52]. J. He, W. Li, H. Li, and C. Liu 1998 *Surf. Coat. Tech.* **103-104**, 276

[53]. A. Madan, Y. Wang, S. A. Barnett, C. Engstrom, H. Ljungcrantz, L. Hultman, and M. Grimsditch 1998 *J. Appl. Phys.* **84**, 776

[54]. M. B. Daia, P. Aubert, S. Labdi, C. Sant, F. A. Sadi, P. Houdy, and J. L. Bozet 2000 *J. Appl. Phys.* **87**, 7753

[55]. D. Bhattacharyya, N. Mara, P. Dickerson, R. Hoagland, and A. Misra 2010 *Philos. Mag.* **90**, 1711

[56]. P. Anderson and C. Li 1999 *Nanostr. Mater.* **5**, 349

[57]. P. Anderson, T. Foecke, and P. Hazzledine 1999 *MRS Bull.* **24**, 27

[58]. A. Misra, J. P. Hirth, and H. Kung 2002 *Philos. Mag. A* **82**, 2935

[59]. W. Yang, G. Ayoub, I. Salehinia, B. Mansoor, and H. Zbib 2017 *Acta Mater.* **122**, 99

[60]. J. Wang, C. Zhou, I. J. Beyerlein, and S. Shao 2013 *JOM* **66**, 102

[61]. Z. Wang, M. Saito, S. Tsukimoto, and Y. Ikuhara 2011 *J. Ceram. Soc. Jpn.* **119**, 783

[62]. Z. Lin, X. Peng, T. Fu, Y. Zhao, C. Feng, C. Huang, and Z. Wang 2017 *Physica E* **89**, 15

[63]. S. K. Yadav, S. Shao, J. Wang, and X.-Y. Liu 2015 *Sci. Rep.* **5**, 17380

[64]. S. K. Yadav, R. Ramprasad, J. Wang, A. Misra, and X.-Y. Liu 2014 *Model. Simul. Mat. Sci. Eng.* **22**, 035020

[65]. Y.-M. Kim and B.-J. Lee 2008 *Acta Mater.* **56**, 3481

[66]. H.-K. Kim, W.-S. Jung, and B.-J. Lee 2009 *Acta Mater.* **57**, 3140

[67]. R. Raghavan, J. Wheeler, D. E. de los Ojos, K. Thomas, E. Almandoz. G. Fuentes, and J. Michler 2015 *Mat. Sci. Eng.: A* **620**, 375

[68]. P. C. Yashar and W. D. Sproul 1999 *Vacuum* **55**, 179

[69]. N. Li, H. Wang, A. Misra, and J. Wang 2014 *Sci. Rep.* **4**, 6633

[70]. G. Feldbauer, M. Wolloch, P. O. Bedolla, P. Mohn, J. Redinger, and A. Vernes 2015 *Phys. Rev. B* **91**, 165413

[71]. L. Liu, S. Wang, and H. Ye 2004 *Acta Mater.* **52**, 3681

[72]. J. Wang and A. Misra 2014 *Curr. Opin. Solid State Mater. Sci.* **18**, 19

[73]. R. Zhou, *Molecular Modelling at the Atomic Scale* (CRC Press, Boca Raton, FL, 2014)

[74]. B. J. Alder and T. E. Wainwright 1957 *J. Chem. Phys.* **27**, 1208

[75]. A. Rahman 1964 *Phys. Rev.* **136**, A405

[76]. Y. Xiang (ed.), *Multiscale Modelling and Analysis for Materials Simulation* (World Scientific Publishing Company, Singapore, 2011)

[77]. H. C. Andersen 1980 *J. Chem. Phys.* **72**, 2384

[78]. J. Stadler, R. Mikulla, and H.-R. Trebin 1997 *Int. J. Mod. Phys. C.* **8**, 1131

[79]. S. Plimpton 1996 *J. Comp. Phys.* **117**, 1

[80]. H. Watanabe, M. Suzuki, and N. Ito 2011 *Prog. Theor. Phys.* **126**, 203

[81]. A. I. Duff, M. Finnis, P. Maugis, B. J. Thijsse, and M. H. Sluiter 2015 *Comput. Phys. Commun.* **196**, 439

[82]. http://www.cmsm.iis.u-tokyo.ac.jp/software.html

[83]. J. C. Phillips, R. Braun, W. Wang, J. Gumbart, E. Tajkorshid, E. Villa, C. Chipot, R. D. Skeel, L. Kale, and K. Schulten 2005 *J. Comput. Chem.* **26**, 1781

[84]. B. R. Brooks, C. L. Brooks, A. D. Mackerell, L. Nilsson, R. J. Petrella, B. Roux, Y. Won, G. Archontis, C. Bartels, S. Boresch, A. Caisch, L. Caves, Q. Cui, A. R. Dinner, M. Feig, S. Fischer, J. Gao, M. Hodoscek, W. Im, K. Kuczera, T. Lazaridis, J. Ma, V. Ovchinnikov, E. Paci, R. W. Pastor, B. Post, J. Z. Pu, M. Schaefer, B. Tidor, R. M. Venable, H. L. Woodcock, X. Wu, W. Yang, D. M. York, and M. Karplus 2009 *J. Comput. Chem.* **30**, 1545

[85]. R. Salomon-Ferrer, D. A. Case, and R. C. Walker 2012 *Wiley Interdiscp. Rev.: Comput. Mol. Sci.* **3**, 198.

[86]. J. R. Reimers, *Computational Methods for Large Systems: Electronic Structure Approaches for Biotechnology and Nanotechnology* (John Wiley & Sons Inc., Heidelberg, 2011)

[87]. G. Kresse and J. Furthmueller 1996 *Comput. Mater. Sci.* **6**, 15

[88]. http://gaussian.com/

[89]. http://susi.theochem.tuwien.ac.at/index.html

[90]. http://www.abinit.org

[91]. J. M. Soler, E. Artacho, J. D. Gale, A. Garca, J. Junquera, P. Ordejn, and D. Sanchez-Portal 2002 *J. Phys.: Condens. Matter* **14**, 2745

[92]. P. Gianozzi, S. Baroni, N. Bonini, M. Calandra, R. Car, C. Cavazzoni, D. Cerelosi, G. L. Chiarotti, M. Cococcini, I. Dabo, A. Dal Corso, S. de Gironcoli, S. Fabris, G. Fratesi, R. Gebauer, U. Gerstmann, A. Gougoussis, A. Kokalj, M. Lazzeri, L. Martin-Samos, N. Marzari, F. Mauri, M. Mazzarello, S. Paolini, A. Pasquarello, L. Paulatto, S. Sbraccia, S. Scandolo, G. Sclauezero, A. P. Seitsonen, A. Smogunov, P. Umari, and R. M. Wentzcovitch 2009 *J. Phys.: Condens. Matter* **21**, 395502

[93]. M. Mihalkovic and C. L. Henley 2012 *Phys. Rev. B* **85**, 092102

[94]. M. S. Daw, S. M. Foiles, and M. I. Baskes 1993 *Mater. Sci. Rep.* **9**, 251

[95]. Y. Mishin, M. Mehl, and D. Papaconstantopoulos 2005 *Acta Mater.* **53**, 4029

[96]. J. Tersoff 1988 *Phys. Rev. B* **37**, 6991

[97]. M. Mueller, P. erhart, and K. Albe 2007 *J. Phys.: Condens. Matter* **19**, 326220

[98]. M. I. Baskes and C. F. Melius 1979 *Phys. Rev. B* **20**, 3197

[99]. J. H. Westbrook and R. L. Fleischer (eds.), *Intermetallic Compounds, Principles and Practice, Vol. 1, Principles* (Wiley, Chicester, 1995)

[100]. M. S. Daw and M. I. Baskes 1984 *Phys. Rev. B* **25**, 6443

[101]. M. W. Finnis and J. E. Sinclair 1984 *Philos. Mag. A* **50**, 45

[102]. M. I. Baskes 1987 *Phys. Rev. Lett.* **59**, 2666

[103]. M. Pascuet and J. Fernandez 2015 *J. Nucl. Mater.* **467**, 229

[104]. M. S. Daw and M. I. Baskes 1983 *Phys. Rev. Lett.* **50**, 1285

[105]. P. Brommer, A. Kiselev, D. Schopf, P. Beck, J. Roth, and H.-R Trebin 2015 *Modell. Simul. Mater. Sci. Eng.* **23**, 074002

[106]. R. A. Johnson and D. J. Oh 1989 *J. Mater. Res.* **4**, 1195

[107]. R. R. Zope and Y. Mishin 2003 *Phys. Rev. B* **68**, 024102

[108]. http://crystallography.net/cod/

[109]. D. Schopf, P. Brommer, B. Frigan, and H. -R. Trebin 2012 *Phys. Rev. B* **85**, 054201

[110]. A. I. Duff, T. Davey, D. Korbmacher, A. Glensk, B. Grabowski, J. Neugebauer, and M. W. Finnis 2015 *Phys. Rev. B* **91**, 214311

[111]. W. Humphrey, A. Dalke, and K. Schulten 1996 J. Mol. Graphics **14**, 33

[112]. R. Storn and K. Price 1997 *J. Global Optim.* **11**, 341

[113]. S. Hocker, P. Beck, S. Schmauder, J. Roth, and H. -R. Trebin 2012 *J. Chem. Phys.* **136**, 084707

[114]. J. E. Angelo, N. R. Moody, and M. I. Baskes 1995 *Modell. Simul. Mater. Sci. Eng.* **3**, 289

[115]. S. Chantasiriwan and F. Milstein 1996 *Phys. Rev. B* **53**, 14080

[116]. J. Mei, J. W. Davenport, and G. W. Fernando 1991 *Phys. Rev. B* **43**, 4653

[117]. S. M. Foiles, M. I. Baskes, and M. S. Daw 1986 *Phys. Rev. B* **33**, 7983

[118]. G. Bonny, D. Terentyev, R. C. Pasianot, S. Ponce, and A. Bakaev 2011 *Modell. Simul. Mater. Sci. Eng.* **19**, 085008

[119]. N. Li, S. K. Yadav, J. Wang, X. -Y. Liu, and A. Misra 2015 *Sci. Rep.* **5**, 18554

[120]. K. Mommma and F. Izumi 2011 *J. Appl. Crystallog.* **44**, 1272

[121]. A. Stukowski 2009 *Modell. Simul. Mater. Sci. Eng.* **18**, 015012

[122]. J. Li 2003 *Modell. Simul. Mater. Sci. Eng.* **11**, 173

[123]. A. Kuksin, S. Starikov, D. Smirnova, and V. Tseplyaev 2016 *J. Alloys Compd.* **658**, 385

[124]. D. Schopf, H. Euchner, and H. -R. Trebin 2014 *Phys. Rev. B* **89**, 214306

[125]. M. Mendeley, M. Kramer, C. Becker, and M. Asta 2008 *Philos. Mag.* **88**, 1723

[126]. H. Yu and F. Sun 2009 *Physica B* **404**, 1692

[127]. S. K. Yadav, R. Ramprasad, A. Misra, and X. -Y. Liu 2012 *J. Appl. Phys.* **111**, 083505

[128]. R. Ahuja, O. Eriksson, J. M. Wills, and B. Johansson 1996 *Phys. Rev. B* **53**, 3072

[129]. T. Lee, K. Ohmori, C. -S. Shin, D. G. Cahill, I. Petrov, and J. E. Greene 2005 *Phys. Rev. B* **71**, 144106

[130]. W. M. Haynes (ed.), *CRC Handbook of Chemistry and Physics, 97th ed.* (CRC Press/Taylor & Francis, Boca Raton, FL, 2017)

[131]. D. G. Sangiovanni, D. Edstrom, L. Hultman, V. Chirita, I. Petrov, and J. E. Greene 2012 *Phys. Rev. B* **86**, 155443

[132]. D. G. Sangiovanni, B. Alling, P. Steneteg, L. Hultman, and I. A. Abrikosov 2015 *Phys. Rev. B* **91**, 054301

[133]. R. Gaudoin, W. M. C. Foulkes, and G. Rajagopal 2002 *J. Phys.: Condens. Matter* **14**, 8787

[134]. M. J. Gillan 1989 *J. Phys.: Condens. Matter* **1**, 689

[135]. P. Tzanetakis, J. Hillairet, and G. Revel 1976 *physica status solid (b)* **75**, 433

[136]. S. V. Dudiy and B. I. Lundqvist 2001 *Phys. Rev. B* **64**, 045403

[137]. D. Gall, S. Kodambaka, M. A. Wall, I. Petrov, and J. E. Greene 2003 *J. Appl. Phys.* **93**, 9086

[138]. L. Tseteseris, N. Kalfagiannis, S. Logothetidis, and S. T. Pantelides 2007 *Phys. Rev. B* **76**, 224107

[139]. G. -D. Zhan, M. Mitomo, T. Nishimura, R. -J. Xie, T. Sakuma, and Y. Ikuhara 2004 *J. Amer. Ceram. Soc.* **83**, 841

[140]. R. Schwaiger, B. Moser, M. Dao, N. Chollacoop, and S. Suresh 2003 *Acta Mater.* **51**, 5159

[141]. K. Mandel, M. Radajewski and L. Krger 2014 *Mater. Sci. Eng.: A* **612**, 115

[142]. S. Ishihara, K. Akashiro, T. Tanizawa, N. Furushiro, Y. Umakoshi and S. Hori 2000 *Mater. Trans. JIM* **41**, 376

[143]. J. S. Carpenter, A. Misra, M. D. Uchic, and P.M. Anderson 2012 *Appl. Phys. Lett.* 101, 051901.

[144]. R. Hoagland, R. Kurtz, and C. Henager 2004 *Scr. Mater.* **50**, 775.

[145]. J. Wang, R. Hoagland, J. Hirth, and A. Misra 2008 *Acta Mater.* **56**, 3109

[146]. H.M. Zbib, C.T. Overman, F. Akasheh, and D. Bahr 2011 *Int. J. Plast.* 27, 1618

[147]. R. Zhang, J. Wang, I. Beyerlein, A. Misra, and T. Germann 2012 *Acta Mater.* **60**, 2855

APPENDICES

Appendix A: Fitted Parameters of Potential Function

The followings are the fitted function parameters of the fitted potential. Please refer to Chapter 2 for details on variables.

Table A.1: Function parameters for pair interaction.

	Ti-Ti	Ti-Al	Ti-N	Al-Al	Al-N	N-N
C_1	192.7906	185.2365	4.0608	391.2714	43.4544	33.8845
η_1	91.1618	5.5976	2.0893	8.6322	6.7328	19.6944
C_2	300.0014	44.8351	9.6273	110.3441	0.7986	-71.6605
η_2	6.9271	4.3704	4.0929	6.6527	1.6491	6.2671
k	2.4514	1.2658	3.9075	2.9299	3.3483	3.3490
ϕ	1.6139	0.0008	1.4290	0.4705	4.2006	2.4693
h	0.5804	1.4654	1.4324	1.8537	1.0511	0.9215

Table A.2: Function parameters for embedding energy.

	Ti	Al	N
F_0	-1.32691	-3.57893	-19.99992
γ	0.10001	0.61265	0.89425
F_1	0.00033	-0.00036	0.00009

Table A.3: Function parameters of electron density

	Ti	Al	N
a_1	0.22126	0.04661	-0.80873
a_2	-0.12162	-0.86839	0.19535
α	5.01398	1.29356	2.86758
β	1.97999	2.04348	2.56376
h	2.96589	2.26672	2.71954

APPENDIX B: Deformation Analysis in Ovito and AtomEye

I used two different atomic properties calculation scheme to analyse the compression results in Chapter 3. They will be explained here in a little more detail.

1. **Displacement Vector**

   In this mode, I have to first choose the reference configuration. In most cases, it is specified as the initial position after equilibration. The displacement vector is then calculated by subtracting the initial position of each atom with its current position. To look only at local displacement, instead of whole cell movement such as in compression, the atoms' initial positions are resized proportionally to the current box size, from which instead then the displacement vector is calculated. The vector is displayed as centred on the atom. Displacement magnitude is simply the Cartesian size of this vector.

2. **Von Mises Local Shear Strain**

   This powerful method is somewhat complicated to explain. Consider atom i and initial nearest neighbour j, which undergoes deformation from initial position $\mathbf{d}_{ji}^{0}$ to

current position $\mathbf{d}_{ji}$. Then, the deformation matrix $\mathbf{J}_i$ can be calculated by minimizing

$$\sum_j |\mathbf{d}_{ji}^0 - \mathbf{d}_{ji}|^2 \quad \rightarrow \quad \left(\sum_j \mathbf{d}_{ji}^{0T}\mathbf{d}_{ji}^0\right)^{-1}\left(\sum_j \mathbf{d}_{ji}^{0T}\mathbf{d}_{ji}\right) \tag{B.1}$$

After obtaining deformation matrix, the local Lagrangian matrix can be determined.

$$\boldsymbol{\eta}_i = \frac{1}{2}(\mathbf{J}_i\mathbf{J}_i^T - \mathbf{I}) \tag{B.2}$$

The local shear strain of atom i is then computed using matrix's component:

$$\eta_i^{Mises} = \sqrt{\eta_{yz}^2 + \eta_{xz}^2 + \eta_{xy}^2 + \frac{(\eta_{yy}-\eta_{zz})^2 + (\eta_{xx}-\eta_{zz})^2 + (\eta_{xx}-\eta_{yy})^2}{6}} \tag{B.3}$$

The parameters then take non-negative values. Using this measure, one can quantify the degree of plasticity. In most cases, atoms are coloured using rainbow scale: from blue being the lowest to red signifying highest strain in the scale.

Appendix C: Input Scripts

I use the following scripts:

VASP AIMD Script

```
SYSTEM = Samples MD
PREC = Med
EDIFF= 1E-2
ENCUT = 700 # ENMAX in POTCAR
NELM = 20 # max number of selfconsistance steps, 40 normally
NELMIN = 4 # min number of SC steps
NSW = 1000 # max number of steps for IOM, # of MD steps
NBLOCK = 1 ; KBLOCK = 1000 # default =1
IBRION = 0 # -1 if NSW=1,0 ,0 for MD, 1 for newton, 2 for conj-grad
POTIM = 1.00 #
ISIF = 2 # 3=full vol relax, 2=no vol or shape change
ISMEAR = 0 # default
SIGMA = 0.2 # default Check this one!
LPLANE = .TRUE. # good for large cells
NSIM = 1
```

LREAL = Auto # projection in reciprocal space, good for large cells
NPAR = 8 #
RWIGS = 1 1 1 1 # wigner seitz radius (need a number for each atom type)
VOSKOWN = 0 # default=0, 1 different interpolation formula
ALGO = VeryFast #
MAXMIX = 30 #something to do with dielectric function, also for MD
ISYM = 0 #switch of symmetry, for MD
SMASS = 0 #
TEBEG = 3000 #temperature for MD
TEEND = 3000
LSCALAPACK = .TRUE.
IALGO=48
AMIN = 0.01
LWAVE = .FALSE. # determines if WAVECAR is written

Potfit Control Script
ntypes 3
config fitdat
startpot bilayer.pot
endpot bilayer.eam
tempfile bilayer.tmp
imdpot dummy.imd
plotfile bilayer.plot
write-pair 1
write-lammps 1
imdpotsteps 5000
output-prefix bilayer
opt 1
eng-weight 20
anneal-temp 10
evo-threshold 0.8
stress-weight 1
seed 42

LAMMPS NPT Script
units metal
boundary p p p
atom-style atomic
atom-modify map array
variable latparam equal 4.225
——— Create Atoms ———————
read-data aot-thick1-nm-40401
mass 1 47.867
mass 3 26.9815
mass 2 14.0067
———- Calling the potential file———————

```
pair-style eam/alloy
pair-coeff * * bilayer.lammps.eam Ti N Al
———— Running NPT simulation———————-
timestep 0.001
velocity all create 300 4928459 dist gaussian
dump melt all atom 5000 dump.dat
restart 100000 restart.*
thermo 500
thermo-style custom step temp etotal pe enthalpy press vol lx ly lz pxx pyy pzz pyz pxz
pxy
fix 1 all npt temp 300 300 0.1 aniso 0 0 0.1
run 250000
unfix 1
```

LAMMPS Compression Script

```
# Input file for uniaxial compressive loading of single crystal aluminum # Mark Tschopp,
November 2010
# ——————————— INITIALIZATION ——————————————-
units metal
dimension 3
boundary p p p
atom-style atomic
# variable latparam equal 4.05
# ——————————— ATOM DEFINITION ——————————————-
read-data aot-thick1-45451
mass 1 47.867
mass 3 26.9815
mass 2 14.0067
# ——————————— FORCE FIELDS ———————————————
pair-style eam/alloy
pair-coeff * * bilayer.lammps.eam Ti N Al
# ———————————- SETTINGS ———————————————
compute csym all centro/atom fcc
compute peratom all pe/atom
########################################
# EQUILIBRATION
reset-timestep 0
timestep 0.001
velocity all create 300 12345 mom yes rot no
fix 1 all npt temp 300 300 1 aniso 0 0 1 drag 1
# Set thermo output
thermo 500
thermo-style custom step lx ly lz press pxx pyy pzz pe temp
# Run for at least 10 picosecond (assuming 1 fs timestep)
run 40000
```

```
unfix 1
# Store final cell length for strain calculations
variable tmp equal “lz”
variable L0 equal $tmp
print “Initial Length, L0: $L0”
##############################:q#########
# DEFORMATION
reset-timestep 0
fix 1 all npt temp 300 300 1 x 0 0 1 y 0 0 1 drag 1
variable srate equal 5.0e9
variable srate1 equal “-v-srate / 1.0e12”
fix 2 all deform 1 z erate $srate1 units box remap x
# Output strain and stress info to file
# for units metal, pressure is in [bars] = 100 [kPa] = 1/10000 [GPa]
# p2, p3, p4 are in GPa
# Strain in percent
variable strain equal “((lz - v-L0)*100)/v-L0”
variable p1 equal “-v-strain”
variable p2 equal “pxx/10000”
variable p3 equal “pyy/10000”
variable p4 equal “pzz/10000”
fix def1 all print 200 “$p1 $p2 $p3 $p4” file aot1-u-z-rate-2.txt screen no
# Use cfg for AtomEye
dump 4 all cfg 3200 dump-cmp-aot1-u-rate-2.*.cfg mass type xs ys zs id c-csym c-
peratom fx fy fz
dump-modify 4 element Ti N Al
# Ovito dump
dump mydump all atom 800 dump-aot1-u-z-rate-2.atom
# Display thermo
thermo 100
thermo-style custom step v-strain temp v-p2 v-p3 v-p4 ke pe press
thermo-modify lost warn norm yes flush yes
run 160000
#######################################
# SIMULATION DONE
print “All done”
```